Excitons in Quantum Dots and Design of their Environment

Inauguraldissertation

zur
Erlangung der Würde eines Doktors der Philosophie
vorgelegt der
Philosophisch-Naturwissenschaftlichen Fakultät
der Universität Basel

von

Matthias Christian Löbl

aus Deutschland

Basel, 2020

The original document is saved on the university of Basel document server
http://edoc.unibas.ch

This work is licensed under a Creative Commons
Attribution-NonCommercial-NoDerivatives 4.0 International License.
The complete text may be reviewed here:
http://creativecommons.org/licenses/by-nc-nd/4.0/

Genehmigt von der Philosophisch-Naturwissenschaftlichen Fakultät auf Antrag von

Prof. Dr. Richard J. Warburton

Prof. Dr. Jonathan J. Finley

Prof. Dr. Martino Poggio

Basel, den 17. Dezember 2019

Prof. Dr. Martin Spiess
Dekan

Summary

Self-assembled semiconductor quantum dots confine single carriers on the nanometer-scale. For the confined carriers, quantum mechanics only allows states with discrete energies. Due to the Pauli exclusion principle, two carriers of identical spin cannot occupy the same energy level. When the quantum dot hosts more carriers (electrons or electron-holes), they fill the states according to Hund's rules. The recombination of a single exciton (a bound electron-hole pair) confined to the quantum dot gives rise to the emission of a single photon. For these reasons, quantum dots are often regarded as artificial atoms or even two-level systems.

However, the environment of a quantum dot has a strong effect on it. The properties of a quantum dot can significantly deviate from that of an atom when it couples to continuum states in the surrounding semiconductor material; charge noise can strongly broaden the absorption of the quantum dot beyond its natural linewidth. On the other hand, designing the environment of a quantum dot enables to control its properties. Tunnel-coupling the quantum dot to a Fermi-reservoir or integrating it into cavities and waveguides are important examples.

The first part of this thesis investigates a situation in which the environment of the quantum dot is especially problematic: when the quantum dot is integrated into a nanostructured device, close-by surfaces cause significant charge noise. To reduce the charge noise, a new type of ultra-thin diode structure is developed as a host for the quantum dots. The design of the diode is challenging as it must fulfill several requirements to enable spin-physics and quantum optics on single quantum dots in nanostructures. For quantum dots embedded in the final diode structure, we simultaneously achieve full electrical control of their charge state, ultra-low charge noise, and excellent spin properties.

Even when the quantum dots have a large distance to surfaces, coupling to interfaces within the semiconductor heterostructure can be a problematic source of noise and decoherence. For InGaAs quantum dots, the so-called wetting layer is an interface that forms during the growth of the quantum dots and is located in their direct spatial proximity. The continuum states of the two-dimensional wetting layer are energetically close to the p- and d-shells of the quantum dots. Problematic coupling between quantum dot

and wetting layer states takes place for charged excitons. The second part of this work shows that a slight modification to the growth process of the quantum dots removes wetting layer states for electrons. The wetting-layer free quantum dots can contain more electrons than conventional InGaAs quantum dots and the linewidths of highly charged excitons significantly improve. Importantly, these quantum dots retain other excellent properties of conventional InGaAs quantum dots: control of charge and spin state, and narrow linewidths in resonance fluorescence.

Also for different types of self-assembled semiconductor quantum dots, the growth has a significant influence on the optical properties of confined excitons. In the third part of this thesis, it is investigated how nucleation processes during the growth are connected to the optical properties of GaAs quantum dots in AlGaAs. Remarkably, this connection can be studied post-growth by spatially resolved optical spectroscopy. The main experimental observation is the presence of strong correlations between the optical properties of a quantum dot and its proximity to neighboring quantum dots. In particular, the emission energy and the diamagnetic shift of the quantum dot emission are strongly correlated with the area of the so-called Voronoi cell surrounding the quantum dot. The observations can be explained with the capture zone model from nucleation theory, which shows that the optical quantum dot properties reveal information about the material diffusion during the semiconductor growth.

As explained before, the surrounding semiconductor environment can have a strong effect on the properties of quantum dots. However, even for a well-isolated quantum dot, there are higher shells of the quantum dot itself which can lead to effects beyond a two-level system. In the final part of this thesis, a radiative Auger process is investigated. The radiative Auger effect is directly connected to higher shells of the quantum dot and appears in its emission spectrum. It arises when resonantly exciting the singly charged exciton (trion). When one electron recombines radiatively with the hole, the other one can be promoted into a higher shell. The radiative Auger emission is red-shifted by the energy that is transferred to the second electron. The corresponding emission lines show a strong magnetic field dispersion which is characteristic for higher shells. The radiative Auger effect is observed on both types of quantum dots investigated before. Radiative Auger offers powerful applications: the single-particle spectrum of the quantum dot can be easily deduced from the corresponding emission energies; carrier dynamics inside the quantum dot can be studied with a high temporal resolution by performing quantum optics measurements on the radiative Auger photons.

Contents

1 Introduction 7

1.1 Self-Assembled Quantum Dots . . . 9

2 Charge Tunable Quantum Dots in Membrane Structures 15

2.1 Design and Characterization of an Ultra-Thin *p*-*i*-*n*-*i*-*n*-Diode Structure Hosting Quantum Dots . . . 16

  2.1.1 Introduction . . . 16

  2.1.2 The *p*-*i*-*n*-*i*-*n* Quantum Dot Heterostructure . . . 18

  2.1.3 Design of the Diode Structure . . . 20

  2.1.4 Photoluminescence and Resonance Fluorescence . . . 21

  2.1.5 Electron Spin Pumping . . . 24

  2.1.6 Conclusions . . . 27

  2.1.7 Application of the *p*-*i*-*n*-*i*-*n*-Diode in Nanostructured Devices . . . 35

2.2 Issues and Possible Improvements . . . 36

3 Excitons in Quantum Dots without Electron Wetting Layer States 37

3.1 Introduction . . . 37

3.2 Sample Growth and Ensemble Measurements . . . 39

3.3 Photoluminescence as a Function of Gate Voltage . . . 41

3.4 Triply-Charged Excitons . . . 42

3.5 Temperature Dependence . . . 47

  3.5.1 The X^{3-} Final States . . . 53

  3.5.2 The X^{3-} Initial States . . . 58

  3.5.3 Parameters . . . 60

  3.5.4 Coulomb Matrix Elements for Two-Dimensional Harmonic Oscillator Wavefunctions . . . 61

4 Correlations between Optical Properties and Voronoi-Cell Area 65

4.1 Introduction . . . 65

4.2 Sample Growth . . . 67

4.3 Optical Measurements 67
4.4 Conclusions 72
4.5 Frequency Distribution of the Voronoi-Cell Areas 73
4.6 Correction of the Non-Linearity of the Piezo-Scanners 74
4.7 AFM-Measurement 75
4.8 Emission Energy and Voronoi-Cell Area 75

5 Radiative Auger Process in the Single-Photon Limit 79
5.1 Introduction 79
5.2 Experimental Results 81
5.3 Experimental Methods 87
5.4 Modeling the Magnetic Field Dispersion 88
5.5 Radiative Auger Process: Theory 91
5.6 Cross-Correlation: Theory 94
5.7 Evaluation of Correlation Measurements 97
5.8 Power Dependent Excitation 97
5.9 Spin Pumping and Rabi Oscillations 99

6 Conclusions and Outlook 101

7 Acknowledgment 104

8 Appendix 105
8.1 Solving the Schrödinger Equation Numerically 105
  8.1.1 Method 1: Transferring the Differential Equation into an Eigenvector Problem 106
  8.1.2 Method 2: Step from (Ψ_i, Ψ_{i+1}) to Ψ_{i+2} 106
8.2 Time-Resolved Measurements 108
  8.2.1 Superconducting Single-Photon Detectors 108

Chapter 1

Introduction

Towards the end of the 19th century, some scientists already claimed that physics is completely understood. A few years later, quantum mechanics drastically changed our view on nature. There are probably two reasons why it took so long to come up with quantum mechanics. The first one is that, as its name suggests, it comes into play when dealing with extremely small objects, such as single atoms or molecules. In the early days of quantum mechanics, nobody had ever observed such structures as directly as it is possible today by using scanning probe microscopy [1, 2]. The second reason might be that some conclusions of quantum mechanics are counter-intuitive from a classical perspective [3, 4].

Today, quantum mechanics is an accepted theory, and one has started to make use of it. Developing devices such as lasers or miniaturized transistors requires an understanding of quantum theory. A more recent application idea is using quantum objects as such, as a unit of information in a quantum computer [5, 6, 7], a qubit, or for long-distance quantum key distribution [8].

For such applications, there are many different approaches that range from single trapped ions [5] or color centers in the solid-state [9] to much larger objects such as superconducting circuits [7]. A semiconductor quantum dot (QD) can also be used for some of these applications [6, 10, 11].

In this thesis, all experiments are performed with self-assembled QDs in III-V semiconductors [12]. These QDs are small enough to show many quantum mechanical effects. They can confine single carriers on the nanometer-scale [12]. The strong confinement gives rise to discrete energy levels that can be sequentially filled according to Hund's rules. The decay of an exciton confined to the QD leads to the emission of a single photon – a non-classical state of light [13, 14]. The QD can also host a single spin [15, 16, 17]. For these reasons, a QD is often called an artificial atom. For applications in quantum information, a QD has several strengths and weaknesses that are briefly discussed in the following.

A QD is an excellent source of single photons: the combination of high emission rate (∼GHz), high single-photon purity, and photon indistinguishability [13, 14, 18, 19, 20, 21, 22] is shared with almost no other emitter. These properties make QDs particularly interesting for applications in quantum communication as photons can be transmitted over long distances via optical fibers. Furthermore, the spin of an electron or an electron-hole confined to the QD can be used as a qubit [6]. Spin initialization by optical pumping [15, 16, 23], ultrafast spin manipulation by picosecond-laser pulses [24, 25], and spin-readout [26] by all-optical means have been demonstrated. Spins in different QDs can be entangled by remotely interfering photons emitted from the two QDs [27, 28]. The criteria for quantum information processing are, to a certain extent, fulfilled [29].

However, there are two main challenges: the first one is the noisy solid-state environment of the QD. Noise from nearby charge traps can significantly broaden the QD linewidth beyond the radiative lifetime limit [30]; noise from nuclear spins limits the inhomogeneous dephasing time (T_2^*) of an electron spin in the QD to a few ns [31, 32, 33, 34]; lattice vibrations (phonons) or coupling to continuum states [35, 36] can lead to rapid dephasing and affect both the spin properties and the linewidth of the QD. The second challenge is the self-assembled nature of the QDs. They grow at random locations on the sample. For experiments with a few QDs, it is sufficient to determine their position post-growth [37]. For scalable applications, this method is highly disadvantageous, and an array of well ordered QDs with close-to identical properties would be highly desirable.

Some of the described problems have been solved within the last years: charge noise is strongly reduced when using ultra-clean material [14, 38, 39, 40]. Active or passive feedback on the QD-emission can further mitigate the noise [41, 42]. Phonon-related effects can be strongly reduced by operating at low temperatures where the emission of QDs is, in contrast to many other emitters [43], dominated by the zero-phonon line [44]. The interaction with continuum states such as the wetting layer can be reduced by modifications to the QD-growth [45]. Spin dephasing times are strongly enhanced for the spin of a hole (an electron vacancy) compared to an electron spin because the hole has a *p*-type atomic wavefunction. Therefore, its interaction with the nuclei is reduced [17, 46]. Novel ideas for site-control of otherwise self-assembled QDs might mitigate the scalability issue [47].

Two things should be said: first, solving one of these problems often comes along with making another one worse, and there are different types of QDs with different strengths and weaknesses. Site-control, for instance, can be easily achieved by etching an array of nucleation sites into a substrate [48]. Such a process usually leads to defects created during the etching step, which, in turn, can cause significant additional charge noise

[49, 50].

Second, some issues turned out to be easier to solve or less fundamental than others. Whereas charge noise is more a question of material quality, nuclear spins remain a problem and are inherent to the used atomic species. Even for a hole-spin with strongly reduced nuclear spin-interaction, dephasing times have so far been limited to $T_2^* \sim 10^2$ ns in the best case [17, 46]. Sophisticated techniques such as nuclear spin narrowing [51] or real-time Hamiltonian estimation [52] are needed to prolong the dephasing time further. On the other hand, the spin dephasing time is relatively long in comparison to the time needed for optical spin-manipulation [24], which enables some quantum applications [53].

Very promising applications of QDs are hybrid-systems. The QD is a bright single-photon emitter [13, 14, 20]. It can be used as an optical interface for other systems which itself do not couple well to light. Recent ideas involve interfacing a gate-defined spin qubit [54, 55] or a superconducting circuit [56]. The QD is also a very sensitive charge sensor [57], enabling an optical readout of the charge state of other qubits [58]. Furthermore, the QD can interface an ultra-cold atom memory based on rubidium or cesium – a promising architecture for quantum repeater applications [59]. Finally, the QD can be embedded in optical or mechanical cavities or in waveguide architectures [10] – approaches which enable quantum optics experiments in the solid-state [60, 61].

1.1 Self-Assembled Quantum Dots

A particle confined to a finite volume can only take discrete values of energy, E. This energy quantization is a result of quantum mechanics. The so-called eigenenergies can be calculated by solving the time-independent Schrödinger equation

$$\left(-\frac{\hbar^2}{2m^*}\Delta + V(\vec{x})\right)|\Psi(\vec{x})\rangle = E\,|\Psi(\vec{x})\rangle\,, \tag{1.1}$$

where $|\Psi(\vec{x})\rangle$ is the wavefunction of a particle with an effective mass m^* inside a potential $V(\vec{x})$.

However, the quantization is irrelevant for many macroscopic objects because the energy spacing between these discrete levels is so small that it easily can be bridged by thermal excitation. The question when quantum effects become significant depends on the temperature and the size of the object. A simple criterion is given by the thermal wavelength

$$\lambda = \frac{h}{\sqrt{2\pi m^* k_\mathrm{B} T}}. \tag{1.2}$$

When the size of an object is smaller than this length scale, quantum effects become observable since the thermal energy is smaller than the quantization energies – the object can be considered as zero-dimensional. Constraints for quantum applications are typically much stricter than this criterion, i.e. require even lower temperatures.

Semiconductor QDs are small enough such that Eq. 1.2 is fulfilled at cryogenic temperatures. There are different kinds of QDs with different sizes. Some nanocrystals have sizes down to a few nanometers [62]; gate defined QDs can have sizes up to several hundred nanometers [63]. The QDs investigated in this thesis, self-assembled semiconductor QDs, have typical lateral sizes in the range $\sim 20 - 40$ nm [64].

Usually, self-assembled semiconductor QDs are grown by molecular beam epitaxy. There are several methods that lead to self-assembly of nanostructures and eventually can be used to grow these QDs. In this work, two different types of QDs are used: self-assembled InGaAs QDs that are grown in the so-called Stranski-Krastanov mode [65] and GaAs QDs in AlGaAs which are grown via local droplet-etching [66]. The growth of InGaAs QDs is based on using lattice-mismatched semiconductors. When InAs is grown on top of GaAs, only about 1.5 monolayers of InAs adopt the lattice-constant of the GaAs-substrate and form the so-called wetting layer. When more InAs is deposited, the lattice-mismatch of both materials leads to the formation of InAs-islands [67]. When these islands are covered with GaAs, they become optically active QDs. They form a potential minimum for carriers because the semiconductor bandgap of InGaAs is smaller than that of GaAs. Local droplet-etching is a different method that enables the growth of self-assembled QDs without using lattice-mismatched semiconductors – in our case, GaAs QDs embedded in AlGaAs. This method uses the fact that metals such as aluminum or gallium nucleate in the form of small droplets when they are deposited on AlGaAs. These metal-droplets etch into the substrate material, which leads to the formation of nano-holes [66]. The nano-holes are filled up with GaAs, forming a QD inside the surrounding AlGaAs. A more detailed explanation of both growth methods can be found in Chapters 3, 4 and in Refs. [40, 66, 68].

Fig. 1.1(a) shows a scanning electron microscope image of a self-assembled InGaAs in GaAs. The QD appears bright in this image since the contained indium has a higher atomic number than the surrounding material. The QD has a height of ~ 3 nm and a lateral dimension of ~ 30 nm. The indium-concentration is higher in the center of the QD, and the confinement potential is deeper in this region. Therefore, the effective lateral size of the wavefunction in a QD is typically below 10 nm [71, 72].

Since the lateral dimension of the QD is much larger than its extent in the z-direction, the QD can often be modeled as a two-dimensional Harmonic oscillator [63, 73]. The

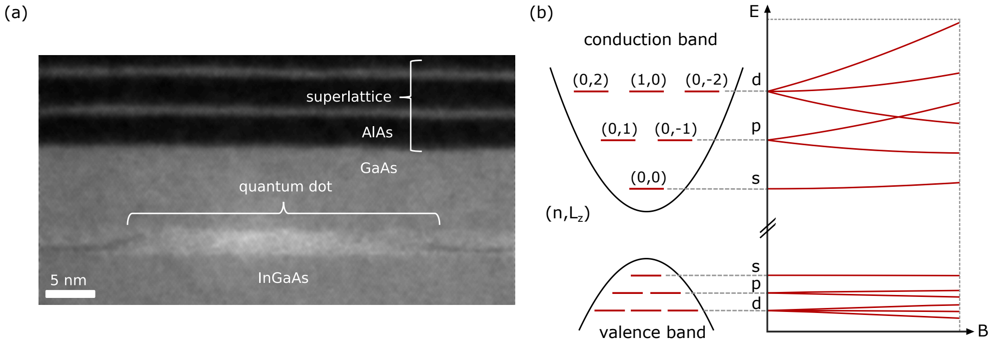

Fig. 1.1: (a) Transmission electron microscopy image of a self-assembled InGaAs QD in GaAs (taken from Ref. [45]). Above the quantum dot, alternating layers of AlAs and GaAs are grown. (b) Energy levels (shells/orbitals) of the quantum dot modeled by a symmetric harmonic confinement potential. With an increasing magnetic field, the degeneracy of the shells is lifted. For the conduction band, the effect of the magnetic field is more pronounced since the electron effective mass is significantly smaller than the hole effective mass. The energy spectrum of the different states forms the Fock-Darwin spectrum [69, 70]. The quantum numbers of the corresponding shells are labeled as n (radial quantum number) and L_z (angular momentum quantum number).

two-dimensional confinement potential has the following form: $V(r) = \frac{1}{2}m_e^*\omega_0^2 r^2$, where m_e^* is the electron effective mass and ω_0 specifies the strength of the confinement. This harmonic confinement is convenient as the Schrödinger equation (Eq.1.1) can be solved analytically. The eigenenergies are multiples of $\hbar\omega_0$, an analytical formula for the wavefunctions is given in Chapter 3. A schematic of the first states (shells) of a QD is shown in Fig. 1.1(b).

The eigenenergies and wavefunctions of a QD change when an external electric or magnetic field is applied. An external electric field adds a linear correction term to the confinement potential, giving rise to the quantum-confined Stark effect. A magnetic field (here in the z-direction) adds a vector potential term to the Schrödinger equation [74]:

$$\left(\frac{1}{2m^*}\mathbf{p}^2 + V(\vec{x})\right)|\Psi(\vec{x})\rangle = E\,|\Psi(\vec{x})\rangle\,, \tag{1.3}$$

where $\mathbf{p} = (-i\hbar\nabla - e\mathbf{A})$ is the momentum operator with $\mathbf{A} = \frac{1}{2}B_z x\mathbf{e}_y - \frac{1}{2}B_z y\mathbf{e}_x$. The corresponding eigenenergies,

$$E_{n,L} = (2n + |L_z| + 1)\,\hbar\omega_1 - \frac{1}{2}L_z\hbar\omega_c, \tag{1.4}$$

are often referred to as the Fock-Darwin spectrum [69, 70], where n and L_z are the radial and the angular momentum quantum numbers. In this expression, $\hbar\omega_c = \hbar eB/m_e^*$ is the electron cyclotron energy and the term ω_1 is given by $\omega_1 = \sqrt{\omega_0^2 + \left(\frac{\omega_c}{2}\right)^2}$. The Fock-Darwin spectrum for a QD with $\hbar\omega_0 = 24$ meV is shown in Fig. 1.1(b). The Fock-Darwin spectrum describes the magnetic field dependence (diamagnetic shift) for many different types of QDs [63, 73, 75]. For very strong magnetic fields, where the magnetic field term dominates over the confinement, the Fock-Darwin spectrum forms a Landau level fan [74]. For small magnetic fields, the diamagnetic shift is sometimes approximated by a parabolic dependence [76, 77]. The shift is more pronounced when $\hbar\omega_0$ is small since the cyclotron energy becomes comparable to $V(r)$ when increasing the magnetic field. For atoms, where the confinement is significantly stronger, this effect is very small.

In a semiconductor, a bound electron-hole pair (exciton) can be excited optically [78]. An exciton in the QD can be created by exciting the surrounding semiconductor material with a laser [79]. Following the above-band excitation, the created electrons and holes relax to the conduction and valence band minimum by multi-phonon emission. Further relaxation down to the ground state of the QD (s-shell) can take place by processes involving just a few phonons [80]. Optical recombination of an electron in the conduction band s-shell of the QD with a hole in its valence band s-shell can take place (photoluminescence). This transition is dipole allowed due to the p-type atomic wavefunction of the valence band hole. The hole has typically a heavy-hole character since the light hole is at higher energy due to strain and the strong confinement potential of the QD [12]. Photoluminescence is a convenient technique to determine the parameters of a QD. However, the above band illumination leads to photoluminescence not only form the QD but also from the surrounding semiconductor material. For using the QD as an artificial atom in the solid-state, resonant excitation is necessary [81]. The resonant excitation technique enables quantum optics experiments on semiconductor QDs [51, 60, 82]. Experimentally, the resonance fluorescence of the QD can be separated from the reflected laser light by using a cross-polarization technique [83].

A QD can be tunnel-coupled to other systems such as another QD or a Fermi-reservoir. For most measurements presented in this thesis, the QDs are tunnel-coupled to a close-by metallic electron reservoir, which acts as a back gate. The method is schematically illustrated in Fig. 1.2(a). There is also a second gate above the QDs, a top gate. Applying a voltage to this diode structure applies an electric field to the QDs and tunes their energy levels with respect to the Fermi-energy of the back gate. The latter effect enables the charge state of the QD to be set deterministically [79]. Note that the tunnel coupling to the back gate should not be too strong but should be significantly less than the Coulomb

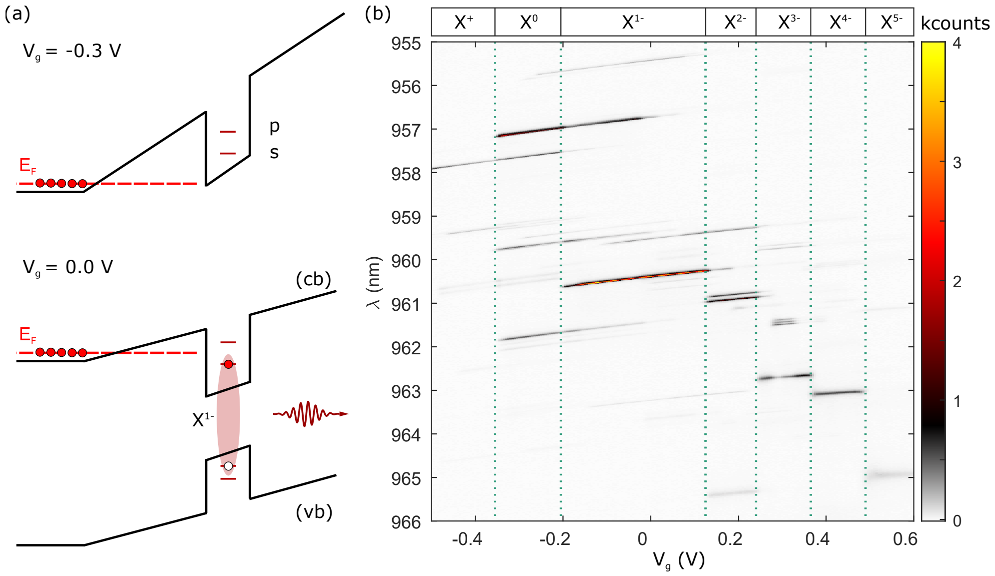

Fig. 1.2: (a) A schematic of a quantum dot (QD) tunnel-coupled to a Fermi-sea with Fermi-energy, E_{F}. At a negative gate voltage, the QD-states are above the Fermi-level. On increasing the voltage, the *s*-shell of the QD becomes lower than the Fermi-level. As a consequence, an electron tunnels from the Fermi-sea into the QD. The on-site Coulomb repulsion within the QD prevents a further electron with the opposite spin from tunneling into the *s*-shell (Coulomb blockade). (b) Photoluminescence of a QD as a function of the gate voltage. With increasing voltage, the QD-levels are lowered with respect to the Fermi-energy of the Fermi-sea and electrons sequentially fill the QD-shells. When a new electron is added to the QD, its emission energy changes due to the Coulomb interaction between all particles within the QD. This interaction gives rise to a characteristic plateau structure of the emission spectrum as a function of the gate voltage.

and confinement energies of the QD. Otherwise, the QD shells will strongly hybridize with the continuum states of the back gate [84, 85, 86]. Good spin properties for carriers in the QD require even larger tunnel barriers to suppress spin co-tunneling [23]. In the case of InGaAs QDs, tunnel barriers between 20-40 nm are a reasonable choice [23, 79].

Even when the distance between the QDs and the gates is too large for tunnel coupling, the gates can be useful. The emission energy of a QD can be tuned via the d.c. Stark effect when a voltage is applied between the top and the back gate [87]. Besides, the charge state of the QD usually fluctuates randomly if such a diode is not used. As a result, the emission from the QD shows significant telegraph noise (blinking) [88]. Blinking is highly disadvantageous for applications where the QD should provide identical single photons at a constant rate. To improve the optical QD-properties, the concept of gating the surroundings has also been implemented for other emitters, such as vacancy centers [89].

Electrons and holes confined to a QD interact via the Coulomb force. The carrier-carrier interaction terms add to the Schrödinger equation (Eq. 1.1), and single-particle states are no longer accurate when more carriers occupy the same QD. Multi-carrier effects lead to characteristic emission spectra of QDs, where the emission energy abruptly changes whenever a new electron is added to the QD. As a function of the charge of a QD, the photoluminescence shows a series of plateaus [79] (Fig. 1.2(b)). For a low bias voltage, the QD-levels are above the Fermi-level of the back gate, and the QD is empty. An electron-hole pair can be excited optically, and the photoluminescence shows emission from the neutral exciton (X^0). At a gate voltage of $V_g = -0.2$ V, the QD is charged with a single electron from the back gate. The emission is now dominated by the negatively charged trion (X^{1-}), which is red-shifted compared to the neutral exciton. The on-site Coulomb repulsion within the QD prevents a further electron with the opposite spin from tunneling into the QD (Coulomb blockade). At higher gate voltage, even more electrons fill the QD, and emission from highly charged excitons ($X^{2-} - X^{5-}$) is observed. These exciton lines are typically broader than in this measurement due to interaction with the wetting layer [79]. Chapter 3 shows how the electron wetting layer states can be removed. As shown in Fig. 1.2(b), the corresponding QDs have narrow emission lines for highly charged excitons.

When the QD confines several carriers, the strong carrier-carrier interaction withing the QD can lead to rich physics, such as Auger processes, where energy is transferred between the different carriers [35, 90]. In many cases, the origin of an Auger-process is the optical recombination of an electron-hole pair leaving an imbalance between the remaining carriers in the QD. Chapter 3 investigates an Auger process following the optical recombination of the triply charged exciton (X^{3-}). Chapter 5 shows that even for the limit of just three carriers, a similar Auger process can take place. This radiative Auger process is observed on a negative trion.

Chapter 2

Charge Tunable Quantum Dots in Membrane Structures

This section is partly adapted from Ref. [91]: "Narrow optical linewidths and spin pumping on charge-tunable, close-to-surface self-assembled quantum dots in an ultra-thin diode", Matthias C. Löbl, Immo Söllner, Alisa Javadi, Tommaso Pregnolato, Rüdiger Schott, Leonardo Midolo, Andreas V. Kuhlmann, Søren Stobbe, Andreas D. Wieck, Peter Lodahl, Arne Ludwig, Richard J. Warburton, Phys. Rev. B **96**, 165440 (2017).

Deterministically controlling the charge-state of a self-assembled quantum dot by embedding it into a diode has been an important breakthrough [79, 92]. Charge noise is reduced [38] and spin physics has been very successful in such structures [15, 16, 17, 27, 28]. A similar breakthrough has been integrating quantum dots in nanostructures such as waveguides or cavities. In such devices, the interaction of the quantum dot with light is enhanced, and routing of the emitted photons is possible [10, 60, 93].

An issue is that both concepts are incompatible to a certain extent. To control the charge state of a quantum dot and electrically stabilize its environment, it is placed in the intrinsic region of a semiconductor and surrounded by two metallic gates. One gate forms a Fermi-reservoir in tunnel contact with the quantum dot. On the one hand, these gates have to be conducting – the carrier concentration should not be too little. On the other hand, too high carrier densities will affect the optical properties of a waveguide by free carrier absorption and plasmonic effects [94]. An *n*-*i*-Schottky diode with a top gate made out of a typical metal such as gold [38] can be ruled out since the absorption would be too high. A good system in that respect is a *p*-*i*-*n*-diode with epitaxial gates, doped with a carrier concentration of $10^{18} - 10^{19}$ cm^{-3} which provides metallic behaviour of the gates [95] in combination with low absorption at optical frequencies [96]. However, in the case of a nanostructure, there are two remaining issues. The first one is related to the fabrication process that can attack the gates and laterally remove material. A second issue is the built-in field of the p-i-n-diode. The built-in field implies that much forward bias is needed to tune the quantum dot in resonance with the Fermi-reservoir in the back-gate [97]. The high forward bias comes along with high currents [97] through the device and can affect the quantum dot performance [97].

2.1 Design and Characterization of an Ultra-Thin p-i-n-i-n-Diode Structure Hosting Quantum Dots

Abstract: We demonstrate full charge control, narrow optical linewidths, and optical spin pumping on single self-assembled InGaAs quantum dots embedded in a 162.5 nm thin diode structure. The quantum dots are just 88 nm from the top GaAs surface. We design and realize a p-i-n-i-n diode that allows single-electron charging of the quantum dots at close-to-zero applied bias. In operation, the current flow through the device is extremely small resulting in low noise. In resonance fluorescence, we measure optical linewidths below $2\,\mu$eV, just a factor of two above the transform limit. Clear optical spin pumping is observed in a magnetic field of 0.5 T in the Faraday geometry. We present this design as ideal for securing the advantages of self-assembled quantum dots – highly coherent single photon generation, ultra-fast optical spin manipulation – in the thin diodes required in quantum nano-photonics and nano-phononics applications.

2.1.1 Introduction

Single self-assembled quantum dots are a source of high-quality single photons; they are also hosts for single spins [17, 24, 26, 98, 99, 100, 101]. Their large optical dipole moment enables fast initialization, manipulation, and readout of spin states all by optical means [12, 16, 24, 101, 102]. In the best case, transform-limited single-photon emission from single quantum dots has been demonstrated [39]. These properties are extremely sensitive to the quantum dot environment. The electrical environment can be controlled by embedding the quantum dots in diode heterostructures. The diode locks the Fermi energy and provides electrical control of the quantum dot charge state. Some of the best performances have been achieved in heterostructures that are ~ 500 nm thick with the quantum dot positioned ~ 300 nm from the GaAs-air interface [38, 39].

The solid-state character of quantum dots allows their optical [10] and mechanical [103, 104] properties to be engineered by nano-structuring. For instance, embedding emitters in a membrane leads to the suppression of out-of-plane radiation modes through total internal reflection; control of the in-plane modes can be achieved via lateral patterning of the membrane. Cavities and waveguides can be engineered by creating defects in a photonic crystal bandgap structure. Single photons can be routed on-chip, and controlled by single two-level systems [105]. Likewise, engineering the mechanical properties can create phononic structures with the aim of controlling the quantum-dot–phonon interaction [103, 104]. In all these applications, the basic building block is a thin GaAs membrane. It is crucial that the quantum dots in these thin structures exhibit the same excellent properties of quantum dots in bulk-like structures. This has not been achieved so far.

Typical photonic crystal membranes, in the wavelength regime relevant for InGaAs quantum dots, range in total thickness from 120 nm to 200 nm [97, 106]. The first demonstrations of charge control on quantum dots in photonic crystals used thin *p*-*i*-*n* diode structures [97, 107]. However, the large built-in electric field in combination with the small thickness of these devices led to a large potential at the position of the quantum dots shifting the Coulomb plateaus to large forward bias voltages. This resulted in high tunneling currents at the operating bias in *p*-*i*-*n*-membrane devices, a possible explanation for the absence of spin pumping on embedded quantum dots [97]. Besides, the optical linewidths of quantum dots were relatively high in these structures.

In order to avoid the problems associated with high tunneling currents, we present here a quantum dot diode which operates close to zero bias. The main idea is to incorporate an *n*-layer within a *p*-*i*-*n* device, resulting in a *p*-*i*-*n*-*i*-*n* diode. The intermediate *n*-layer is fully ionized. Most of the built-in field between the outer *p*- and *n*- gates drops between the top *p*-gate and the intermediate *n*-layer. The electric field at the location of the quantum dots is therefore much smaller than in a *p*-*i*-*n* diode with equal dimensions. This allows single-electron charging to occur close to zero bias. The *p*-*i*-*n*-*i*-*n* diode is used in silicon transistor technology [108, 109], albeit with lateral rather than vertical control of the doping. It has also been employed in self-assembled quantum dot devices [107, 110], but in these experiments, narrow optical linewidths in combination with good spin properties were not achieved.

We present here a careful design that fulfills a list of criteria. The design rests on a full quantitative analysis of the band bending. It is realized using state-of-the-art GaAs heterostructures [39, 40]. We present resonant laser spectroscopy on single quantum dots in a 162.5 nm thick *p*-*i*-*n*-*i*-*n* diode with a quantum dot to surface distance of just 88 nm. Deterministic charge control at low bias, narrow optical linewidths, as well as optical spin pumping is demonstrated for these close-to-surface quantum dots. The developed heterostructure is ideal for electrical control of quantum dots in nanostructured membranes for photonic and phononic applications.

2.1.2 The p-i-n-i-n Quantum Dot Heterostructure

In the design of this structure, we have to fulfill a number of constraints. First, the quantum dots should operate in the Coulomb blockade regime. This allows individual quantum dots to be loaded deterministically with single electrons. Within a Coulomb blockade plateau, the external bias allows some fine-tuning of the optical transition frequencies via the dc Stark effect. Second, the dc current flowing through the device should be as small as possible to avoid decoherence processes. This can be only guaranteed if the charging voltage is close to zero bias. Third, the optical linewidths on driving the quantum dot resonantly should be small, close to the transform limit. This places stringent conditions on the level of charge noise that can be tolerated. Fourth, the membrane should have as little optical absorption as possible. Fifth, the membrane should be thinner than $\sim 250\,\mathrm{nm}$ to ensure single-mode behavior in waveguide structures. In fact, the fabrication of such nanostructures with a soft-mask technique sets a slightly stronger constraint: 180 nm is the maximum membrane thickness that can be processed with vertical sidewalls [111]. Sixth, the quantum dots must be located close to the center of the diode structure to maximize the coupling to TE-like photonic modes [10]. The combination of the fifth and the sixth constraint means that the distance between quantum dots and the surface cannot be more than 90 nm. Seventh, the spin relaxation time should be large so that the spin can be initialized and manipulated. In a diode device at low temperature, this means that the co-tunneling rate between a quantum dot electron spin and the Fermi sea should be suppressed by using a relatively large tunnel barrier [112]. In such a situation, the spin can be initialized into one of its eigenstates by optical pumping [15, 16, 23, 26].

Fulfilling these constraints is very challenging. It is clearly necessary to work with epitaxial gates, n- and p-type regions in the device, as a metallic Schottky barrier is highly absorbing. In principle, a thin p-i-n diode is a possibility. However, at zero bias, there is a very large built-in electric field (Fig. 2.1(a)). Furthermore, the quantum dots must be positioned at least $30 - 35\,\mathrm{nm}$ away from the n-type back contact to suppress co-tunneling sufficiently. The combination of both constraints means that the quantum dot charges with a single electron only at a large and positive bias, around ~ 1 V. A high current through the device is hard to avoid under these conditions [97, 113]. The quantum dots could be located closer to the back gate while suppressing co-tunneling by using AlGaAs tunneling barriers. Highly opaque AlGaAs tunneling barriers have been successfully used [30, 87, 90]. More transparent AlGaAs tunneling barriers require extremely precise control of thickness and Al-content, hard to achieve in practice.

An alternative to the p-i-n diode is a diode with an additional n-layer in the intrinsic

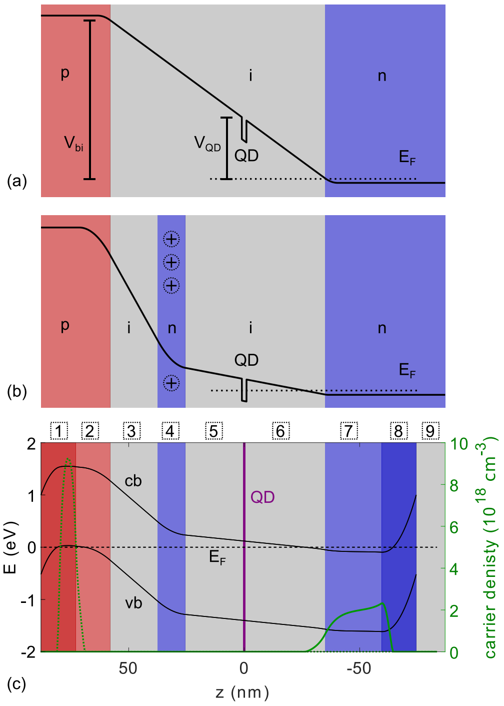

Fig. 2.1: (a,b) Schematic conduction band profile of a *p*-*i*-*n* and *p*-*i*-*n*-*i*-*n* diode at zero bias voltage. In the *p*-*i*-*n*-*i*-*n* structure, an intermediate, fully ionized *n*-type layer causes band bending, reducing the potential difference between quantum dots and back gate. In this way, the quantum dots can be charged at a bias voltage close to zero. In contrast, a large positive voltage must be applied to the *p*-*i*-*n* diode. (c) Heterostructure of the investigated samples. Conduction (cb) and valence (vb) band edges are plotted in black and the density of free carriers is plotted in green (dotted line for holes, solid line for electrons). The dashed black line indicates the Fermi level, E_F. The purple layer indicates the location of the quantum dots at the center of the membrane. The quantum dots are not included in the band-structure simulation. The diode structure is grown on top of a 1371 nm thick $\mathrm{Al_{0.75}Ga_{0.25}As}$ sacrificial layer enabling selective underetching. The quantum dots are a distance of 35 nm away from a back gate consisting of two *n*-type layers (light and dark blue). The top gate consists of two *p*-type layers with different doping concentrations (indicated in red). An additional *n*-type layer is located between quantum dots and top gate. The full heterostructure is constructed as follows: 12.5 nm intrinsic GaAs (layer 9), 15 nm *n*-type GaAs with a doping concentration of $n_{D+} = 8.0 \cdot 10^{18}\,\mathrm{cm}^{-3}$ (layer 8), 24.5 nm *n*-type GaAs with $n_D = 2.0 \cdot 10^{18}\,\mathrm{cm}^{-3}$ (layer 7), 35 nm intrinsic GaAs (layer 6), a layer of InGaAs quantum dots, additional 25.5 nm intrinsic GaAs (layer 5), 12 nm *n*-type GaAs with $n_d = 2.0 \cdot 10^{18}\,\mathrm{cm}^{-3}$ (layer 4), 20.5 nm intrinsic GaAs (layer 3), 15 nm *p*-type GaAs with $n_A = 2.0 \cdot 10^{18}\,\mathrm{cm}^{-3}$ (layer 2), 15 nm *p*-type GaAs with $n_{A+} = 1.0 \cdot 10^{19}\,\mathrm{cm}^{-3}$ (layer 1).

region, a *p-i-n-i-n* device (Fig. 2.1(b)). The additional *n*-layer lies in the depletion region of the surrounding *p-i-n* diode. It is fully depleted such that it becomes positively charged. At zero bias, the total potential drop between the outer *p*- and *n*-layers is the same as in the *p-i-n* diode, but now there is a large drop between the top *p*-contact and the intermediate *n*-layer, followed by a small drop between the intermediate *n*-layer and the back contact. By choosing the location and doping levels of the intermediate *n*-layer, the device can be designed so that the quantum dot charging voltage lies close to zero volts.

The *p-i-n-i-n* design allows in principle all seven criteria to be met. The design is compatible with a 35 nm *i*-GaAs tunneling barrier that is known to result in clear Coulomb blockade yet suppresses co-tunneling sufficiently so that spin initialization can be carried out with high fidelity with optical pumping even in the Faraday geometry [15, 23]. The device can be operated close to zero bias, resulting in very small currents. Absorption is minimized by using epitaxial gates instead of metal Schottky gates. The intermediate *n*-layer is fully ionized and, therefore, should not result in any additional losses. The entire heterostructure (see Fig. 2.1(c)) can be made as thin as 176 nm with the quantum dots located in the center.

The performance of a *p-i-n-i-n* device needs to be tested experimentally. A particular challenge is to achieve narrow optical linewidths for quantum dots just $80 - 90$ nm away from the free surface as it is a known source of charge noise. By using careful design and state-of-the-art material, we report here success in this endeavor.

2.1.3 Design of the Diode Structure

A *p-i-n-i-n* heterostructure is designed to fulfill the seven criteria. Charge carrier densities and electric fields are calculated by solving the Poisson equation, either numerically (nextnano) or analytically within the depletion approximation (see appendix A). In the numerical simulation, the effect of surface depletion due to surface Fermi pinning is taken into account by using a Schottky barrier height of 1 eV at the surface of the structure. The two approaches give results which are in good quantitative agreement. The calculated band bending and exact layer sequence are shown in Fig. 2.1(c).

The sample is grown by molecular beam epitaxy. The diode membrane is grown on top of a 1371 nm thick $\mathrm{Al}_{0.75}\mathrm{Ga}_{0.25}\mathrm{As}$ sacrificial layer which enables fabrication of free standing membranes via selective wet etching [111]. The first part of the membrane is a 12.5 nm thick layer of intrinsic GaAs (no. 9 in Fig. 2.1(c)), followed by a back gate consisting of two layers of *n*-type (silicon-doped) GaAs. The first layer (no. 8) is 15 nm thick and has a high doping concentration n_{D+}; the second layer (no. 7) is 24.4 nm thick with a lower doping concentration n_D (see Fig. 2.1(c) for precise values). A tunnel barrier (no. 6) of 35 nm intrinsic GaAs separates the back gate from a layer of InGaAs quantum dots. Above the quantum dot layer, a 25.5 nm thick capping layer (no. 5) of intrinsic GaAs is grown; subsequently, the intermediate *n*-type layer (no. 4) with a doping density of n_d and a thickness of 12 nm is grown. Finally, there is a 20.5 nm layer (no. 3) of intrinsic GaAs and a top gate consisting of two 15 nm thick *p*-type (carbon-doped) GaAs layers (no. 1, 2). The first *p*-type layer (no. 2) has a lower doping concentration (n_A) than the second one (n_{A+}) (see Fig. 2.1(c) for precise values). The intention of the very highly doped *p*-type layer on top of the device is to prevent surface depletion of the top gate and to allow for fabrication of high-quality ohimc *p*-contacts. Details on the fabrication of electrically gated samples are given in appendix F.

2.1.4 Photoluminescence and Resonance Fluorescence

The samples are measured in a helium bath cryostat at 4.2 K. Optical experiments are performed with a confocal dark-field microscope with a spot size close to the diffraction limit [83]. All measurements are carried out on two samples processed from the same wafer, denoted as samples 1 and 2 in the following. Both samples fulfill all the requirements that we defined at the outset: a diode-like IV-characteristic with low tunneling currents at small bias voltages, exciton charging transitions at small bias voltages, narrow linewidths in resonance fluorescence, and optical spin pumping.

Plotted in Fig. 2.2(a) are the IV-curves of the two samples, both showing diode-like behavior with very low tunneling currents for a large region around 0 V. This excellent electrical behavior is a consequence of both the high material quality of our wafers and the careful contacting of the *p*-gate (see appendix F). First tests of devices with nano-structures do not show an increased leakage current, but further investigations are required to rule out etched sidewalls as a possible source of increased leakage currents.

We characterize the charging behavior of a single quantum dot by measuring its photoluminescence (PL) as a function of an external bias voltage. Excitation is carried out with a continuous-wave laser with a wavelength of 830 nm. The voltage applied between top and back gates of the sample changes the energy difference between the back gate Fermi level and the discrete energy levels of the quantum dot. The PL shows clear Coulomb blockade with a series of plateaus, see Fig. 2.2(c). We assign these plateaus to the neutral exciton X^0 and the charged excitons X^{1-}, X^{2-}, and X^{3-}. All charge plateaus appear in reverse bias, in a range between -0.7 V and -0.4 V. At these bias voltages, the tunneling current through the sample is limited to only a few tens of nA for a mesa size of $\sim 15\,\mathrm{mm}^2$ (see Fig. 2.2(b)), corresponding to a current density of less than $\sim 3\,\mathrm{nA/mm}^2$.

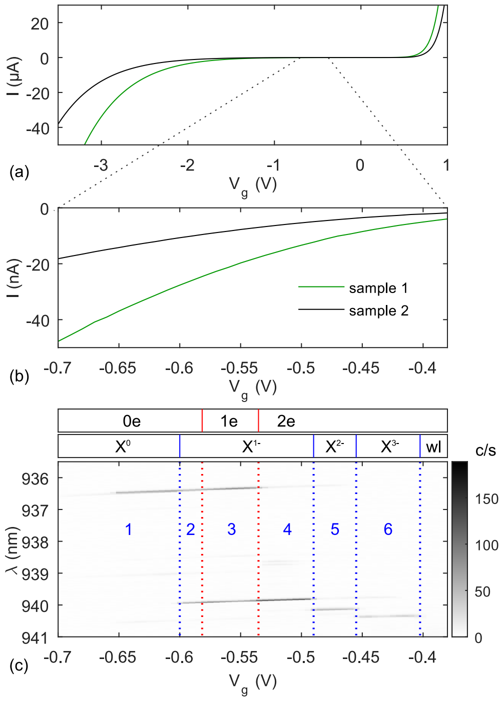

Fig. 2.2: (a) IV-curve of two separate samples. Both IV-curves are measured at 4.2 K and show a typical diode behavior. (b) IV-curve in the voltage regime where excitons of single quantum dots are measured. (c) Photoluminescence (PL) for weak non-resonant excitation (830 nm) as a function of applied bias voltage for a quantum dot in sample 1. The emission of neutral (X^0) and the negatively charged excitons (X^{1-}, X^{2-}, and X^{3-}) is observed. All excitons appear at a low bias voltage where the tunneling current is only several tens of nA. The dotted blue lines indicate the regimes in which the different exciton states become energetically favorable. The dotted red lines indicate the single-electron regime of the quantum dot as measured by resonance fluorescence. Owing to the weak excitation power in PL, the single-electron regime observed in resonance fluorescence coincides with the PL measurement. For high-power non-resonant excitation, the charging steps in the PL can be shifted by optically created space charge.

Our PL-measurements can be interpreted in a majority-minority carrier picture: the optical excitation creates the minority carrier, the hole; the back gate provides majority carriers, electrons. For a 25 nm tunnel barrier (e.g. used in Ref. [38, 79, 92, 112]), electron tunneling is typically much faster than recombination such that once a hole is captured, fast tunneling enables the exciton with the smallest energy to be formed before recombination occurs [12]. Abrupt changes in the PL spectrum as a function of bias result. In this work, the tunnel barrier is larger, 35 nm, and interpretation of the

PL spectrum is slightly more involved.

In the first region of Fig. 2.2(c), the ground state is an empty quantum dot. The lowest energy excited state is X^0. When the quantum dot captures a single hole, it becomes energetically favorable for a single electron to tunnel into the quantum dot, forming an exciton and via recombination a photon at the X^0 wavelength.

The first dashed line between regions 1 and 2 in Fig. 2.2(c) marks the point at which the X^{1-} and X^0 energies cross, while the empty quantum dot remains the ground state of the system. In region 2, electrons begin to tunnel into the quantum dot once it has captured a single hole and the X^{1-} line appears. The fact that the X^0 remains bright at this point, although not as bright as X^{1-}, indicates that the electron tunneling time into the quantum dot is comparable to the X^0 radiative lifetime: recombination can occur before tunneling has created the exciton with the lowest energy. We note that the tunneling rate is large enough that no quenching of the resonance fluorescence of X^{1-} due to an Auger process is expected. The ionization of the quantum dot due to an Auger process has been observed for thicker tunnel barriers [90]. Another ionization channel following a radiative Auger effect will be discussed in chapter 5.

It might appear surprising that the X^0 brightness increases in the regime where the quantum dot ground state is the single-electron state (region 3 of Fig. 2.2(c)). These measurements are carried out in the weak excitation regime where hole capture is significantly slower than exciton recombination. The single-electron ground state implies that X^0 recombination can take place as soon as a hole is captured. We speculate that the presence of an electron in the quantum dot increases the hole capture rate.

In the fourth region, the quantum dot is charged with two electrons in its ground state. Thus, the capture of a single hole enables the X^{1-} recombination. In this region, the intensity of X^0 is small. X^{1-} recombination leaves behind a single electron. If a hole is captured before tunneling takes place, X^0 emission is possible. However, this is unlikely with weak optical excitation (the case here) as electron tunneling is faster than hole capture.

Finally, in regions 5 and 6, the energetically favorable excitons are the X^{2-} and X^{3-} states. These states contain one and two electrons in the quantum-dot *p*-shell, respectively. The tunneling barrier is more transparent for the *p*-shell than for the *s*-shell on account of the higher *p*-shell energy leading to faster tunneling times [114] and, therefore, less overlap between the plateaus measured in PL.

The PL experiment establishes that the transition between the 0 and 1e ground states takes place at $-0.6\,\mathrm{V}$, not exactly at the design value of zero. This can be explained by a slight inaccuracy in the doping concentration of the intermediate *n*-type layer (see appendix B). However, the flat IV-characteristic in reversed bias implies that tunneling currents are still very small at this voltage. The measured IV-characteristic is comparable to a *p-i-n* diode structure of similar thickness [97], but in the latter case charging would take place at large forward bias where tunneling currents are much bigger.

We turn now to resonant excitation of single quantum dots: this measures the exact optical absorption linewidth. A resonance fluorescence measurement of the quantum dot presented in Fig. 2.2(b) is shown in Fig. 2.3(a). The resonant excitation is carried out with a narrow-bandwidth continuous-wave laser, the reflected laser light is suppressed with a cross-polarized detection scheme [83]. We make use of the Stark shift to sweep the quantum-dot transition through the resonance, using the applied bias voltage, while the excitation laser is kept at a constant wavelength. The measurement presented in Fig. 2.3(a) is carried out with a low excitation power corresponding to 22.5 % of the saturation count rate. In the best case, linewidths below $2\,\mu$eV (full width at half maximum) are measured on second time scales. This performance is comparable to that of quantum dots in thick diode structures located far from the GaAs-air interface [38, 39]. Narrow linewidths are reproducibly observed for different quantum dots in both samples (Fig. 2.3(b)). Quantum dot linewidths are highly sensitive to charge noise. This measurement demonstrates forcibly that the level of charge noise in the close-to-surface, *p-i-n-i-n* device is similar to the ultra-low charge noise in the very best far-from-surface, *p-i-n* device. Important for this low charge noise is screening of surface states in a gated structure [38] as well as very low tunneling currents at the operation point of the device.

2.1.5 Electron Spin Pumping

Next, we investigate the spin properties of a quantum dot. We perform optical spin pumping experiments in a magnetic field in the Faraday geometry. The laser wavelength is changed stepwise to map the full Coulomb plateau. The background suppression of the dark-field microscope has a chromatic dependence and is therefore readjusted for each wavelength. In practice, this is carried out by an automatic algorithm that minimizes the intensity of the laser background by adjusting the polarization optics [83]. For a fixed laser wavelength, the bias voltage is swept, sweeping the quantum dot transition with respect to the laser. This gives a linewidth measurement of the X^{1-} exciton, see Fig. 2.4(a). This procedure is repeated for different laser wavelengths giving a full map of the response over the single-electron Coulomb plateau. The results for zero magnetic field and a magnetic field of 0.5 T (Faraday geometry) are shown in Fig. 2.4(a) and Fig. 2.4(b), respectively. Both measurements are done with the same excitation power. In Fig. 2.4(b), the X^{1-}-plateau shows a Zeeman splitting. Furthermore, the resonance

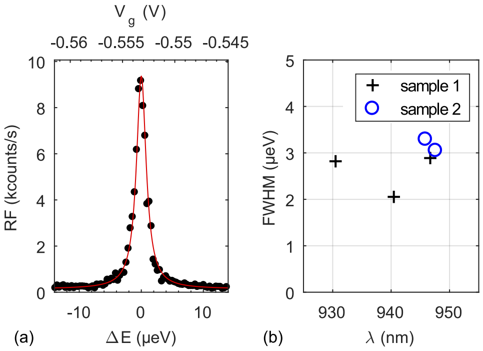

Fig. 2.3: (a) Resonance fluorescence of the singly charged exciton X^{1-} measured on the quantum dot shown in Fig. 2.2(b). The linewidth obtained by fitting a Lorentzian profile (red line) to the data (black circles) is $1.9\,\mu$eV (full width at half maximum). The count rate is 22.5 % of the saturation count rate. (b) Average linewidths across the singly charged exciton plateau for five quantum dots in two separate samples. The linewidths lie reproducibly in the range $2 - 3.5\,\mu$eV.

fluorescence signal disappears in the middle of the plateau. This is the signature of optical spin pumping [15, 23, 115]: the spin is initialized in one of the spin eigenstates.

Spin pumping is interpreted in terms of the level scheme shown in Fig. 2.4(d). There are two strong transitions, the vertical transitions, and two weak transitions, the diagonal transitions. In the Faraday geometry, spin pumping arises due to the weakly allowed diagonal transitions in combination with a long electron spin relaxation time [98]. On driving the $|\uparrow\rangle \leftrightarrow |\uparrow\downarrow, \Uparrow\rangle$ transition, the electron is pumped into the $|\downarrow\rangle$ state via the weak diagonal transition $|\uparrow\downarrow, \Uparrow\rangle \leftrightarrow |\downarrow\rangle$ (green line in Fig. 2.4(d)). The laser is no longer scattered by the quantum dot, and the resonance fluorescence turns off. In the plateau center, the signal is reduced by a factor of $\alpha_r = 40.1 \pm 1.6$ for the red transition, and by a factor of $\alpha_b = 37.6 \pm 1.2$ for the blue transition. In both cases, we take the resonance fluorescence intensity at zero magnetic field as a reference. To quantify the spin initialization we estimate a spin initialization fidelity $F = \sqrt{\langle\uparrow|\,\rho\,|\uparrow\rangle}$ for pumping the red, and $F = \sqrt{\langle\downarrow|\,\rho\,|\downarrow\rangle}$ for the blue transition. The initialization fidelity can be related to the resonance fluorescence via $F = \sqrt{1 - 1/\alpha_{r/b}}$ (see appendix D for details). This way, we estimate initialization fidelities of $F = 98.7\,\%$ for both spins. A significant difference is not expected at 4.2 K and small magnetic fields as the thermal energy is much larger than the Zeeman splitting between the electron spin states. At the edges of the single-electron Coulomb plateau, the resonance fluorescence signal does not disappear. At the plateau edges, co-tunneling with the Fermi sea in the back gate randomizes the

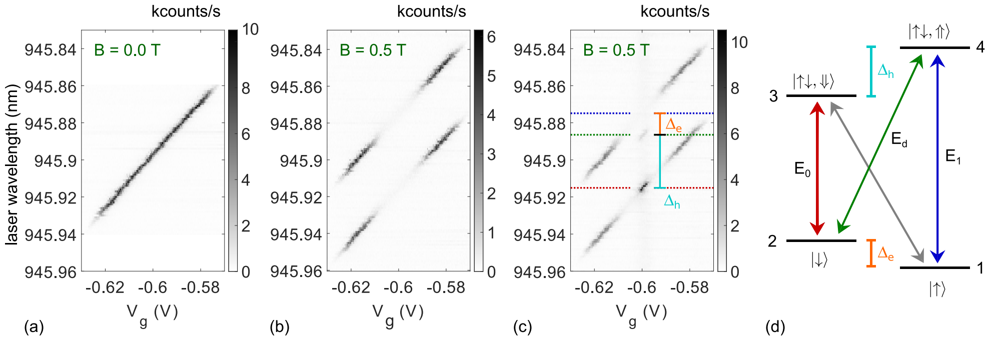

Fig. 2.4: (a) Resonance fluorescence of the singly charged exciton as a function of bias voltage and resonant laser wavelength. The measurement is carried out at zero external magnetic field on a quantum dot in sample 2. (b) Resonance fluorescence of the same quantum dot at a magnetic field of $B = 0.5\,\mathrm{T}$ in the Faraday geometry. At the center of the plateau, the resonance fluorescence signal disappears due to optical spin pumping. (c) Resonant excitation is carried out with two lasers exciting the same quantum dot. The wavelength of the first laser is changed step-wise, whereas the second laser is kept at a constant wavelength of 945.874 nm (indicated by the blue line). The signal reappears when both vertical exciton transitions are excited simultaneously, confirming the presence of optical spin pumping (indicated by the red line). When the second laser is in resonance with the diagonal transition $|\downarrow\rangle \leftrightarrow |\uparrow\downarrow, \Uparrow\rangle$ (indicated by the green line), the resonance fluorescence signal is also enhanced since the second laser pumps the quantum dot back to its bright transition $|\uparrow\rangle \rightarrow |\uparrow\downarrow\,, \Uparrow\rangle$. However, this enhancement is weaker since the corresponding transition is dipole forbidden, i.e. only weakly allowed. The observation of the diagonal transition allows the Zeeman splittings, Δ_e, Δ_h for electron and hole, respectively, to be determined. Note that in (a–c) all lasers are kept at the same power. (d) Level scheme of the quantum dot in the Faraday geometry.

spin rapidly, and spin pumping becomes ineffective [112]. The observation of optical spin pumping in the Faraday geometry confirms that the spin-flip processes which couple the two electron spin states $|\uparrow\rangle$, $|\downarrow\rangle$ are significantly slower than the decay rate of the weakly allowed diagonal transition [23].

To confirm that the observed disappearance of the signal arises due to optical spin pumping, we repeat the experiment with a second laser, a re-pump laser [15]. The second laser has a fixed wavelength of 945.87 nm, the wavelength of the vertical transition $|\uparrow\rangle \leftrightarrow |\uparrow\downarrow, \Uparrow\rangle$ (blue arrow in Fig. 2.4(d)). These measurements are shown in Fig. 2.4(c). The laser powers are kept constant throughout the entire measurement. Two re-pump resonances are observed (marked by red and green dashed lines in Fig. 2.4(d)).

When the first laser, the pump laser, is in resonance with the vertical transition $|\downarrow\rangle \leftrightarrow |\uparrow\downarrow, \Downarrow\rangle$, the electron spin is shelved in the $|\uparrow\rangle$ state. With this laser alone, the resonance fluorescence disappears. However, in the presence of the re-pump laser, the electron spin is driven back into the $|\downarrow\rangle$ state, and the resonance fluorescence reappears: the electron spin ends up in a statistical mixture of the two spin states. Similarly, the system ends up in a mixture of the spin states when the pump laser is stepped into resonance with the weakly-allowed diagonal transition $|\downarrow\rangle \leftrightarrow |\uparrow\downarrow, \Uparrow\rangle$. However, since the diagonal transition is only weakly allowed, the resonance fluorescence is relatively weak in this case. These observations explain the origin and intensity of the two re-pump resonances.

The fact that the diagonal transition $|\downarrow\rangle \rightarrow |\uparrow\downarrow, \Uparrow\rangle$ is visible allows the energies of all three optical transitions to be determined. The energies of the different exciton transitions are denoted as E_1 for the transition $|\uparrow\rangle \rightarrow |\uparrow\downarrow, \Uparrow\rangle$, E_0 for $|\downarrow\rangle \rightarrow |\uparrow\downarrow, \Downarrow\rangle$, and E_d for $|\downarrow\rangle \rightarrow |\uparrow\downarrow, \Uparrow\rangle$ (see Fig. 2.4(d)). The electron and hole Zemann splitting are given by $\Delta_\mathrm{e} = E_1 - E_\mathrm{d}$ and $\Delta_\mathrm{h} = E_\mathrm{d} - E_0$. This allows the magnitude of the electron and hole g-factors to be determined via the relations $\Delta_\mathrm{e/h} = g_\mathrm{e/h}\mu_\mathrm{B}B$. Assuming that the electron g-factor is negative, we find an electron g-factor of $g_\mathrm{e} = -0.55$ and a hole g-factor of $g_\mathrm{h} = 1.37$, values comparable to those in the literature [15, 97, 116].

2.1.6 Conclusions

In conclusion, we have designed a *p-i-n-i-n* diode structure with a thickness of just 162.5 nm. The device enables single-electron charging of embedded self-assembled quantum dots at low bias voltage and with small tunneling currents. The diode is fully compatible with the fabrication of photonic and phononic nanostructures in thin membranes. We demonstrate narrow optical linewidths and optical spin pumping for the close-to-surface quantum dots in the *p-i-n-i-n* diode. These excellent properties will underpin future exploitations of quantum dot spins in functionalized nanostructures.

Appendix A: Analytical Bandstructure Model

We present an analytic calculation of the band structure of the *p-i-n-i-n* diode [109]. To this end, we divide the heterostructure in 5 different regions (Fig. 2.5). The first region (A) is the depletion zone of the p-type top gate, of width w_p and doping concentration n_A, part of layer number 2 in Fig. 2.1(c). The second region (B) is the intrinsic GaAs layer between top gate and an intermediate n-layer (layer 3 in Fig. 2.1(c)). Its width is denoted by L_1. The third region (C) is the intermediate n-layer (layer 4 in Fig. 2.1(c))

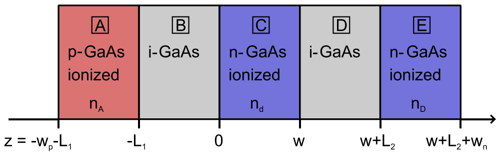

Fig. 2.5: Schematic *p*-*i*-*n*-*i*-*n* diode with labels used in the analytical calculation of the band structure. The letters (A–E) in the frames correspond to the different regions considered in the band structure calculation; the colors indicate the corresponding layers of the diode shown in Fig. 2.1(c).

with a width denoted by w and doping concentration n_d. The fourth region (D) is the subsequent intrinsic region of width L_2 which includes the quantum dot layer (layer 5, 6 in Fig. 2.1(c)). The final region (E) is the depletion zone of the back gate (part of layer 7 in Fig. 2.1(c)). It has a width of w_n and a doping concentration of n_D.

We apply the Poisson equation $\Delta\Phi = -\frac{e \cdot n}{\epsilon\epsilon_0}$ to all five regions (e electron charge, ϵ_0 vacuum permittivity, ϵ relative permittivity of GaAs, and n carrier density). Note that the potential Φ is defined for a positive probe charge and has to be reversed in sign to describe an electron in the conduction band. Together with the constraints that the electric displacement field $-\epsilon\epsilon_0 \cdot \frac{\partial\Phi}{\partial z}$ must be continuous and vanishes at the outer edges of the depletion zones, one obtains the following 5 equations for the electric field in the different regions A–E of the structure:

$$\mathrm{A}: \frac{\partial\Phi}{\partial z} = \frac{e}{\epsilon\epsilon_0} \cdot n_A \cdot (z + w_p + L_1) \tag{2.1}$$

$$\mathrm{B}: \frac{\partial\Phi}{\partial z} = \frac{e}{\epsilon\epsilon_0} \cdot n_A w_p \tag{2.2}$$

$$\mathrm{C}: \frac{\partial\Phi}{\partial z} = \frac{e}{\epsilon\epsilon_0} \cdot (n_A w_p - n_d z) \tag{2.3}$$

$$\mathrm{D}: \frac{\partial\Phi}{\partial z} = \frac{e}{\epsilon\epsilon_0} \cdot (n_A w_p - n_d w) \tag{2.4}$$

$$\mathrm{E}: \frac{\partial\Phi}{\partial z} = \frac{e}{\epsilon\epsilon_0} \cdot (n_D \cdot (L_2 + w - z) + n_A w_p - n_d w) \tag{2.5}$$

Integration of the electric field in all 5 regions of the diode yields the potential drop ΔV

between top gate and back gate:

$$\begin{aligned}\frac{\epsilon\epsilon_0}{e}\cdot\Delta V =&\frac{\epsilon\epsilon_0}{e}\cdot(V_0-V_{\text{bias}})\\ =&\frac{n_A}{2}w_p^2+n_Aw_pL_1+n_Aw_pw-\frac{n_d}{2}w^2\\ &+L_2\cdot(n_Aw_p-n_dw)-\frac{n_D}{2}w_n^2\\ &+w_n\cdot(n_Aw_p-n_dw)\end{aligned}\tag{2.6}$$

where V_0 is the built-in voltage of the diode and V_{bias} is the externally applied bias voltage. For high doping concentrations when top and back gate are degenerately doped, the built-in voltage is given by: $e\cdot V_0 = E_{\text{gap}}+E_{\text{F}}^{\text{e}}+E_{\text{F}}^{\text{h}}$ where E_{gap} is the band gap of GaAs and $E_{\text{F}}^{\text{e/h}}$ is the Fermi level for electrons in the back gate and holes in the top gate, respectively ($E_{\text{F}}^{\text{e/h}}=\hbar^2/2m_{e/h}^*\cdot\left(3\pi^2n\right)^{2/3}$). The condition that the entire device is charge neutral,

$$-n_A\cdot w_p+n_d\cdot w+n_D\cdot w_n=0,\tag{2.7}$$

in combination with Eq. 2.6, determines the widths of the depletion zones w_p and w_n:

$$\begin{aligned}w_p =&\frac{1}{a_1}\cdot\left(a_2+\sqrt{a_2^2+2a_1a_3}\right)\\ &a_1=n_A+\frac{n_A^2}{n_D}\\ &a_2=-n_AL_2-n_Aw-n_AL_1+\frac{n_An_d}{n_D}w\\ &a_3=n_dL_2w+\frac{n_dw^2}{2}+\frac{\epsilon\epsilon_0}{e}\Delta V-\frac{n_d^2w^2}{2n_D}\\ w_n =&\frac{1}{n_D}\cdot(n_Aw_p-n_dw)\end{aligned}\tag{2.8}$$

Using Eq. 2.8 the potential as a function of vertical position inside the heterostructure is obtained by integration over Eq. 2.1–2.5. In particular, the electric field at the position of a quantum dot is given by Eq. 2.4.

Appendix B: Bias Voltage of Coulomb Plateaus

We present a possible explanation for the fact that the 0-1 electron transition takes place at a bias voltage of $V_{\text{bias}}=-0.6\,\text{V}$ and not around zero bias as intended. Deviations of heterostructure or quantum dot parameters can shift this transition voltage. The part of the heterostructure that influences the 0-1e transition voltage most strongly is the intermediate n-type layer. A deviation in its thickness or its doping concentration changes the potential of the quantum dot levels with respect to the Fermi-reservoir. The layer thickness can be controlled rather precisely in MBE-growth. Therefore, we simulate the 0-1e transition voltage as a function of the doping concentration of the intermediate n-layer. The ratio between doping of the intermediate n-layer and doping of the back gate is kept constant for this estimation since a systematically different n-doping would affect both layers. We use the analytical model and also numerical band structure simulations (nextnano). We take a single electron confinement energy of the quantum dot of $E_\mathrm{c} = 134\,\mathrm{meV}$ [117] and vary the doping concentration (Fig. 2.6(a)). The 0-1 electron transition voltage obtained numerically assuming ohmic boundary conditions agrees well with the analytical model but is systematically slightly larger. We explain this by the fact that the numerical Poisson equation solver takes into account a charge overspill of back gate electrons into the intrinsic region (see Fig. 2.1(c)). This effect lifts the conduction band energy slightly at the location of the quantum dots. In contrast, the analytical model assumes abrupt depletion regions. A numerical simulation taking into account surface depletion via Schottky barriers of 1 V gives comparable results (see Fig. 2.6). Surface effects are not considered in the analytical model. All this work predicts a 0-1e transition voltage of about $-0.1\,\mathrm{V}$ for the nominal doping concentration $n_d = 2.0 \cdot 10^{18}\,\mathrm{cm}^{-3}$.

Fig. 2.6(b) shows the 0-1 electron transition voltage as a function of the quantum dot single electron confinement energy E_c keeping the doping at the nominal value of $n_d = 2.0 \cdot 10^{18}\,\mathrm{cm}^{-3}$. The dashed black line indicates a single electron confinement energy of $E_c = 134\,\mathrm{meV}$ that has been reported in literature [117]. One can see that the shift of the 0-1e transition voltage to $-0.6\,\mathrm{V}$ cannot be explained by any realistic single electron confinement potential of the quantum dot. This suggests that the most likely explanation for the shift of the 0-1e transition to $-0.6\,\mathrm{V}$ is a deviation of the n-doping from the nominal value. An increase by about 30 % reproduces the experimental result taking $E_\mathrm{c} = 134\,\mathrm{meV}$ (Fig. 2.6(a)). A reduced doping of the p-type top gate would also shift the 0-1e transition to more negative bias voltages. However, the effect of an under-doped p-layer is smaller and cannot explain the shift to $-0.6\,\mathrm{V}$ completely.

Appendix C: Supplementary Experimental Data

In the previous sections, we presented narrow linewidths for a quantum dot in sample 1; optical spin pumping is demonstrated for a quantum dot in sample 2. To illustrate that the measurements are reproducible on different quantum dots, we show in Fig.

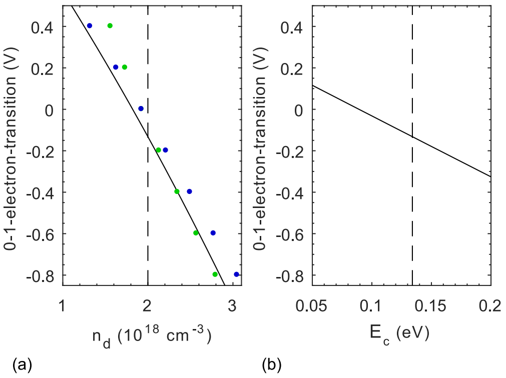

Fig. 2.6: (a) The calculated shift of the 0-1 electron charging transition as a function of the doping of the intermediate n-type layer n_d. The back gate doping is scaled correspondingly ($n_d = n_D$). The black curve shows the result of the analytical calculation (see appendix A); the green points represent the results of band structure simulations including surface depletion; the blue points represent the results of band structure simulations assuming ohmic contacts. (b) Shift of the 0-1 electron charging transition as a function of the single electron confinement energy E_c.

2.7 a typical linewidth for the quantum dot in sample 2, and demonstrate optical spin pumping for the quantum dot in sample 1.

Appendix D: Analysis of Spin Pumping

Here we show how resonance fluorescence of the singly charged exciton is used to obtain spin initialization fidelities. In section 2.1.5, the initialization fidelity was connected to the ratio $\alpha_{r/b}$ between the resonance fluorescence intensity when no spin pumping is present (at B = 0 T) and the resonance fluorescence intensity when spin pumping is active (at B = 0.5 T).

We give a derivation of this relation in a rate-equation picture. At zero magnetic field, both allowed transitions $|{\downarrow}\rangle \leftrightarrow |{\uparrow\downarrow}, {\Downarrow}\rangle$ and $|{\uparrow}\rangle \leftrightarrow |{\uparrow\downarrow}, {\Uparrow}\rangle$ are degenerate (see Fig. 2.4(d)). In the steady state, the ratio between occupation of upper and lower levels is given by:

$$\frac{N_3^{B=0}}{N_2^{B=0}} = \frac{N_4^{B=0}}{N_1^{B=0}} = \frac{\Gamma}{\Gamma + \gamma + \gamma_D} \equiv b \tag{2.9}$$

with $N_3^{B=0} = N_4^{B=0}$ the occupation of the excited states and $N_2^{B=0} = N_1^{B=0}$ the occupation of the ground states (see Fig. 2.4(d) for labels). Γ denotes the stimulated emission/excitation rate, γ the spontaneous emission rate via the dipole-allowed vertical

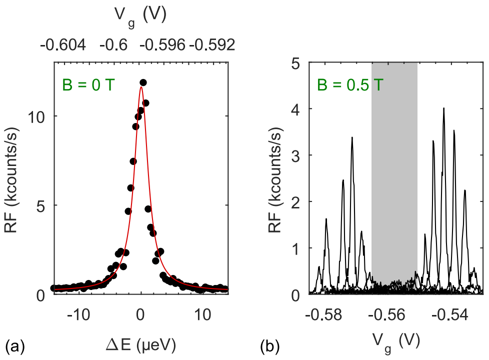

Fig. 2.7: (a) Resonance fluorescence of a quantum dot in sample 2 (the one from Fig. 2.4). The linewidth obtained by a Lorentzian fit (red curve) is 2.7 μeV for a power corresponding to 27 % of the saturation count rate. (b) Optical spin pumping on the singly charged exciton for a quantum dot in sample 1 (the one from Fig. 2.3) at a magnetic field of 0.5 T. The different peaks correspond to resonance fluorescence measurements for different excitation wavelengths. The gray shaded region indicates the regime where the spin pumping dominates over co-tunneling processes and the resonance fluorescence signal thus disappears. At the plateau edges, the co-tunneling dominates and resonance fluorescence reappears.

transitions, and γ_D the spontaneous emission rate via the diagonal transitions. The resonance fluorescence intensity $\mathrm{RF}^{B=0}$ is directly connected to the occupation of the upper states: $\mathrm{RF}^{B=0} = \tilde{c}\left(N_3^{B=0} + N_4^{B=0}\right)$. The combination of Eq. 2.9 and the normalization condition $\sum_{i=1}^{4} N_i^{B=0} = 1$ yields the equation:

$$\mathrm{RF}^{B=0} = \tilde{c}\left(N_3^{B=0} + N_4^{B=0}\right) = \frac{\tilde{c}}{1 + 1/b}. \tag{2.10}$$

In finite magnetic field, the transitions $|\downarrow\rangle \leftrightarrow |\uparrow\downarrow, \Downarrow\rangle$ and $|\uparrow\rangle \leftrightarrow |\uparrow\downarrow, \Uparrow\rangle$ are split in energy. We take the case when the red-shifted transition $|\downarrow\rangle \leftrightarrow |\uparrow\downarrow, \Downarrow\rangle$ is driven by a laser field whereas the other one is not addressed. This means that $N_4^{B\neq 0} = 0$ and the resonance fluorescence is connected to the occupation of just one upper level: $\mathrm{RF}^{B\neq 0} = \tilde{c}N_3^{B\neq 0}$. In the steady state, the ratio of $N_3^{B\neq 0}$ and $N_2^{B\neq 0}$ is also given by the relation $N_3^{B\neq 0}/N_2^{B\neq 0} = b$, see Eq. 2.9. In combination with the normalization condition $\sum_{i=1}^{3} N_i^{B\neq 0} = 1$ this leads to:

$$\mathrm{RF}^{B\neq 0} = \tilde{c}N_3^{B\neq 0} = \tilde{c}\frac{1 - N_1^{B\neq 0}}{1 + 1/b}. \tag{2.11}$$

The combination of Eq. 2.10 and Eq. 2.11 directly connects the occupation $N_1^{B\neq 0}$ of the

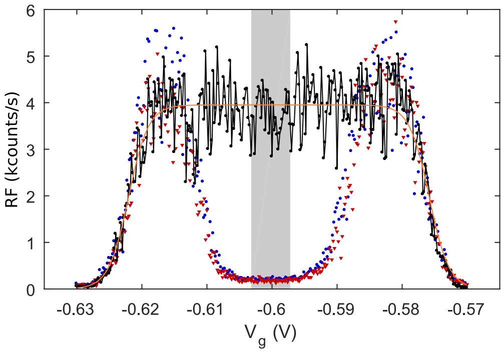

Fig. 2.8: Resonance fluorescence intensity along the single electron Coulomb plateau for the quantum dot shown in Fig. 2.4. The black curve shows data at 0.0 T divided by a factor of two (to give a signal per spin); the red triangles (blue circles) show the data at 0.5 T for the lower (higher) frequency Zeeman transitions. To obtain the ratio between the plateau intensities with and without spin pumping, the corresponding signals are averaged in the plateau center (gray shaded region). The orange curve is a fit of the data at $B = 0.0\,\mathrm{T}$ to Eq. 2.13.

ground state with the resonance fluorescence intensities:

$$N_1^{B\neq 0} = 1 - \frac{1}{\alpha_r}, \text{ with } \alpha_r = \frac{\mathrm{RF}^{B=0}}{\mathrm{RF}^{B\neq 0}}. \tag{2.12}$$

This equation shows how the initialization fidelity can be deduced from the resonance fluorescence measurements.

The corresponding values of $\alpha_{r/b}$ are determined in the following way. For every bias voltage, the maximum resonance fluorescence signal (Fig. 2.4) is determined. Results are plotted in Fig. 2.8 for the two transitions at 0.5 T (Zeeman-split) and for the single transition at zero magnetic field. The signals are averaged over a small region in the Coulomb plateau center to determine accurately the strength of the resonance fluorescence in the regime where optical spin pumping dominates over spin co-tunneling. In this way, we determine the intensity ratio $\alpha_{r/b}$ between the signal at zero magnetic field and the signal at $B = 0.5\,\mathrm{T}$.

Appendix E: Lever Arm Approximation

On increasing the bias voltage from the center of the Coulomb plateau, the X^{1-} resonance fluorescence drops once it becomes electrically favorable for a second electron to tunnel into the quantum dot. On the other hand, on decreasing the bias voltage from the plateau center, the X^{1-} resonance fluorescence drops once it becomes energetically favorable for the electron to tunnel out of the quantum dot. In both cases, the edges of the X^{1-} plateau are not abrupt since the electron occupation in the back gate is determined by a thermally smeared Fermi distribution. At the plateau edges, the X^{1-} resonance fluorescence signal maps the Fermi distribution of the back gate and is well described by a 2-sided Fermi-distribution:

$$I_{\mathrm{RF}}(V) = I_0 \cdot \frac{1}{1+\exp\left(\frac{e\cdot(V-V_1)}{\lambda_{\mathrm{diff}} k_{\mathrm{B}} T}\right)} \cdot \frac{1}{1+\exp\left(\frac{e\cdot(V_2-V)}{\lambda_{\mathrm{diff}} k_{\mathrm{B}} T}\right)} \tag{2.13}$$

where $k_{\mathrm{B}}T$ is the thermal energy, V_1 and V_2 specify the bias voltage at the plateau edges, and I_0 is the intensity in the plateau center. The variable λ_{diff}, the differential lever arm, is defined by $\lambda_{\mathrm{diff}} = e \cdot \left(\frac{\partial \Phi_{\mathrm{QD}}}{\partial V_{\mathrm{bias}}}\right)^{-1}$ where Φ_{QD} is the energy difference between back gate Fermi-energy and the quantum dot single electron level. Thus, λ_{diff} parameterizes how the potential of the quantum dot changes with bias voltage V_{bias}.

We determined the differential lever arm as a function of the bias voltage by using numerical band structure simulations. We find a value of $\lambda_{\mathrm{diff}} = 4.17$ at a bias voltage of $-0.6\,\mathrm{V}$. A slightly increased n-doping explaining the 0-1e transition at this bias is taken into account (see appendix B). In the simulation, the lever arm is to a good approximation constant over the single electron Coulomb plateau. We fit the model described by Eq. 2.13 using the position of the plateau edges V_1, V_2 and the plateau intensity I_0 as the only fit parameters. The temperature 4.2 K as well as the differential lever arm are fixed parameters in the fit. The fit describes the experimental data very well (Fig. 2.8). This is further evidence that the electrical properties of our sample are well understood.

We note that the lever arm is often defined as $\lambda_{\mathrm{geo}} = L/L_{QD}$ (geometrical lever arm) and $\lambda_{\mathrm{el}} = e \cdot \left(\frac{\Phi_{\mathrm{QD}}}{V_0 - V_{\mathrm{bias}}}\right)^{-1}$ (electrical lever arm). For diode structures with little band bending, the three parameters λ_{diff}, λ_{el}, and λ_{geo} are to a good approximation equivalent [23, 112, 118]. Obviously, this is not the case for the heterostructure presented here as a result of band bending in the *p*-*i*-*n*-*i*-*n* structure.

Appendix F: Sample Fabrication

A schematic of the sample is shown in Fig. 2.9. To fabricate devices from the wafer material, a mesa structure is defined by means of optical lithography. The top gate is etched away around this mesa so that an independent contact to the back gate can be made. A wet chemical process with a diluted mixture of sulfuric acid and hydrogen peroxide ($1\,\mathrm{H_2SO_4} : 1\,\mathrm{H_2O_2} : 50\,\mathrm{H_2O}$) was used for the etching. Subsequently, a contact

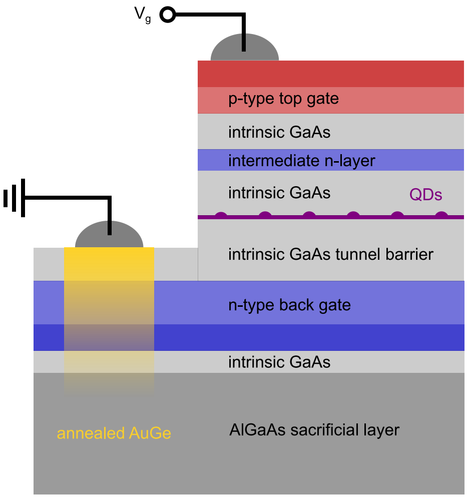

Fig. 2.9: Schematic of the sample. To make electrical contacts, the top gate is removed in part of the sample by wet chemical etching. An AuGe-contact (yellow) is annealed into the back gate. The top and the back gate are contacted with silver paint.

pad of Au/Ge/Ni is evaporated onto the new etched surface and then annealed at 420 °C resulting in an ohmic contact to the back gate [119]. In the next step, we evaporate a pad of 3 nm titanium followed by 7 nm of gold on a small part ($\sim 1\,\text{mm}^2$) of the top gate using a shadow mask. Making electrical contacts via standard bonding processes requires careful adjustment of the bonding parameters to avoid any damage, especially on very thin samples. On account of the small distance between the top- and the back gate in this device, standard bonding processes were avoided as a precautionary measure. Instead, the electrical contacts to the gates were made by affixing the wires to the bond pads with silver paint, a method with which we reproducibly achieved good contacts.

2.1.7 Application of the p-i-n-i-n-Diode in Nanostructured Devices

The p-i-n-i-n-diode has been successfully used as a platform for quantum dots in nanostructured devices [107, 120]. The fabrication of nanobeam-waveguides and nanomechanical resonators has been done using the method described in Ref. [111]. The fabrication involves patterning a soft-mask via e-beam lithography followed by reactive-ion etching. The p-i-n-i-n-diode is grown on top of a $\sim 1\ \mu$m thick AlGaAs layer that can be selectively etched with HF or HCl. Before the etching, electrical contacts are protected by photoresist. Selective etching with HF is done in the absence of light to avoid photo-induced erosion of the p-type top gate [121], etching with HCl has to be done at low temperatures to provide selective etching of AlGaAs [122]. In both cases, the device performance after fabrication is very good: narrow quantum dot linewidths in combination with optical spin-pumping are routinely achieved. The *p*-*i*-*n*-*i*-*n*-diode structures are fully compatible with the fabrication of nano-engineered devices.

2.2 Issues and Possible Improvements

Quantum dots in a *p*-*i*-*n*-*i*-*n*-diode show narrow linewidths and excellent spin properties for the negatively charged exciton, X^{1-}. An issue is that the linewidth of the neutral exciton, X^0, turns out to be systematically worse [121]. We suspect that this issue is associated with the ionized intermediate *n*-layer that is silicon-doped. Silicon-doping of GaAs provides free electrons as the group 4 silicon occupies mostly lattice sites of the group 3 gallium. However, a small amount of As lattice sites are occupied by silicon as well, which leads to free states for holes [123]. For the X^{1-}, the hole is strongly bound to the quantum dot due to the presence of an additional electron. For the X^0, this is not the case, and the hole might tunnel to one of the few hole states in the intermediate *n*-layer. This effect would give rise to additional charge noise in case of the X^0. An attempt to solve this problem could be to place an additional AlGaAs barrier between quantum dots and intermediate *n*-layer.

Simple *p*-*i*-*n*-diodes have performed better in this respect so far. Close to transform-limited linewidths, high single-photon purity, and indistinguishability have been achieved on X^0, X^+ for quantum dots in a nanostructured *p*-*i*-*n* diode [20, 124]. For deterministic charge control of a quantum dot, the corresponding design is potentially disadvantageous. The transition from neutral to charged exciton appears at above 1 V forward bias at a significant current.

The *p*-*i*-*n*-*i*-*n*-concept works well for X^{1-}. It has been shown that the spin dephasing time of the positively charged exciton, X^{1+}, is significantly better due to the *p*-type Bloch-wavefunction of the hole [17]. Therefore, it would be desirable to have an alternative for the *p*-*i*-*n*-*i*-*n*-diode that allows locking the quantum dot charge state to a single hole rather than a single electron. Unfortunately, a *p*-*i*-quantum-dot-*i*-*p*-*i*-*n* diode would suffer from the problem that quantum dots are grown on top of a carbon *p*-doped layer. Under these conditions, the overall material quality and the quantum dot properties turned out to be reduced [125]. Alternative ways of reducing the built-in filed at the quantum dot position are conceivable. When putting a material with a low dielectric response (vacuum in the extreme case) between the top and the back gate, most of the built-in potential drops in this layer rather than in the GaAs.

Chapter 3

Excitons in Quantum Dots without Electron Wetting Layer States

This section is partly adapted from Ref. [91]: "Excitons in InGaAs Quantum Dots without Electron Wetting Layer States", Matthias C. Löbl, Sven Scholz, Immo Söllner, Julian Ritzmann, Thibaud Denneulin, András Kovács, Beata E. Kardynał, Andreas D. Wieck, Arne Ludwig, and Richard J. Warburton, Communications Physics **2**, 93 (2019).

Abstract: The Stranski-Krastanov growth-mode facilitates the self-assembly of quantum dots (QDs) by using lattice-mismatched semiconductors, for instance, InAs and GaAs. These QDs are excellent photon emitters: the optical decay of QD-excitons creates high-quality single-photons which can be used for quantum communication. One significant drawback of the Stranski-Krastanov mode is the wetting layer. It results in a continuum close in energy to the confined states of the QD. The wetting-layer-states lead to scattering and dephasing of QD-excitons. Here, we report a slight modification to the Stranski-Krastanov growth-protocol of InAs on GaAs which results in a radical change of the QD-properties. We demonstrate that the new QDs have no wetting-layer-continuum for electrons. They can host highly charged excitons where up to six electrons occupy the same QD. Additionally, single QDs grown with this protocol exhibit optical linewidths matching those of the very best QDs making them an attractive alternative to conventional InGaAs QDs.

3.1 Introduction

InGaAs quantum dots (QDs) grown in the Stranski-Krastanov (SK) mode are excellent photon emitters. Individual QDs provide a source of highly indistinguishable single-photons [13, 14, 20, 21, 22, 126] and a platform for spin-photon and spin-spin entanglement [27, 28, 127]. Their solid-state nature enables the integration of QDs in on-chip nanostructures such as photonic crystal cavities or waveguides [10, 107, 120, 128, 129, 130]. In some respects, a QD can be considered as an artificial atom. However, this approximation is often too simplistic. Unlike a real atom in free space, an exciton (a bound electron-hole pair) in a QD can couple to further degrees of freedom in its solid-state environment, for instance, phonons [25, 131, 132, 133, 134] and nuclear spins [17, 33, 46, 51, 99, 135, 136]. One problematic source of unwanted coupling is the so-called wetting layer (WL) [35, 76, 86, 137]. The WL is a two-dimensional layer lying between all QDs. It is an inherent feature of SK-growth.

On account of the confinement in the growth direction, there is an energy gap between the WL-continuum and QD-electron and QD-hole states. However, this gap protects the QD-electrons and -holes from coupling to the WL only to a certain extent. The gap vanishes for a QD containing several electrons due to the on-site Coulomb repulsion; the energy gap can be bridged by carrier-carrier and carrier-phonon scattering [35, 138]. Furthermore, the gap is not complete: a low energy tail of the WL-continuum can extend to the QD-confined-states [139, 140, 141, 142]. The result is that the WL has negative consequences for quantum applications: Multi-electron states of a QD hybridize with extended states of the WL [35, 76, 143], severely limiting the prospects for using multi-electron states as qubits, for instance, the four-electron qubit proposed in Ref. [144]. A parasitic coupling between a QD and an off-resonant cavity [145, 146] can be caused by QD–WL Auger processes [147, 148]. The low-energy tail of WL-states [139, 140, 141, 142] leads to damping of exciton Rabi oscillations [137, 149, 150] and enhanced exciton-phonon scattering [151]. Finally, the WL limits applications of small QDs where the QD-WL energy gap is small [152]. Such QDs are useful for a hybrid system of QDs and Cs-atoms [153, 154].

We show here that the QD-properties can be radically altered when WL-states are absent. Electron WL-states are removed by a simple modification to the SK-growth: InGaAs QDs are overgrown with a monolayer of AlAs [155, 156, 157, 158]. On the nano-scale, we propose that the absence of electron WL-states is related to the large bandgap of AlAs. Changes regarding the QD-properties are drastic: we observe highly charged excitons with narrow optical emission where up to six electrons occupy the conduction band shells of the QD – a novelty for QDs in the considered wavelength regime. The QD-potential is deepened, and hybridization with any WL-continuum is absent. Furthermore, the QDs have close-to transform-limited optical linewidths at low temperature, a very sensitive probe of the material quality [38]. Whenever the WL limits the QD-performance [137, 145, 147, 148, 149, 151], we propose that conventional SK QDs can be profitably replaced with their no-electron WL-counterparts.

3.2 Sample Growth and Ensemble Measurements

The QDs are grown by molecular beam epitaxy on a GaAs-substrate with (001)-orientation. The first monolayer of InAs deposited on GaAs (at 525 °C) adopts the GaAs lattice constant. After deposition of 1.5 monolayers, the strain mismatch between InAs and GaAs leads to island formation [67] (Fig. 3.1(a),(b)). These islands become optically-active QDs upon capping with GaAs. A two-dimensional InAs layer remains, the WL. This is the widely used SK self-assembly process.

Here, the InAs islands are capped initially with a single monolayer of AlAs, which has a higher bandgap than GaAs (Fig. 3.1(c)). Subsequently, a capping layer of 2.0 nm GaAs is grown (at 500 °C) (Fig. 3.1(d)). The additional AlAs monolayer is the only change of the standard SK protocol. For some samples, a so-called flushing step [68] is made following the growth of the GaAs-cap (increase of temperature to 630 °C) (Fig. 3.1(e)). With or without flushing, the heterostructure is completed with overgrowth of GaAs (Fig. 3.1(f)).

To determine the QD-structure post-growth, we carried out scanning transmission electron microscopy (STEM). Fig. 3.1(g) is a high-resolution high-angle annular dark-field (HAADF) STEM-image where the contrast is related to the atomic number. The QD is the $\sim$ 3 nm high and $\sim$ 30 nm wide bright feature close to the center of the image. The complete images with an atomic resolution demonstrate that the entire structure is defect-free (see appendix A). The WL consists of InGaAs with a monolayer of AlAs contained within it. The AlAs capping layer can be clearly made out as a darker region surrounding the QD. Energy-dispersive X-ray spectroscopy (EDX) confirms the WL composition: indium atoms are found over a $2-3$ nm thick region, yet the aluminum atoms are located within a 1 nm thick layer (Fig. 3.1(h)). These features point to highly mobile In atoms yet weakly mobile Al atoms under these growth conditions [159]. The overall thickness of the modified WL is similar to the WL of standard InGaAs QDs [160]. The presence of In-atoms above the AlAs-layer is most likely due to In-segregation. This effect is illustrated in Fig. 3.1(c-e). Contrary to results in Ref. [156], the STEM-image does not indicate a transition to a Volmer-Weber growth.

We probe the electronic states initially by photoluminescence (PL) experiments. Fig. 3.1(i) shows ensemble PL from QDs grown with and without the AlAs-cap, in both cases without a flushing step. The spectra reveal the different shells (s, p, d) of the QDs. For the standard QDs, PL from the WL can be observed at $\sim$ 925 nm, emission at lower wavelength is from bulk GaAs. In contrast, for the AlAs-capped QDs, the WL PL disappears. This is the first evidence for the absence of carrier confinement in the

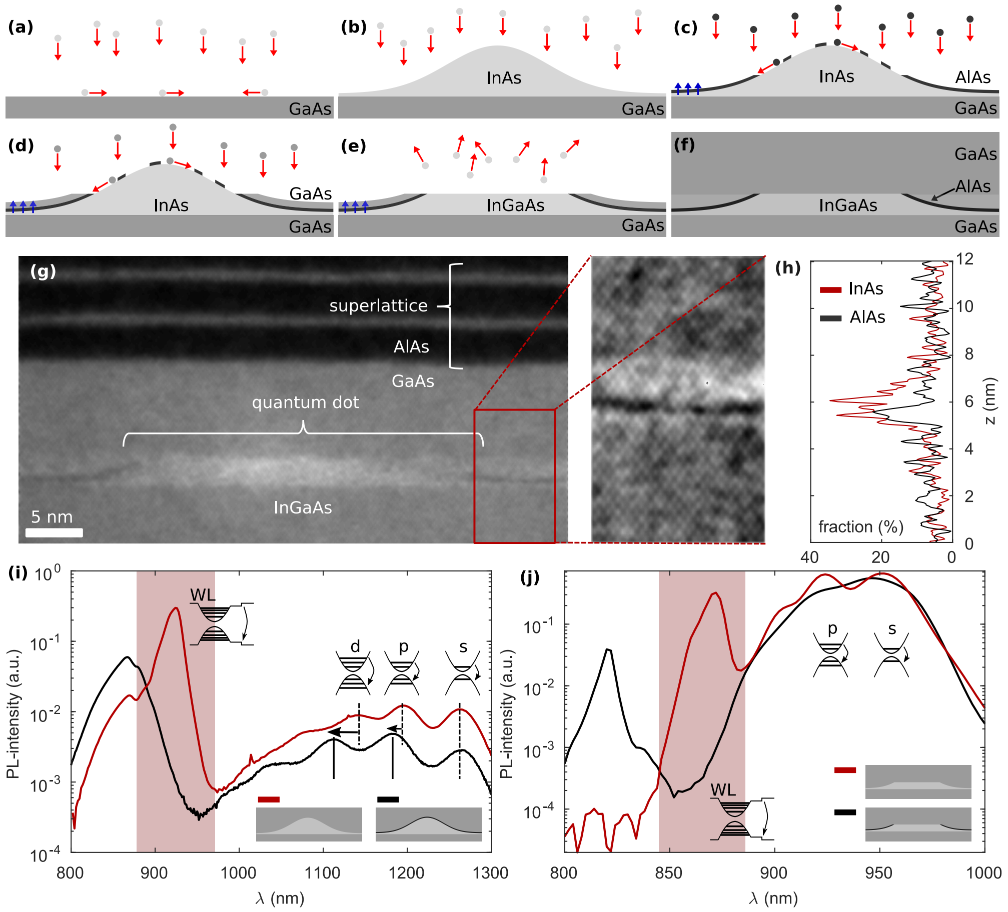

Fig. 3.1: **Growth and characterization of the quantum dots.** (a-f) Schematic illustration of the quantum dot (QD) growth. (a) InAs is deposited on a GaAs-surface. (b) After deposition of ∼ 1.5 monolayers of InAs, strain-driven QD-formation takes place. The QDs are capped with a monolayer of AlAs (c) and 2 nm GaAs (d). During these steps, segregation of In atoms takes place (blue arrows). The segregation leads to a wetting layer (WL) which is an alloy of GaAs, InAs, and AlAs. (e) The top part of the capped QD evaporates at 630°C (flushing step). (f) The flushed QDs are overgrown with GaAs. (g) Scanning transmission electron microscopy image of a flushed QD. InAs appears bright, AlAs dark. (h) Chemical composition of the WL measured by spatially resolved energy-dispersive X-ray (EDX) spectroscopy at a location without a QD (different location to (g) but nominally the same). (i) Ensemble photoluminescence (PL) at room temperature from a sample with unflushed, standard InGaAs QDs (red curve) and unflushed, AlAs-capped InGaAs QDs (black curve). The WL PL (highlighted by the red band) dominates the spectrum. The QD PL appears in the regime $1000-1300$ nm. The QD-shells are labeled. (j) Ensemble-PL at 77 K from a sample with flushed, standard InGaAs QDs (red curve) and flushed, AlAs-capped InGaAs QDs (black curve). The flushing blue-shifts the QD-ensemble to $\sim 900-980$ nm.

modified WL. We come to the same conclusion on flushed QDs for which the ensemble-PL is blue-shifted from 1000 – 1300 nm to ∼ 900 – 980 nm (Fig. 3.1(j)). Without the AlAs-capping, there is strong emission from the WL at ∼ 875 nm. For the AlAs-capped QDs, WL emission is not observed.

3.3 Photoluminescence as a Function of Gate Voltage

The ensemble-PL measurements do not distinguish between electron and hole confinement. We make this distinction by single-QD measurements. The particular concept is to probe the QD- and WL-electron-states by gradually lowering the energy of the states with respect to the Fermi energy of a tunnel-coupled [23, 112, 114, 149] Fermi sea. The QD is small enough to exhibit pronounced Coulomb blockade: electrons from the Fermi sea are added one-by-one and the QD-states are filled according to Hund's rules [35, 79]. A hole in the QD is provided by optical excitation with an above band laser (750 nm). We focus on flushed QDs, both without and with the AlAs capping layer.

For a standard InGaAs QD, PL as a function of gate voltage is shown in Fig. 3.2(a). The plateaus correspond to different charge states of the QD-exciton (Fig. 3.2(b)): in the presence of a hole, electrons fill the QD-shells sequentially. The standard QD shows charging of the neutral exciton X^0 to a net charge of $-3e$, the exciton X^{3-} containing a total of four electrons and one hole. At higher gate voltage, the QD PL disappears. This is a sign that the WL becomes occupied [79, 86, 143, 161, 162].

The PL from the AlAs-capped QD is strikingly different. Charging beyond X^{3-} to X^{4-} and X^{5-} takes place (Fig. 3.2(c)). The X^{5-} contains a total of six electrons with fully occupied s- and p-shells. This is a novelty for QDs in this wavelength regime (960 nm). Further, even the X^{4-} and X^{5-} result in sharp emission lines. There is no rapid loss of intensity or rapid increase in linewidth at high gate voltages. This measurement points to, first, a deep confinement potential, sufficiently deep to accommodate six electrons despite the strong Coulomb repulsions, and second, the absence of WL-states for electrons.

At high positive bias, PL also appears at ∼ 830 nm (see Fig. 3.6(b)), highly blue-shifted with respect to the QD PL, and close to the bandgap of GaAs. This PL line has a very strong Stark shift allowing us to identify it as a spatially indirect transition [85, 86] from an electron in the Fermi sea with a hole in the WL. From this line, we can, therefore, extract the properties of the WL in the valence band. We find that the AlAs-capped QDs have a valence band WL with ionization energy 19 meV with respect to the top of the GaAs valence band (see appendix B). This ionization energy is reduced

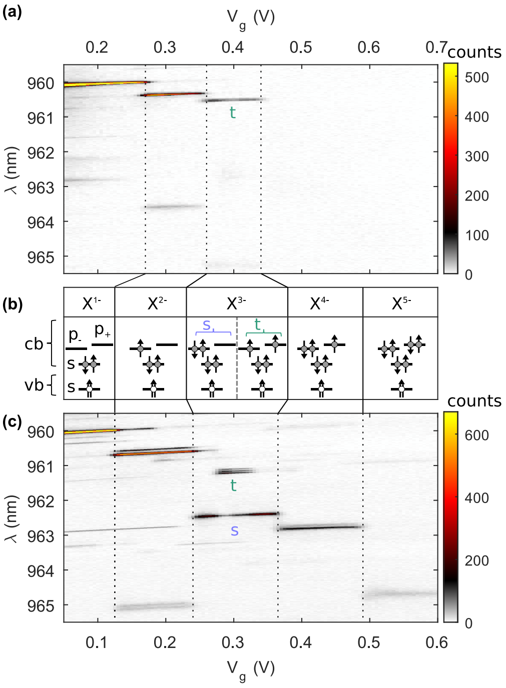

Fig. 3.2: **Photoluminescence (PL) as electron states are sequentially filled.** (a) PL counts versus gate voltage on a single, standard, flushed InGaAs quantum dot (QD). The plateaus correspond to Coulomb blockade [79]. (b) QD-shells and their occupation for the different exciton complexes. The triply charged exciton X^{3-} has two low-lying states: a singlet (blue: s) or a triplet (green: t). (c) PL counts versus gate voltage on a single, AlAs-capped, flushed InGaAs QD. In the absence of wetting layer states for electrons, the X^{3-} singlet (s) and triplet (t) as well as the highly charged exciton complexes X^{4-} and X^{5-} appear.

with respect to the WL of standard InGaAs QDs (ionization energy $\sim$ 30 meV). The AlAs-cap eliminates any bound WL-states in the conduction band and pushes the bound WL-states in the valence band towards the GaAs valence band edge.

The full theoretical explanation for the absence of electron WL-states requires consideration of strain [163] and, possibly, a treatment beyond the envelope wavefunction approximation [164]. This is left for future investigations.

3.4 Triply-Charged Excitons

For standard InGaAs QDs (Fig. 3.3(a)) and AlAs-capped QDs (Fig. 3.3(b)), we measure PL of the X^{3-}-exciton as a function of the magnetic field parallel to the growth direction.

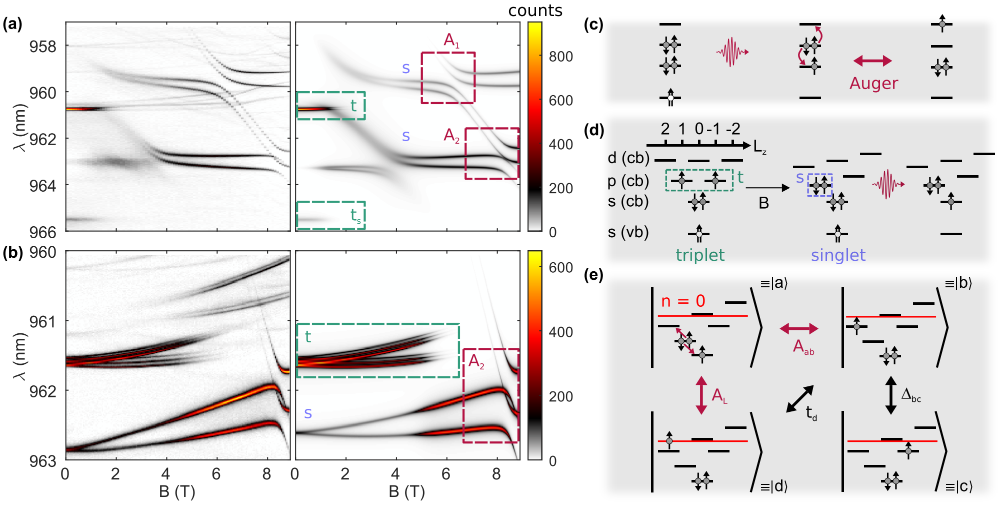

Fig. 3.3: **Triply-charged exciton as a probe of the quantum dot (QD) and the wetting layer (WL) states.** (a) X^{3-} counts as a function of the magnetic field for a standard InGaAs QD (measurement and simulation). (b) As (a) but for an AlAs-capped QD. Note that the line appearing at ~ 5 T and wavelength ~ 961 nm arises from X^{2-}, not X^{3-}. (c) The optical decay process of the X^{3-} singlet. Following photon emission, the p-shell is doubly occupied yet there is a vacancy in the s-shell. This turns on an Auger-like coupling to a state in which a high-lying level is singly occupied (QD-shell or WL-continuum) and the s-shell is doubly occupied. In this way, the PL-process is sensitive to the high-lying state even though it is not occupied in the initial state [35]. (d) X^{3-} assuming that angular momentum is a good quantum number: the p-shell has angular momentum $L_z = +1$ and -1; the d-shell $+2$, 0 and -2. The X^{3-} ground state changes from a triplet to a singlet at a finite magnetic field. (e) The final state of the singlet X^{3-}. State $|a\rangle$ can couple to the d-shell of the QD via an Auger-like process (state $|b\rangle$) and to a Landau level in the WL (state $|d\rangle$). When d_- and p_+ come into resonance, state $|b\rangle$ couples to state $|c\rangle$ where one electron occupies the p_+-sub-shell.

We present a method to probe the high-lying energy states, for instance, the QD-d-shell and WL-states, without occupying them. The method relies on an imbalance with respect to shell filling in the X^{3-} final state. Following X^{3-} recombination, there are two p-shell electrons yet just one s-shell electron. (Of the two s-shell electrons in the X^{3-} initial state, one recombines with the hole to create a photon.) This imbalance enables Auger-like processes: one of the p-shell electrons falls into the s-shell, thereby losing energy; the other p-shell electron is given exactly this energy and is promoted to a higher-lying state (Fig. 3.3(c)). This process will only occur if a high-lying state exists close to the right energy. If the s–p separation is $\hbar\omega_0$, the process is, therefore, a probe of the energy levels lying $\hbar\omega_0$ above the p-shell. Some spectroscopy is possible: the energy levels of a QD can be tuned with a magnetic field. These processes can result in large changes to the PL on charging from X^{2-} to X^{3-} [35, 76]. For instance, in a QD without a d-shell, on applying a magnetic field, the X^{3-} PL shows a series of pronounced anti-crossings with Landau levels associated with the WL [35]: the WL is thereby probed without occupying it in the initial state.

We explore initially X^{3-} on standard InGaAs QDs. For the singly and doubly charged excitons, X^{1-} and X^{2-}, the emission splits into two lines by the Zeeman effect and blue-shifts via its diamagnetic response (see appendix E). The X^{3-} has a much richer structure (Fig. 3.3(a)). At zero magnetic field, the X^{3-} has a configuration with two electrons in the QD-s-shell and two electrons in the p-shell. According to Hund's rules, the ground state electrons occupy different p-sub-shells with parallel spins (a spin-triplet) and two emission lines result, split by the large electron-electron exchange energy, denoted as t (triplet) and t_s (triplet satellite) in Fig. 3.3(a) [35]. On increasing the magnetic field, the degeneracy (or near degeneracy) of the p-sub-shells is lifted. In the Fock-Darwin model [35, 63, 165], the p_--sub-shell (angular momentum $L_z = +1$) moves down in energy by $-\frac{1}{2}\hbar\omega_c$ while the p_+-sub-shell (angular momentum $L_z = -1$) moves up in energy by $+\frac{1}{2}\hbar\omega_c$ (Fig. 3.3(d)). Here, $\hbar\omega_c$ is the electron cyclotron energy. Once this splitting becomes large enough, the X^{3-} ground state turns from a triplet to a singlet where two electrons of opposite spin populate the lower p-sub-shell (Fig. 3.3(d)) [35]. The transition from triplet to singlet ground state occurs at ~ 1.3 T (Fig. 3.3(a)). The singlet (and not the triplet) ground state represents the probe of the higher lying electronic states.

The magnetic field dependence of the X^{3-} singlet-PL-spectrum on a standard InGaAs QD shows several anti-crossings (Fig. 3.3(a)). We develop a model to describe the X^{3-} final state. The model includes Coulomb interactions within a harmonic confinement and couplings to a WL-continuum (see appendix C). In addition to the energies of the transitions, the linewidths are a powerful diagnostic. The spectrally narrow PL-lines arise from intra-QD-processes; the spectrally broad PL-lines from QD–WL-continuum coupling as the continuum of WL-states facilitates rapid dephasing [35, 151].

The singlet emission at ~ 1.3 T is spectrally broad, which signifies that the final state couples to the WL-continuum. There is an anti-crossing at ~ 3 T with a state with a linear magnetic field dispersion. This anti-crossing indicates a hybridization with the 0th WL-Landau-level (Fig. 3.3(e)). A second singlet emission line appears at higher energy, and there are two further anti-crossings at a high magnetic field (A_1 and A_2 in Fig. 3.3(a)). We exclude that these processes are caused by hybridization with the WL since the optical emission stays narrow in this regime. The first part of the explanation is an Auger-like process within the QD itself (Fig. 3.3(e)). The optical decay of the X^{3-} singlet leaves behind two electrons in the lower p-sub-shell and one electron in the s-shell (state $|a\rangle$). This final state can couple to state $|b\rangle$ via an Auger-like process where one p-electron fills the vacancy in the s-shell and the other goes up into the d-shell. This coherent coupling between the two basis states $|a\rangle$ and $|b\rangle$ leads to two eigenstates after optical decay and thus explains the second emission line at higher energy. The second part of the explanation involves the single-particle states. With increasing magnetic field, the d_--sub-shell of the QD moves down in energy with a dispersion of $-\hbar\omega_c$ while the p_+-sub-shell moves up with $\frac{1}{2}\hbar\omega_c$. In the Fock-Darwin model, angular momentum is a good quantum number and d_- and p_+ therefore cross. Experimentally, this is not the case: there is a small anti-crossing. This is not surprising for a real QD where there is no exact rotational symmetry. To describe this, we introduce basis state $|c\rangle$ (with an electron in the p_+- rather than the d_--shell) and a small coupling between states $|b\rangle$ and $|c\rangle$ to describe the symmetry breaking. This leads to the two characteristic anti-crossings (A_1, A_2) of the singlet emission pair with a line with a dispersion of approximately $-\frac{3}{2}\hbar\omega_c$.

An analytic Hamiltonian describing all these processes is given in appendix C. Using realistic parameters for the QD, the model (Fig. 3.3(a)) reproduces the X^{3-} PL extremely well. This strong agreement allows us to extract the key QD parameters from this experiment: the electron s–p splitting ($\hbar\omega_0 = 24.1$ meV) and the electron effective mass ($0.07m_o$). We are also to conclude that the potential is sub-harmonic: the p–d splitting is smaller than the s–p splitting.

With this understanding of the X^{3-}, we turn to the spectra from an AlAs-capped QD (Fig. 3.3(b)). As for the standard InGaAs QD, there is a transition from triplet to singlet X^{3-} ground state, albeit at higher magnetic fields. In complete contrast to the standard InGaAs QD, the hybridization with a Landau level is not observed. This is powerful evidence that the electron WL-states no longer exist.

The X^{3-} from the AlAs-capped QD is revealing in a number of other respects. First, the X^{3-} singlet state shows one Zeeman-split line, not two as for the standard InGaAs QD. This is evidence that the $|a\rangle - |b\rangle$ coupling is suppressed on account of the energies: state $|b\rangle$ lies at too high an energy to couple to state $|a\rangle$ (see appendix C). A large ratio between $|b\rangle - |a\rangle$ energy splitting and coupling strength leads to a very weak emission from the second line, strongly red-shifted for a positive $|b\rangle - |a\rangle$ energy splitting. The absence of a second singlet emission line is evidence that the p–d splitting is larger than the s–p splitting, a super-harmonic potential. This is consistent with the thin, AlAs-layer in the STEM-characterization (Fig. 3.1(g)) which bolsters the lateral confinement; and also the ensemble-PL where the AlAs-cap blue-shifts the d-shell more than the p-

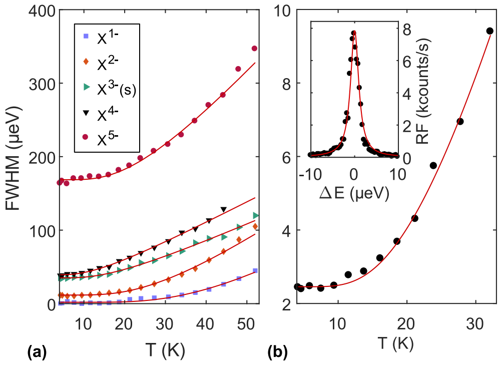

Fig. 3.4: **Linewidths of excitons in an AlAs-capped quantum dot.** (a) Photoluminescence-linewidth (full width at half maximum) of the charged excitons as a function of temperature. The red lines represent a fit to a model that describes the interaction with acoustic phonons. (b) Linewidth of the singly charged exciton X^{1-} in resonance fluorescence as a function of temperature. The inset shows an exemplary resonance fluorescence measurement at 4.2 K with a linewidth of 2.3 μeV. This measurement was carried out at low excitation power (coherent scattering regime). The saturation count rate obtained under resonant excitation is 60 kcounts/s.

shell (Fig. 3.1(i)). Second, the X^{3-} singlet and triplet PL-lines appear simultaneously at low magnetic field (Fig. 3.3(b)) yet there is a rather abrupt transition for the standard InGaAs QD (Fig. 3.3(a)). This is an indication that relaxation to the exciton ground state is slower for the AlAs-capped QDs. This may also be related to the WL: electrons in the WL can mediate spin relaxation. Without the WL, this process is turned off. Finally, the X^{3-} exciton in the AlAs-capped QD has a very pronounced fine structure splitting: the splitting of the X^{3-} triplet into three lines is a prominent feature (Fig. 3.3(b)). This particular fine structure originates from the electron-hole exchange in the initial exciton state [161], and its increase relative to standard InGaAs QDs is indicative of a stronger electron-hole confinement [166, 167].

We model X^{3-} in the AlAs-capped QD with the model developed for the standard InGaAs QD. The coupling to the Landau level is set to zero. A small perturbation is included to account for the anharmonicity of the confinement potential. The model describes the experimental results extremely well (Fig. 3.3(b)). The model determines the electron s–p splitting as $\hbar\omega_0 = 27.5$ meV.

3.5 Temperature Dependence

The temperature dependence of the exciton linewidths is a further probe of the coupling to continuum states. Linewidths of excitons in standard InGaAs QDs strongly increase with temperature as soon as hybridization with a WL is present [151]. Such a temperature broadening was observed for exciton complexes even with modest charge [151], for instance, X^{2-}. For an AlAs-capped QD, we measure the PL-linewidth of all charged excitons (X^{1-} to X^{5-}) as a function of temperature (Fig. 3.4(a)). Even for the highly charged excitons X^{4-} and X^{5-}, the temperature-induced broadening is much weaker than that for charged excitons beyond X^{1-} in standard InGaAs QDs which show a strong, linear temperature dependence [151]. Instead, the linewidths are described well by a model that considers a localized exciton and dephasing via acoustic phonon scattering [168]. This measurement is also evidence that the WL-states for electrons no longer exist.

Finally, we measure the linewidth of the singly charged exciton (X^{1-}) with resonant excitation, detecting the resonance fluorescence [38] (Fig. 3.4(b)). The resonance fluorescence linewidth increases with temperature above ~ 10 K, indicative of acoustic phonon scattering (see appendix D). At 4.2 K, the linewidth (2.3 μeV) is similar to the linewidth of the very best InGaAs QDs [38]. This shows that the AlAs-capped QDs retain the very low charge noise achieved for standard InGaAs QDs [38, 39]. This is important: the AlAs-capped QDs have slow exciton dephasing and weak spectral fluctuations such that they are completely compatible with applications that place stringent requirements on the quality of the single-photons.

Appendix A: Sample Growth, Fabrication, and STEM-measurements

The sample heterostructure is grown by molecular beam epitaxy (MBE) on a GaAs wafer with (001)-orientation. The overall growth conditions are similar to those described in Ref. [40]. The heterostructure, together with growth temperatures and growth rates of individual layers, is given in Table 3.1. To flatten the wafer surface, an AlAs/GaAs-superlattice is grown first. A spacer of 50 nm GaAs separates the superlattice from a silicon-doped (n-type) back-gate (300 nm). QDs are separated from the back-gate by a tunnel barrier of 30 nm GaAs. The QDs (growth described in section 3.2) are overgrown with additional 8 nm of GaAs. To keep the current through the diode structure low, a tunnel barrier (another AlAs/GaAs-superlattice) is grown above the QDs. The heterostructure is completed with a thin GaAs capping layer.

For electric charge control of the QDs, a semi-transparent Schottky top-gate (∼ 6 nm Au) is deposited on part of the sample. An ohmic contact to the back-gate is fabricated by annealing In-solder for 5 min at 370°C in a forming gas atmosphere.

For scanning transmission electron microscopy (STEM) investigations, an electron-transparent lamella was prepared by conventional mechanical polishing followed by argon ion milling. The high-resolution HAADF STEM-image was acquired using a FEI Titan G2 equipped with a Schottky field emission gun operated at 200 kV, a Cs probe corrector (CEOS DCOR). The annular dark-field detector semi-angle used was 69.1 mrad. For STEM, a series of 10 images were recorded with a short acquisition time, aligned and summed using the Velox software (Thermo Scientific) to improve the quality of the image. In the STEM image, the intensity of the atomic columns is approximately proportional to the square of the atomic number [169]. STEM measurements are combined with an energy-dispersive X-ray (EDX) measurement (same microscope). Fig. 3.5 shows a STEM-image of an AlAs-capped QD. The image has an atomic resolution showing that QD and its surroundings are defect-free. For a better visibility, we increase the contrast of the original STEM-image by Gaussian smoothing. The result corresponds to a STEM-image taken with lower spatial resolution and is shown in Fig. 3.5(b). In the STEM-images, a single QD is visible as a bright (In-rich) region. Due to the lower atomic number of aluminum, the AlAs-capping surrounding the QD appears darker. Part of the AlAs/GaAs-superlattice grown above the QDs is visible as an alternating sequence

Material	Thickness (nm)	Temperature (°C)	Rate (Å/s)
GaAs	50	600	2.0
AlAs/GaAs	30×(2/2)	600	1.0/2.0
GaAs	50	600	2.0
n-GaAs	300	600	2.0
GaAs	5	575	2.0
GaAs	25	600	2.0
InAs QDs	–	525	–
AlAs-capping	0.3	525	1.0
GaAs-capping	2	500	2.0
flushing step	–	600	–
GaAs	8	600	2.0
AlAs/GaAs	30×(3/1)	600	1.0/2.0
GaAs	10	600	2.0

Table 3.1: Description of the sample. The different layers of the heterostructure are listed in the order of the growth.

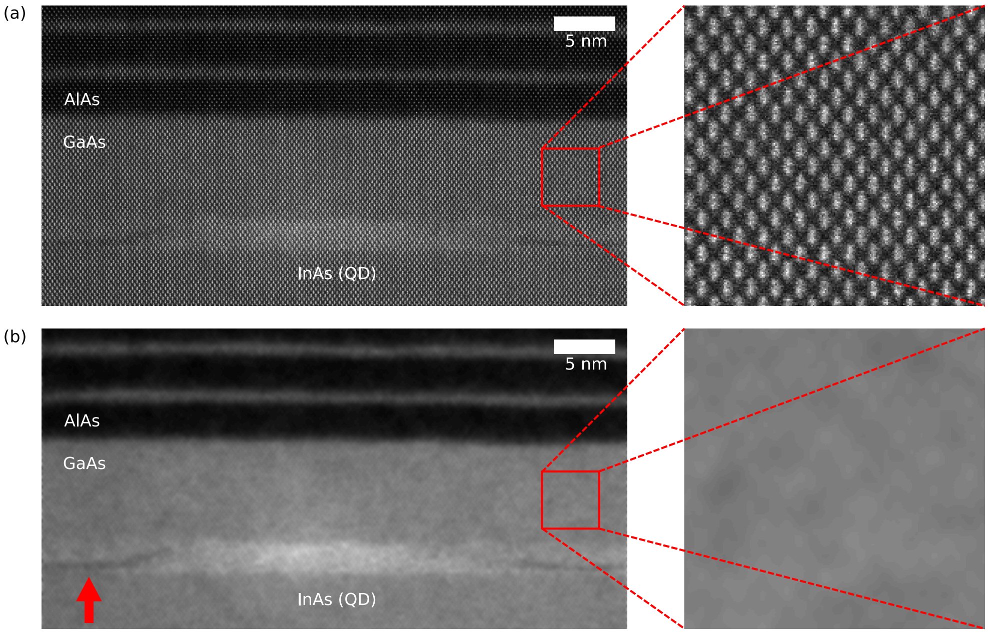

Fig. 3.5: (a) Scanning transmission electron microscopy (STEM) image of an AlAs-capped quantum dot (QD) grown with a flushing step. The STEM-image has an atomic resolution. The QD has a high indium concentration and thus appears bright in the STEM-image. Above the QD, an AlAs/GaAs-superlattice is visible. (b) A Gaussian smoothing of the STEM-image (6 pixel standard deviation) enhances the contrast in the STEM-image. At the edges of the QD, the AlAs capping layer appears as a darker region in the STEM-image (indicated by the red arrow).

of bight and dark regions in the STEM-image.

Appendix B: Wetting-Layer-PL and Indirect Excitons

The nature of the WL-states can also be probed by measuring the emission not from the QDs but from the WL itself. We glean understanding from the standard sample with WL. We then apply this understanding to the sample with AlAs-capped QDs.

Fig. 3.6(a) shows the PL from a sample with standard InGaAs QDs in a large spectral range. QD-emission has a wavelength of about 960 nm; emission related to the WL appears at $\sim$ 875 nm. At a gate voltage above 0.45 V, the WL is charged with electrons from the back-gate. Optical recombination takes place between an electron and a hole, both in the WL. The quantum-confined Stark shift is small because of the strong confinement in the growth direction. At lower gate voltages, the WL-emission strongly

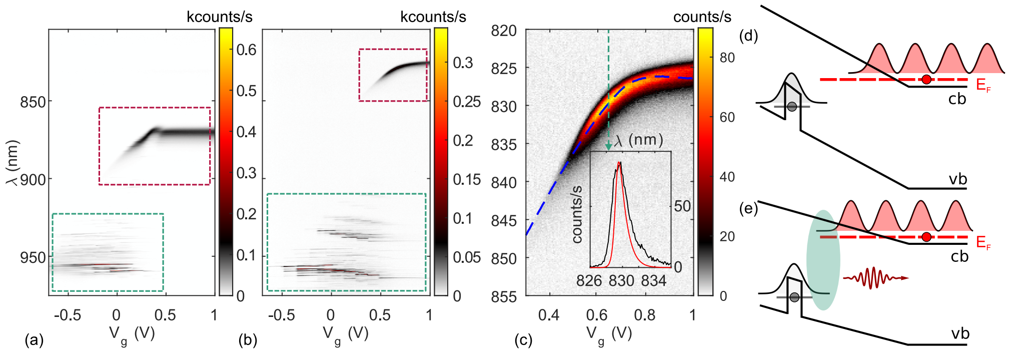

Fig. 3.6: (a) PL over a large bandwidth from the reference sample with standard InGaAs QDs. QD-emission appears at a high wavelength (green frame). PL at ∼ 875 nm is related to the WL (red frame). At low gate voltage, the strong shifts with voltage demonstrate that recombination takes place between holes in the WL and electrons in the back-gate [85]. Above 0.45 V, the strong shift with voltage disappears. This effect demonstrates that there is a transition to a direct emission where recombination takes place between electrons and holes both confined to the WL. The direct recombination is possible since the WL becomes charged with electrons from the back-gate. (b) PL over a large bandwidth from the sample with AlAs-capped QDs. The green frame shows the QD-emission-lines. The PL at ∼ 830 nm arises from spatially indirect recombination between holes in the remnant WL and electrons in the back-gate [85, 86]. (c) A simulation of the indirect emission based on a numerical band structure calculation gives reasonable agreement with the experimental data (dashed blue line). Also, the asymmetric lineshape of the indirect transition (inset: black curve) is reproduced by the simulation (inset: red curve). (d) Explanation of the indirect emission process: at low gate voltage, the built-in electric field of the n-i-Schottky diode suppresses an overlap between back-gate electrons and holes confined in the remnant WL. (e) At positive gate voltage, the electric field is reduced. Consequently, the electron wave functions from the back-gate expand further into the intrinsic region. This leads to a finite wave function overlap between back-gate electrons and WL-holes. The result is an indirect recombination between WL and back-gate. The corresponding emission strongly shifts with the applied gate voltage.

blue-shifts with the electric field. This signals a change in the emission process: it can be explained with spatially indirect recombination between an optically generated hole in the WL and an electron from the back-gate [85, 86].

Fig. 3.6(b) shows PL from the sample with AlAs-capped QDs. The QD-emission has a wavelength of 960 nm, as for QDs in the standard sample. At slightly lower wavelength, emission between higher lying shells of the QD appears. In comparison to the standard InGaAs QDs, this emission is more pronounced for the AlAs-capped QDs. This observation agrees well with the picture of a stronger confinement caused by the AlAs-capping.

Significantly, the emission from a WL-continuum at ~ 875 nm is not observed for the AlAs-capped QDs – confirmation that the electronic WL-states no longer exist. Instead, at high positive gate voltage, there is an emission at ~ 830 nm (Fig. 3.6(c)). The emission arises due to spatially indirect recombination between holes bound by a shallow valence band confinement in the remnant WL and electrons from the back-gate. This process is illustrated in Fig. 3.6(d, e). At small gate voltages, electron wave functions in the back-gate have a negligible overlap with holes bound to the remnant WL. However, at high positive gate voltages, the electric field is reduced. Consequently, there is an overlap between electron wave functions in the back-gate and holes in the remnant WL. This gives rise to the emission at $\lambda \sim 830$ nm. The emission blue-shifts strongly with electric field: this proves its spatially indirect nature.

We simulate the indirect emission line from the AlAs-capped sample in a gate voltage range of $0.3-1.0$ V. For this, we compute the band structure numerically as a function of gate voltage. For the obtained band structure and a given electron energy in the back-gate, we solve the Schrödinger equation numerically assuming an infinitely extended back-gate. As a result, we obtain the wavefunction $\Psi_k(E)$ of a back-gate electron with a specific energy. The intensity of the indirect transition is then estimated as an overlap integral between $\Psi_k(E)$ and the hole wave function Ψ_h which is approximated as a δ-distribution at the WL-position:

$$I\,(E,T) \propto |\langle \Psi_h \mid \Psi_k(E) \rangle|^2 \times \mathrm{DOS}\,(E) \times f\,(E,T)\,. \tag{3.1}$$

The intensity is weighted with a three-dimensional density of states $\mathrm{DOS}\,(E) \propto \sqrt{E - E_{\mathrm{cb}}}$, where E_{cb} is the energy of the conduction band edge, and the Fermi distribution $f\,(E,T)$. The best agreement with the data we find for a Schottky barrier of 0.8 V and a hole ionization energy of 19 meV ($T = 4.2$ K). A slight reduction of the emission energy due to an image charge effect between hole and back-gate has been taken into account. The simulation gives a good description of the line position and the asymmetric line shape of the indirect transition (Fig. 3.6(c)).

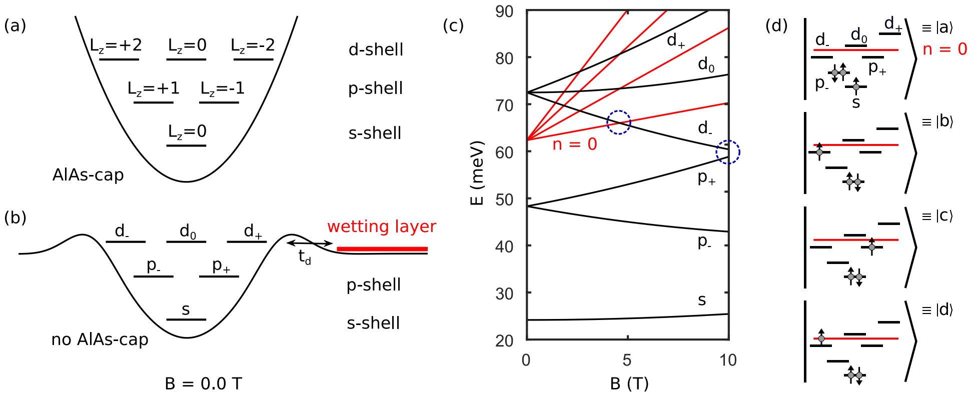

Fig. 3.7: (a) Schematic conduction levels for an AlAs-capped quantum dot (QD). The different shells (s, p, d) are labeled with the corresponding angular momentum quantum number L_z. (b) Schematic conduction levels for a standard QD with a wetting layer (WL). States of the WL-continuum are indicated in red. (c) Black curves: single-particle dispersion for a symmetric two-dimensional harmonic oscillator ($\hbar\omega_0 \approx 24$ meV) as a function of the magnetic field (Fock-Darwin spectrum). Red curves: Dispersion of the WL-Landau-levels. $n = 0$ denotes the lowest Landau level. (d) The four basis states $|a\rangle$, $|b\rangle$, $|c\rangle$, and $|d\rangle$ used to describe the possible final states after X^{3-} recombination. The basis states are shown at high magnetic field.

Appendix C: Modeling of the Magneto-PL-Measurements

We present the calculation which describes the magneto-PL of the X^{3-} exciton complex. The experimental data are shown in Fig. 3.3. The energy of the optical emission lines is given by the energy difference between the initial exciton state before optical recombination and the energy of the electron configuration in the final state after optical recombination. We calculate the energies of the initial and final states separately.

The focus is the X^{3-} singlet exciton. On recombination of an s-shell electron with an s-shell hole, there is a vacancy in the electron s-shell; the p-shell is doubly occupied. This special situation allows Auger-like processes to take place: one of the p-shell electrons falls into the vacancy, the other is promoted to a higher level. These processes admix the QD-d-shell and, should they exist, the WL-Landau-levels into the available final states. The X^{3-} final states have, therefore, a rich structure. As we argue in section 3.4, they provide an ideal way of exploring the single-particle states at energies well above both the s- and p-shells.

Our approach is to focus initially on the behavior of X^{3-} in a QD with a WL. In this case, there is both a confined d-shell and a WL which quantizes into Landau levels in a magnetic field. We develop a model to describe this situation by considering hybridizations between different final states after optical recombination. This allows us to uncover precisely how the X^{3-} spectrum depends on the d-shell and on the WL-Landau-levels: we develop an understanding of our probe of the high-energy states. We then apply this model to a QD in a sample with a modified WL. The absence of features related to the WL enables us to demonstrate that the WL as far as electron states are concerned is no longer present.

3.5.1 The X^{3-} Final States

Assuming that the QD has a lateral parabolic confinement potential of the form $V(r) = \frac{1}{2}m_e^*\omega_0^2 r^2$, the single-particle energies of the different QD shells follow the well known Fock-Darwin spectrum [63, 69, 70]:

$$E_{n,L} = (2n + |L_z| + 1)\,\hbar\omega_1 - \frac{1}{2}L_z\hbar\omega_c. \tag{3.2}$$

Here, n is the radial quantum number and L_z the angular momentum quantum number, $\omega_1 = \sqrt{\omega_0^2 + \left(\frac{\omega_c}{2}\right)^2}$, where $\hbar\omega_c = \hbar eB/m_e^*$ is the electron cyclotron energy, B the magnetic field, and m_e^* the electron effective mass. In Fig. 3.7(c) the magnetic field dispersion described by Eq. 3.2 is shown for different QD shells. The corresponding wave functions are given by [63, 170, 171]

$$|\Psi_{n,L_z}(r,\phi)\rangle = \frac{e^{iL_z\phi}}{\sqrt{\pi}L_e}\sqrt{\frac{n!}{(n+|L_z|)!}}e^{-\frac{r^2}{2L_e^2}}\left(\frac{r^2}{L_e^2}\right)^{|L_z|/2} L_n^{|L_z|}\left(\frac{r^2}{L_e^2}\right). \tag{3.3}$$

The terms $L_n^{|L_z|}$ denote generalised Laguerre polynomials. The parameter $L_e = \sqrt{\hbar/(\omega_1 m_e^*)}$ is the effective length of the wave function.

We consider initially three basis configurations $|a\rangle$, $|b\rangle$, and $|c\rangle$ to describe the final state of the X^{3-} (singlet) exciton. These states and a schematic shell structure of a QD are illustrated in Fig. 3.7. We calculate the energies of states $|a\rangle$, $|b\rangle$, and $|c\rangle$ as the sum of their corresponding single-particle energies and the energies caused by Coulomb interactions between different electrons.

Basis state $|a\rangle$ has one electron in the s-shell and two electrons in the p_--shell (angular momentum $L_z = +1$). According to Eq. 3.2, the sum of all single-particle energies is given by $E_a^0 = 5\hbar\omega_1 - \hbar\omega_c$. State $|b\rangle$ has two electrons in the s-shell and one electron in the d_--shell (angular momentum $L_z = +2$). Its single-particle energy is the same as that of state $|a\rangle$, i.e. $E_b^0 = E_a^0$. State $|c\rangle$ has two electrons in the s-shell and one electron in the p_+-shell (angular momentum $L_z = -1$). Its single-particle energy is given by $E_c^0 = 4\hbar\omega_1 + \frac{1}{2}\hbar\omega_c$. The single-particle energy of state $|c\rangle$ increases in a magnetic field with $+\frac{1}{2}\hbar\omega_c$ whereas that of states $|a\rangle$ and $|b\rangle$ decreases with $-\hbar\omega_c$.

The multi-particle nature of the QD-states gives rise to carrier-carrier Coulomb interactions within the QD, both for the initial exciton state (four electrons and one hole in the QD) and the final states $|a\rangle$, $|b\rangle$, and $|c\rangle$ (three electrons in the QD). We calculate the corresponding energy corrections to the single-particle energies in first order perturbation theory [71, 172]. These energies are the direct carrier-carrier Coulomb interaction given by the relations

$$E_{ij}^d = \frac{e^2}{4\pi\epsilon_0\epsilon_r} \int\int \frac{|\Psi_i(\mathbf{r}_1)|^2 \cdot |\Psi_j(\mathbf{r}_2)|^2}{|\mathbf{r}_1 - \mathbf{r}_2|}\, d\mathbf{r}_1\, d\mathbf{r}_2 \tag{3.4}$$

and the exchange interaction given by

$$E_{ij}^x = \frac{e^2}{4\pi\epsilon_0\epsilon_r} \int\int \frac{\Psi_i(\mathbf{r}_1)^*\, \Psi_j(\mathbf{r}_2)^*\, \Psi_i(\mathbf{r}_2)\, \Psi_j(\mathbf{r}_1)}{|\mathbf{r}_1 - \mathbf{r}_2|}\, d\mathbf{r}_1\, d\mathbf{r}_2. \tag{3.5}$$

For the calculation, we use single-particle wave functions for a symmetric parabolic confinement potential (see Eq. 3.3) and construct fully anti-symmetrized wave functions via Slater determinants. In the case of state $|a\rangle$, for instance, this yields:

$$|a\rangle = \frac{1}{\sqrt{6}} \begin{vmatrix} s_1\uparrow_1 & s_2\uparrow_2 & s_3\uparrow_3 \\ p_1\uparrow_1 & p_2\uparrow_2 & p_3\uparrow_3 \\ p_1\downarrow_1 & p_2\downarrow_2 & p_3\downarrow_3 \end{vmatrix} = \begin{array}{rl} \frac{1}{\sqrt{6}}[& \uparrow_1\uparrow_2\downarrow_3\,(s_1p_2p_3 - p_1s_2p_3) \\ + & \uparrow_1\downarrow_2\uparrow_3\,(p_1p_2s_3 - s_1p_2p_3) \\ + & \downarrow_1\uparrow_2\uparrow_3\,(p_1s_2p_3 - p_1p_2s_3)\,]. \end{array} \tag{3.6}$$

Here, the indices label the different particles, the arrows (↑, ↓) represent the electron spin, and the orbital wave function is represented by the shell label s, p, and d (see Fig. 3.7). For the basis states $|a\rangle$, $|b\rangle$, and $|c\rangle$ the sum of all the direct and the exchange energies is given by:

$$E_a^C = \frac{31}{16}\frac{e^2}{4\pi\epsilon_0\epsilon_r}\frac{1}{L_e}\sqrt{\frac{\pi}{2}}, \tag{3.7}$$

$$E_b^C = \frac{67}{32}\frac{e^2}{4\pi\epsilon_0\epsilon_r}\frac{1}{L_e}\sqrt{\frac{\pi}{2}}, \tag{3.8}$$

$$E_c^C = \frac{9}{4}\frac{e^2}{4\pi\epsilon_0\epsilon_r}\frac{1}{L_e}\sqrt{\frac{\pi}{2}}. \tag{3.9}$$

In these expressions, e is the elementary charge, ϵ_0 the permittivity of vacuum, and ϵ_r the relative permittivity.

We focus now on the couplings between the basis states $|a\rangle$, $|b\rangle$, and $|c\rangle$. As illustrated in Fig. 3.3, states $|a\rangle$ and $|b\rangle$ are coupled by an Auger-like process. For state $|a\rangle$, two electrons occupy the p_--shell (with $L_z = +1$). In the Auger-like process, one of these two electrons goes down to the s-shell (with $L_z = 0$) while the other one goes up to the d_--shell (with $L_z = +2$). This process conserves angular momentum and leads to a coupling between $|a\rangle$ and $|b\rangle$. The corresponding matrix element is given by:

$$A_{ab} = \langle p_1^{L_z=+1} p_2^{L_z=+1} \mid \hat{H}_c \mid s_1^{L_z=0} d_2^{L_z=+2} \rangle = -\frac{5\sqrt{2}}{32} \frac{e^2}{4\pi\epsilon_0\epsilon_r} \frac{1}{L_e} \sqrt{\frac{\pi}{2}}, \tag{3.10}$$

where s, p, and d label the single-particle shell with particle number in the subscript and the angular momentum quantum number in the superscript. $\hat{H}_c$ is the two-particle Coulomb operator given by:

$$\hat{H}_c = \frac{1}{2} \sum_i \sum_{j \neq i} \hat{H}_{ij}, \text{with} \tag{3.11}$$

$$\hat{H}_{ij} = \frac{e^2}{4\pi\epsilon_0\epsilon_r} \frac{1}{|\mathbf{r}_i - \mathbf{r}_j|}, \tag{3.12}$$

where $\mathbf{r}_i$ are the coordinates of the interacting particles.

Fig. 3.8(a) shows a numerical simulation based on the model developed so far: a coupling between $|a\rangle$ and $|b\rangle$; no coupling of states $|a\rangle$ and $|b\rangle$ to state $|c\rangle$. (State $|c\rangle$ is, therefore, irrelevant at this point in the calculation.) Without the $|a\rangle \leftrightarrow |b\rangle$ coupling, there is just a single pair of emission lines. (The splitting within the pair into two lines arises from the spin Zeeman effect.) With the $|a\rangle \leftrightarrow |b\rangle$ coupling, there is no longer just one pair of emission lines but two, Fig. 3.8(a). This feature describes part of the experimental data, Fig. 3.8(d). This demonstrates both that the d-shell exists and that the Auger-like process admixes the d-shell into the X^{3-} final states.

The experimental X^{3-} emission from a standard QD with WL (Fig. 3.8(d)) shows a richer structure than that described with just $|a\rangle \leftrightarrow |b\rangle$ coupling (Fig. 3.8(a)). In the experiment, there are several anti-crossings at high magnetic field along with a complex structure at low magnetic field. This leads us to the conclusion that additional couplings must be introduced to describe the experimental results.

First, we consider the coupling between states $|b\rangle$ and $|c\rangle$. For a perfectly symmetric harmonic confinement potential, this coupling is zero since states $|b\rangle$ and $|c\rangle$ have different angular momenta. Nevertheless, the experiment points to a coupling in the present case. This coupling represents a slight asymmetry in the confinement potential of the QD since, in this case, angular momentum is not a good quantum number [171]. In our

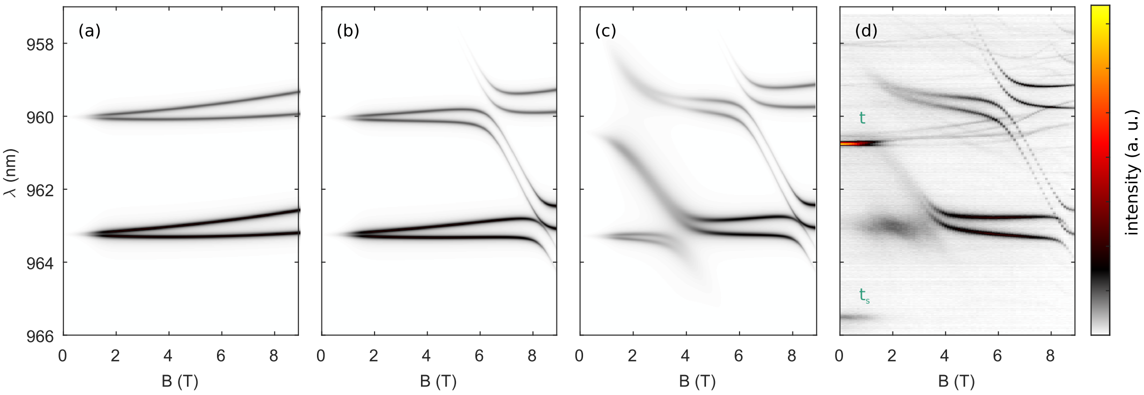

Fig. 3.8: Description of X^{3-} in a quantum dot (QD) with wetting layer (WL). (a) Simulation of the X^{3-} emission spectrum without the coupling term Δ_{bc} between states $|b\rangle$ and $|c\rangle$ and without couplings between QD- and WL-states (A_L, t_d). (b) Simulation including the coupling term Δ_{bc}, yet without the couplings between QD- and WL-states. (c) Final simulation of the X^{3-} emission spectrum including all coupling terms. (d) Measured X^{3-} emission spectrum as a function of the magnetic field. The simulation shown in (a-c) focuses on the X^{3-} singlet, emission of the X^{3-} triplet at low magnetic field (t, t_s) is not included.

simulations we assume a constant coupling term Δ_{bc} between the states $|b\rangle$ and $|c\rangle$. A numerical simulation taking the coupling Δ_{bc} into account is shown in Fig. 3.8(b). The coupling accounts for the pronounced anti-crossings (A_1, A_2 in Fig. 3.3) in the X^{3-} emission lines at high magnetic field.

We note that we neglect any direct coupling between states $|a\rangle$ and $|c\rangle$. At low magnetic field, $|c\rangle$ is energetically far away from $|a\rangle$. At high magnetic field, when $|c\rangle$ comes energetically close to the states $|a\rangle$ and $|b\rangle$, a coupling between $|a\rangle$ and $|c\rangle$ would be both a two particle and angular momentum non-conserving process. On this basis, we assume that a $|a\rangle \leftrightarrow |c\rangle$ coupling is much weaker than the $|b\rangle \leftrightarrow |c\rangle$ coupling. (The $|b\rangle \leftrightarrow |c\rangle$ coupling is a single-particle process and is important when the energies of the d_--shell and the p_+-shell come into resonance, Fig. 3.3(e) and Fig. 3.7(c).) Of course, via the $|a\rangle \leftrightarrow |b\rangle$ and $|b\rangle \leftrightarrow |c\rangle$ couplings, states $|a\rangle$ and $|c\rangle$ will anti-cross.

The $|b\rangle \leftrightarrow |c\rangle$ coupling does not account for the behavior at magnetic fields of $1-4$ T as revealed by a comparison of the calculation (Fig. 3.8(b)) with the experiment (Fig. 3.8(d)). We cannot account for this behavior within the $|a\rangle$, $|b\rangle$, $|c\rangle$ basis. The experiment shows features with a strong negative energy dispersion with increasing magnetic field. These are suggestive of Landau levels in the final state [35]. Landau levels are features of a quantized two-dimensional continuum: they are associated with the WL.

Next, we consider the coupling between WL-Landau-levels and the QD. An Auger-like coupling between state $|a\rangle$ and WL-Landau-level [35] is illustrated in Fig. 3.3(e). The Landau levels of the two-dimensional WL have a dispersion given by $\hbar\omega_c(n+\frac{1}{2})$ [173], with $n \in \mathbb{N}_0$ the Landau level number and $\hbar\omega_c$ the electron cyclotron energy as before. Thus, state $|d\rangle$, the three electron state with two electrons in the s-shell and one electron in a Landau level (see Fig. 3.3(e)), has a magnetic field dispersion given by:

$$E_d = E_d^0 + \hbar\omega_c\left(n+\frac{1}{2}\right). \tag{3.13}$$

The term E_d^0 includes both single-particle energies and Coulomb interaction energies in state $|d\rangle$. The dispersion of E_d is dominated by the Landau level dispersion and E_d^0 is assumed to be constant. Basis states $|a\rangle$, $|d\rangle$ are coupled by an Auger-like process: an anti-crossing with a particular Landau level appears at the magnetic field at which the energy difference between Landau level and QD-p_--shell equals that between p_-- and s-shell of the QD. (For a harmonic confinement potential in a single-particle description, this corresponds to the crossing point of the Landau level and the d_--shell of the QD.) At this point, the corresponding Auger-like process is energy conserving and state $|a\rangle$ couples to the corresponding Landau level. The matrix element for the coupling to the 0th Landau level has been calculated in Ref. [35]. Higher Landau levels also have a d-like component and thus couple to state $|a\rangle$ as well [35]. This gives rise to a series of anti-crossings in the emission spectrum of the X^{3-} singlet state [35, 76]. Since the magnetic field regime in which state $|a\rangle$ couples to Landau levels is relatively narrow, we take here just the coupling to the $n=0$ Landau level, and we assume that the $|a\rangle \leftrightarrow |d\rangle$ coupling, parameter A_L, to be constant with magnetic field [35]. Finally, we introduce a tunnel coupling t_L between the d_--shell and the 0th Landau level of the WL [84]. This couples basis states $|b\rangle$ and $|d\rangle$ with a matrix element t_d (see Fig. 3.7(b)). Including t_d turned out to be necessary to obtain a good description of the measurement, in particular, the X^{3-} singlet emission at ~ 4 T.

In this model, the Auger-like coupling between $|a\rangle$ and $|b\rangle$ is calculated based on the assumption of a perfect harmonic confinement potential. However, for carriers in higher shells of the QD this assumption is not necessarily a good one. Especially in the case of a standard InGaAs QD with WL-states, the potential “softens” (becomes sub-harmonic) such that the energies of the higher shells are reduced with respect to the harmonic oscillator (see Fig. 3.7(b) for an illustration). To compensate for such an effect, we correct both energy and Auger-like coupling of state $|b\rangle$, the only basis state with a QD-d-shell component. In particular, we add a constant energy term to the energy of state $|b\rangle$ ($E_b^0 + E_b^C \rightarrow E_b^0 + E_b^C + \delta E_b$) and scale the coupling between states $|a\rangle$ and $|b\rangle$ with a constant pre-factor ($A_{ab} \rightarrow s_{ab} \cdot A_{ab}$).

The full Hamiltonian describing the final states in the $|a\rangle$, $|b\rangle$, $|c\rangle$, $|d\rangle$ basis becomes:

$$\hat{H}_f = \begin{bmatrix} E_a^0 + E_a^C & s_{ab} \cdot A_{ab} & 0 & -A_L \\ s_{ab} \cdot A_{ab} & E_b^0 + E_b^C + \delta E_b & \Delta_{bc} & t_d \\ 0 & \Delta_{bc} & E_c^0 + E_c^C & 0 \\ -A_L & t_d & 0 & E_d \end{bmatrix} \tag{3.14}$$

To obtain the energies of all final states after optical emission we diagonalize this Hamiltonian numerically for all different magnetic fields. To calculate the actual energies of the optical emission, the eigenenergies are subtracted from the energy of the initial exciton state, i.e. the energy of the X^{3-} before radiative recombination. The initial exciton state is depicted in Fig. 3.3(c). It couples optically only to the final state $|a\rangle$. The relative brightness of one particular optical emission line is given by the fraction of state $|a\rangle$ in the particular eigenstate of $\hat{H}_f$.

A numerical simulation taking also the couplings A_L and t_L to the 0th WL-Landau-level into account is shown in Fig. 3.8(c). We achieve an excellent agreement with the experiment, Fig. 3.8(d). The model accounts for all the main features in the experiment, both the energies of the multiple emission lines and their relative intensities. This gives us confidence that the model accounts for all the significant interactions in the X^{3-} final state in the most complicated case, an InGaAs QD with associated WL.

3.5.2 The X^{3-} Initial States

After X^{3-} recombination, there is a vacancy in the s-shell, allowing Auger-like processes to take place. These processes admix the QD-d-shell and the WL-Landau-levels into the final states. The X^{3-} final states have a rich structure. In contrast, the X^{3-} initial states have a much simpler structure.

At high magnetic field, the X^{3-} initial state has two electrons in the conduction band s-shell and two electrons in the p_--shell of the QD along with a hole in the valence band s-shell. For the electrons, this represents a spin singlet. Other configurations have considerably larger single-particle energies and are, therefore, ignored. The energy of this exciton is given by an effective band gap of the QD E_g^* plus the sum of electron and hole single-particle energies and Coulomb interaction terms:

$$E_i = E_g^* + E_i^0 + E_i^{ee} + E_i^{eh}. \tag{3.15}$$

Here the term E_i^0 denotes the single-particle energy of electrons and hole, E_i^{ee} is the sum of the Coulomb interactions between the electrons, and E_i^{eh} is the Coulomb interaction between electrons and hole. The hole wave function and its single-particle energy can be obtained by using Eqs. 3.2 and 3.3, replacing the electron effective mass with the hole effective mass m_h^*. For the single-particle energy of electrons and hole in the X^{3-} singlet state we obtain:

$$E_i^0 = 6\hbar\omega_1 - \hbar\omega_c + \hbar\omega_1^h, \text{ with} \tag{3.16}$$

$$\omega_1^h = \sqrt{\left(\omega_0^h\right)^2 + \left(\frac{\omega_c^h}{2}\right)^2}, \tag{3.17}$$

where $\hbar\omega_c^h = \hbar eB/m_h^*$ is the cyclotron energy of the hole. We make here the assumption that the QD-confinement-potential experienced by the hole equals that experienced by the electrons. This leads to the relation $m_h^* \left(\omega_0^h\right)^2 = m_e^* \left(\omega_0\right)^2$ and determines implicitly the parameter ω_0^h. For the electron-electron and electron-hole Coulomb energies we obtain [71]:

$$E_i^{ee} = \frac{67}{16}\frac{e^2}{4\pi\epsilon_0\epsilon_r}\frac{1}{L_e}\sqrt{\frac{\pi}{2}}, \tag{3.18}$$

$$E_i^{eh} = -2\frac{e^2\sqrt{\pi}}{4\pi\epsilon_0\epsilon_r}\left(\frac{1}{\sqrt{L_e^2 + L_h^2}} + \frac{2L_e^2 + L_h^2}{2\left(L_e^2 + L_h^2\right)^{3/2}}\right). \tag{3.19}$$

Note that the magnetic field dependence of the electron and hole effective lengths, $L_e = \sqrt{\hbar/(\omega_1 m_e^*)}$ and $L_h = \sqrt{\hbar/(\omega_1^h m_h^*)}$, causes a magnetic field dependence of the electron-electron and electron-hole Coulomb matrix elements, leading in turn to a magnetic field dependence of the emission energies beyond the diamagnetic shift in a single-particle picture. In our simulations, this effect is taken into account.

There are two final points. First, there is a clear Zeeman effect in the experimental data (Fig. 3.8(d)). The Zeeman energy $E_Z = g_X \mu_B B$, where $g_X = g_e + g_h$ is the exciton g-factor, is included after computing the eigenstates of Eq. 3.14. The Zeeman effect splits every emission line into two; the energy separation of the lines is the Zeeman energy. This holds for negligible spin-orbit interaction such that spin and orbital degrees of freedom can be considered separately. Secondly, at low magnetic fields, the X^{3-} initial state is an electronic triplet state: the *s*-shell is doubly occupied, the p_+-shell is singly occupied, and the p_--shell is singly occupied. This triplet initial state results in two PL-lines [35, 79]. The triplet state is a less sensitive probe to higher lying single-particle

parameter	standard InGaAs QD	AlAs-capped QD
$\hbar\omega_0$ (meV)	24.163	27.524
$\hbar\omega_0^h$ (meV)	9.125	10.653
m_e^*/m_o	0.0727	0.0750
m_h^*/m_o	1.0	0.501
s_{ab}	0.443	0.921
$s_{ab} \cdot A_{ab}$ (meV)	-2.038	-4.677
E_g^*(eV)	1.3102	1.2993
Δ_{bc} (meV)	0.774	1.033
t_d (meV)	1.549	–
A_L (meV)	0.383	–
E_d^0 (meV)	154.2	–
δE_b (meV)	-4.639	10.372
ϵ_r	13.16	12.93
g_X	1.52	1.60

Table 3.2: Parameters for the simulation of the X^{3-} singlet emission lines. Simulation and data for a standard InGaAs and an AlAs-capped QD are shown in Fig. 3.8 and Fig. 3.3(a),(b). Parameter values are stated with high precision to facilitate reproducing the simulations.

states: it does not show a hybridization with the d-shell or with WL-Landau-levels [35]. However, at small magnetic fields, around ~ 1.3 T, the singlet initial state becomes the ground state, not the triplet state. As such, we have focussed the entire calculation on the X^{3-} singlet initial state. The X^{3-} triplet initial state is included in the simulations phenomenologically with a parabolic dispersion.

3.5.3 Parameters

The parameters for the simulations shown in Fig. 3.8 and Fig. 3.3(a),(b) are given in Table 3.2. For both the standard InGaAs QD and the AlAs-capped QD, the model parameters were tuned to give a quantitative description of the experimental results.

For the AlAs-capped QDs, there is no evidence whatsoever in the PL-spectra for the process related to the hybridization with the WL. This is evidence that the WL for electrons no longer exists. Therefore, the terms A_L and t_d are set to zero in the simulation.

For the standard InGaAs QD, the intra-dot Auger-like process (i.e. the $|a\rangle \leftrightarrow |b\rangle$ coupling) results in two pairs of emission lines. For the AlAs-capped QD, only a single emission pair is observed. This is evidence that the d-shell of the QD is increased in energy with respect to harmonic confinement. For the simulation, we add a positive correction to the d-shell energy: $\delta E_b \sim +10$ meV. Neglecting Coulomb interactions, this leads to a splitting of δE_b between states $|a\rangle$ and $|b\rangle$. In the X^{3-} final states, the second pair of emission lines is red-shifted by $\sim \delta E_b + 2 \cdot s_{ab} \cdot |A_{ab}| \sim 20$ meV. Furthermore, since $\delta E_b > s_{ab} \cdot |A_{ab}|$, the admixture of basis state $|a\rangle$ in the final state corresponding to the "second" emission pair is strongly reduced: the intensity of the second emission lines becomes very weak.

Additional evidence that the QD-potential "hardens" (becomes super-harmonic) on capping with AlAs comes from ensemble PL-measurements which show a larger p–d splitting compared to the standard InGaAs QDs (Fig. 3.1(i)). Microscopically, this behavior must result from the AlAs which surrounds the QD laterally.

For InGaAs QDs with a WL, δE_b is negative. This is consistent with the concept that the presence of a WL "softens" the confinement potential at higher energies. However, in comparison to the confinement energy $\hbar\omega_0$, the term δE_b is small. In other words, for these standard QDs, the approximation of harmonic confinement is still a reasonable one.

The parameters for the electron and hole confinement energies ($\hbar\omega_0$ and $\hbar\omega_0^h$) are comparable to literature values [174, 175]. The term $\hbar\omega_0$ is larger for the AlAs-capped QD. This is consistent with the understanding that the AlAs-capping increases the lateral carrier-confinement of the QD.

The values for the electron effective mass are similar to the bulk effective mass of GaAs [176] in both cases. In contrast, the hole effective masses are larger than the bulk value. For the calculation shown here, the in-plane effective mass has to be considered. Besides, the effective mass is influenced by the strong confinement of the QD [177]. Nevertheless, the hole mass is rather large. This may reflect the fact that the relation $m_h^* \left(\omega_0^h\right)^2 = m_e^* \left(\omega_0\right)^2$ is inaccurate. There is insufficient information in the spectra to determine m_h^* and ω_0^h independently.

Values obtained for the dielectric constant ϵ_r are in both cases between the bulk value of GaAs and InAs ($\epsilon_{\mathrm{GaAs}} = 12.5$ [178, 179], $\epsilon_{\mathrm{InAs}} = 15.2$ [179]).

3.5.4 Coulomb Matrix Elements for Two-Dimensional Harmonic Oscillator Wavefunctions

In the previous sections, the direct Coulomb interaction and the exchange interaction between particles are calculated. In this section, we give a brief description of how these energies can be calculated analytically.

Matrix elements are calculated by inserting the single-particle wave functions (see Eq.

3.3) into Eqs. 3.4 and 3.5. One obtains a sum of integrals which have the form:

$$\iiiint_{-\infty}^{\infty} \frac{e^{-\frac{\alpha}{2}\left(x_1^2+y_1^2+x_2^2+y_2^2\right)}}{\sqrt{(x_1-x_2)^2+(y_1-y_2)^2}} x_1^{n_1} y_1^{n_2} x_2^{n_3} y_2^{n_4} \; dx_1 \; dy_1 \; dx_1 \; dy_2 \tag{3.20}$$

After a coordinate transformation into center of mass coordinates,

$$X = \frac{1}{2}\left(x_1+x_2\right), Y = \frac{1}{2}\left(y_1+y_2\right), x = \frac{1}{2}\left(x_1-x_2\right), y = \frac{1}{2}\left(y_1-y_2\right), \tag{3.21}$$

an analytical solution for the matrix elements can be obtained by using the integral relation (for even n, m, N, M):

$$\begin{aligned}
&\iiiint_{-\infty}^{\infty} \frac{e^{-\alpha\left(x^2+X^2+y^2+Y^2\right)}}{\sqrt{x^2+y^2}} x^n y^m X^N Y^M \; dx \; dy \; dX \; dY \\
=&\left(\frac{1}{\sqrt{\alpha}}\right)^{N+M+2} \Gamma\left(\frac{N+1}{2}\right) \Gamma\left(\frac{M+1}{2}\right) \int_0^{2\pi} \int_0^{\infty} e^{-\alpha r^2} r^{n+m} \sin^n\left(\phi\right) \cos^m\left(\phi\right) \; dr \; d\phi \\
=&\frac{1}{2}\left(\frac{1}{\sqrt{\alpha}}\right)^{N+M+n+m+3} \Gamma\left(\frac{N+1}{2}\right) \Gamma\left(\frac{M+1}{2}\right) \Gamma\left(\frac{n+m+1}{2}\right) \int_0^{2\pi} \sin^n\left(\phi\right) \cos^m\left(\phi\right) \; d\phi.
\end{aligned} \tag{3.22}$$

Here, we used a transformation into polar coordinates and the following relation:

$$\int_0^{\infty} e^{-\alpha x^2} x^n dx = \frac{1}{2}\left(\frac{1}{\sqrt{\alpha}}\right)^{n+1} \cdot \Gamma\left(\frac{n+1}{2}\right). \tag{3.23}$$

For arbitrary wave functions of a two-dimensional harmonic oscillator, a completely general analytical solution for the Coulomb matrix elements is given in Refs. [180, 181], in agreement with values for specific matrix elements obtained by calculating the integrals one-by-one [71].

Appendix D: Temperature Dependent Measurements

Temperature dependent linewidth measurements in photoluminescence (PL) and resonance fluorescence are shown in Fig. 3.4(a),(b). The linewidths (full width at half maximum, FWHM) as a function of temperature are fitted to the model:

$$\text{FWHM}(T) = \text{FWHM}(T=0) + a \cdot \left[\coth\left(\frac{\hbar\omega_q}{k_\text{B}T}\right) - 1\right]. \tag{3.24}$$

	X^{1-}	X^{1-} (RF)	X^{2-}	X^{3-}	X^{4-}	X^{5-}
FWHM($T = 0$) (μeV)	<10	2.46	11.7	35.1	39.3	169
a (μeV)	268	29.6	182	60.1	52.3	226
$\hbar\omega_q$ (meV)	5.94	3.14	3.78	2.10	1.55	3.01

Table 3.3: Parameters obtained by fitting Eq. 3.24 to the temperature dependent photoluminescence/resonance fluorescence. Data and fits are shown in Fig. 3.4(a).

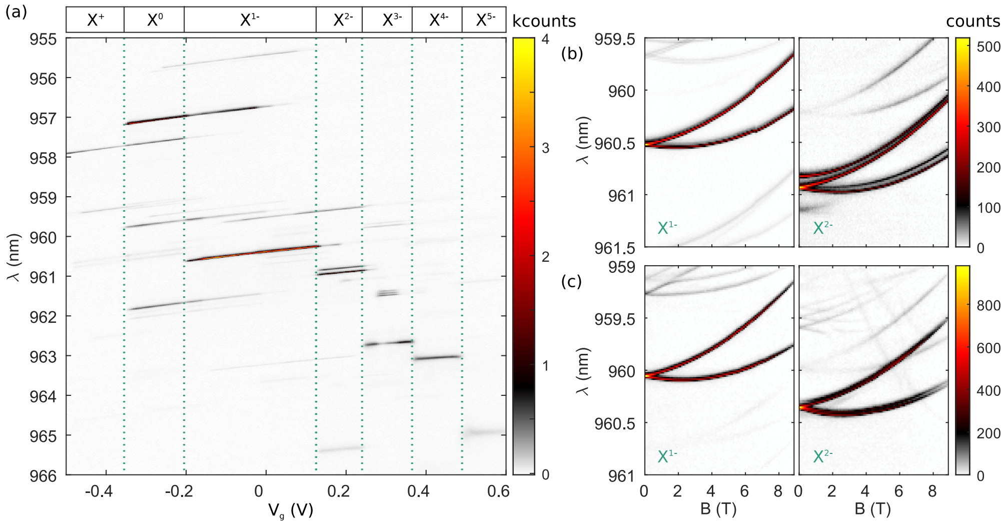

Fig. 3.9: (a) Photoluminescence as a function of gate voltage for an AlAs-capped QD without WL-states for electrons. Exciton complexes ranging from X^+ to X^{5-} are observed. (b) Emission of an AlAs-capped QD as a function of the magnetic field (X^{1-} and X^{2-}). (c) As for (b) but from a standard InGaAs QD.

This is the model from Ref. [168] plus a constant. This temperature dependence describes the linewidth broadening of the zero-phonon-line by the interaction with a single acoustic phonon mode. The fit parameters for the PL-measurements are shown in Table 3.3.

Appendix E: All Charge States of a Single Quantum Dot

In Fig. 3.2, emission of a QD without WL-states for electrons is compared to a standard InGaAs QD with a focus on charged excitons. In Fig. 3.9(a) we show photoluminescence over a larger gate voltage range (same QD as shown in Fig. 3.2(c)). The measurement shows exciton complexes ranging from a positively charged exciton (X^+) to a five-fold negatively charged exciton (X^{5-}). As pointed out in section 3.3, we find optically narrow emission for the excitons X^{3-}, X^{4-}, and X^{5-} which is in strong contrast to standard InGaAs QDs with WL-states for electrons [79, 151].

Shown in Fig. 3.9(b) is the photoluminescence of the X^{1-} and the X^{2-} excitons as a function of the magnetic field on the same AlAs-capped QD. Both emission lines show a Zeeman splitting and a diamagnetic shift. An equivalent measurement on a standard InGaAs QD is shown in Fig. 3.9(c) for comparison. The diamagnetic shift and Zeeman splitting are similar for both types of QDs. The X^{2-} emission shows a larger fine structure in the case of the AlAs-capped QD (similar to the X^{3-} triplet emission shown in Fig. 3.2(c)) implying that the electron-hole exchange in the initial exciton state is larger for the AlAs-capped QDs [161].

Chapter 4

Correlations between Optical Properties and Voronoi-Cell Area

This section is partly adapted from Ref. [77]: "Correlations between Optical Properties and Voronoi-Cell Area of Quantum Dots", Matthias C. Löbl, Liang Zhai, Jan-Philipp Jahn, Julian Ritzmann, Yongheng Huo, Andreas D. Wieck, Oliver G. Schmidt, Arne Ludwig, Armando Rastelli, and Richard J. Warburton, Phys. Rev. B **100**, 155402 (2019).

Abstract: A semiconductor quantum dot (QD) can generate highly indistinguishable single-photons at a high rate. For application in quantum communication and integration in hybrid systems, control of the QD optical properties is essential. Therefore, understanding the connection between the optical properties of a QD and the growth process is important. Here, we show for GaAs QDs, grown by infilling droplet-etched nano-holes, that the emission wavelength, the neutral-to-charged exciton splitting, and the diamagnetic shift are strongly correlated with the capture zone-area, an important concept from nucleation theory. We show that the capture-zone model applies to the growth of this system even in the limit of a low QD-density in which atoms diffuse over μm-distances. The strong correlations between the various QD parameters facilitate a preselection of QDs for applications with specific requirements on the QD properties; they also suggest that a spectrally narrowed QD distribution will result if QD growth on a regular lattice can be achieved.

4.1 Introduction

Semiconductor quantum dots (QDs) are excellent as a bright source of highly indistinguishable single photons [13, 14, 19, 20, 21, 22, 182, 183] and entangled photon pairs [184, 185, 186, 187, 188, 189, 190, 191]. A QD can host a single spin [15, 31, 91, 120] which, however, has a too short coherence time for applications in quantum communication [17, 27, 33, 34]. A hybrid-system of a QD and an atomic quantum memory is more promising in that respect [192, 193]. To connect a QD to an atomic memory based on rubidium, the QD should emit photons matched both in emission energy and bandwidth to the memory [59]. The emission energy can be matched by using GaAs QDs embedded in AlGaAs [88, 194]; bandwidth matching can be achieved by using a Raman-scheme [195, 196, 197, 198].

The growth of QDs has been intensively studied employing scanning probe microscopy [199, 200, 201, 202, 203, 204, 205, 206, 207]. Aiming at entangled photon-pair generation, a connection between such an analysis and the optical properties [208, 209, 210] has focused mostly on the fine-structure splitting of the QD-emission [211, 212, 213, 214, 215, 216, 217, 218]. To tailor all the optical QD-properties, it is important to understand how they are connected to the QD-growth [201].

Here, we establish a strong correlation between the optical properties of GaAs QDs, such as emission energy and diamagnetic shift, and a basic concept from nucleation theory, the capture-zone [206, 219, 220]. This correlation is not obvious since the applicability of the capture zone model depends on conditions such as sudden nucleation [221] and spatially uniform diffusion [222]. Both are not necessarily fulfilled. The correlations that we find here are absent for InGaAs QDs [223] and locally very weak for SiGe QDs [206, 222]. The system we investigate consists of GaAs QDs grown by infilling of Al-droplet-etched nano-holes in an AlGaAs surface [66, 211].

We apply the capture-zone model to the first phase of this process, the formation and growth of Al-droplets. The capture-zone model implies a correlation between Al-droplet volume (island size [206, 224]) and capture-zone area. We show experimentally that this results in a strong correlation between the capture zone area and the optical QD-properties.

We use spatially-resolved photoluminescence imaging to determine the position and the optical properties of individual QDs simultaneously. We investigate samples of low QD-density where a QD is small relative to the distances between QDs (point-island model [220]). The capture zone of each QD is determined as its Voronoi-cell (VC) [206, 219, 221, 222]. From the distribution of the VC-areas, we estimate a critical nucleus size of the Al-droplets (see section 4.5). We find a strong negative correlation between the VC-area, A_{VC}, of a QD and its emission energy, in turn, a strong positive correlation between A_{VC} and the diamagnetic shift of the emission. These results can be well explained with the capture-zone model describing the aggregation dynamics of the Al-droplets. Correlations are measured for QDs of particularly low density, $n_{\mathrm{QD}} < 1\ \mu\mathrm{m}^{-2}$, implying a diffusion length on the μm-scale during the growth phase of Al-droplets [207]. This is a striking result: The optical properties of a QD, which are directly related to its structure on an nm-scale, are strongly correlated with its surroundings on a μm-scale.

4.2 Sample Growth

The samples are grown by molecular-beam epitaxy (MBE) on a (001)-substrate. We investigate two different samples (denoted here as A and B) that are grown in two different MBE-chambers. QDs are grown by GaAs-infilling of Al-droplet-etched nano-holes. A schematic depiction of the growth is shown in Fig. 4.1. First, aluminum is deposited on an AlGaAs-surface in the absence of an As-flux. The growth parameters are: 0.5 ML on $\mathrm{Al_{0.4}Ga_{0.6}As}$, $T = 600°\mathrm{C}$, flux $F = 0.5$ ML/s for sample A; and 0.16 ML on $\mathrm{Al_{0.33}Ga_{0.67}As}$, $T = 630°\mathrm{C}$, flux $F = 0.18$ ML/s for sample B. For both samples, the layer thicknesses correspond to an equivalent amount of AlAs. The Al-atoms nucleate (Volmer-Weber mode [225]) in the form of liquid nano-droplets on the sample surface (see Fig. 4.1(a)).

Underneath an Al-droplet the substrate material is unstable leading to a nano-etching process (Fig. 4.1(b)) [66]. Under a low As-flux, the etching proceeds until the whole Al-droplet is consumed and the material is recrystallized in the surrounding region. Another 2 nm of GaAs is grown on top, filling up the nano-holes via diffusion during a 2-minute annealing step (Fig. 4.1(c)). Overgrown with AlGaAs, the filled nano-holes become optically active QDs (Fig. 4.1(d)).

4.3 Optical Measurements

Optical measurements are performed in a helium bath-cryostat. Photoluminescence (PL) is measured under above-band excitation ($\lambda = 633$ nm). An aspheric objective lens (NA = 0.68) collects the PL. The PL of the QD-ensemble is centered at wavelength 787.4 nm for sample A, 798.0 nm for sample B (values referring to the neutral exciton, X^0), with ensemble standard-deviations 3.4 nm and 1.4 nm, respectively. A typical spectrum of a single QD is shown in Fig. 4.2(a). The neutral exciton has the highest emission energy [88]; the positively charged exciton is redshifted by on average 2.7 meV (sample B: 2.1 meV). Additional exciton complexes appear at even lower energy [226] but are not the focus of our analysis.

Spatially resolved micro-PL is performed by scanning the sample with a low-temperature piezoelectric xy-scanner (attocube ANSxy100/lr). A spatially resolved PL-measurement

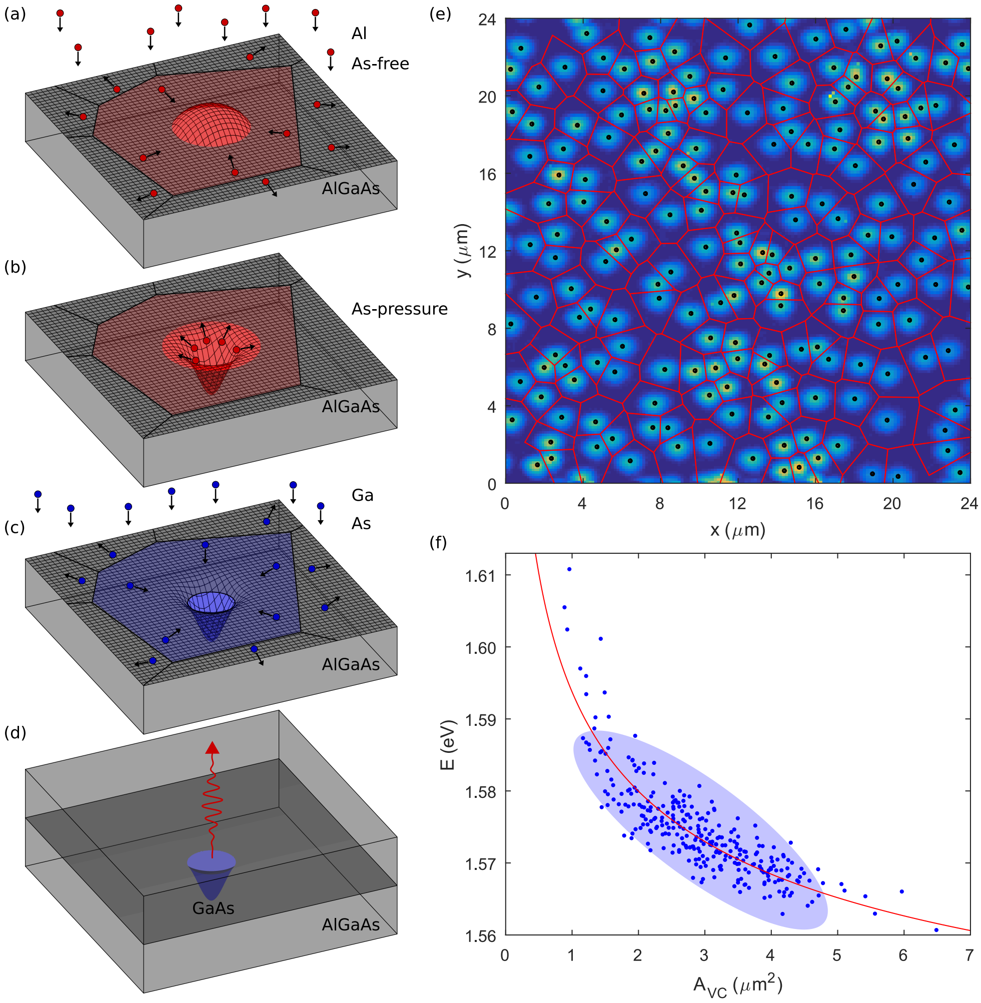

Fig. 4.1: (a) Schematic of the growth process of the quantum dots (QDs). In a first step, aluminum is deposited on an epitaxially grown AlGaAs surface. The aluminum atoms nucleate in the form of liquid nano-droplets. An atom is most likely to attach to the closest Al-droplet. This is the Al-droplet into whose capture zone (red area) the atom falls. (b) Underneath the Al-droplet, the substrate material is unstable. Nano-hole etching takes place upon exposure to an arsenic flux. (c) After the formation of nano-holes, GaAs is deposited. Diffusion leads to an infilling of the droplet-etched nano-holes with GaAs. (d) Finally, the sample is capped with AlGaAs. The GaAs within the nano-hole is now embedded in higher bandgap AlGaAs and forms a QD. (e) Spatially resolved photoluminescence (PL) on a 24 × 24 μm^2-large region of sample A. Positions of individual QDs are obtained by Gaussian fitting (black dots). The red lines are the Voronoi-cells (VCs) corresponding to the QD-positions. (f) Relation between the VC-area (A_{VC}) and the emission energy of the neutral exciton, X^0. The light-blue ellipse is a guide to the eye indicating the correlation in a linear approximation (correlation coefficient $\rho = -0.812$). The red line is a fit of Eq. 4.1.

is shown in Fig. 4.1(e). QDs can be identified as bright regions on this PL-map. The lateral positions of the QDs are obtained by fitting two-dimensional Gaussians. A slight non-linearity of the piezo-scanner is corrected by using the widths of the fitted Gaussians as a reference (see section 4.6). We determine the capture zone around a QD by its Voronoi-cell (VC) – the area that is closer to this particular QD than to any other one. A Voronoi-diagram is shown in Fig. 4.1(e) together with the corresponding QD-positions. We find an average VC-area of $\langle A_{\mathrm{VC}} \rangle = 3.04 \pm 0.08\ \mu\mathrm{m}^2$ (sample A) and $\langle A_{\mathrm{VC}} \rangle = 6.87 \pm 0.44\ \mu\mathrm{m}^2$ (sample B), corresponding to a quantum dot density of $n_{\mathrm{QD}} = 0.329 \pm 0.009\ \mu\mathrm{m}^{-2}$ and $n_{\mathrm{QD}} = 0.146 \pm 0.009\ \mu\mathrm{m}^{-2}$, respectively.

Shown in Fig. 4.1(f) is the emission energy of the neutral exciton, E_{X^0}, for many QDs as a function of the VC-area, A_{VC}. The plot is obtained by combining three independent PL-maps from sample A. We find a strong negative (Pearson) correlation coefficient of $\rho = -0.812$ (sample B: $\rho = -0.809$) between emission energy and A_{VC} ($\rho = \pm 1$ maximum correlation; $\rho = 0$ no correlation). We explain this correlation by applying the capture-zone model to the growth phase of the Al-droplets (Fig. 4.1(a)). An Al-atom, impinging at a random position on the sample, moves on the surface via diffusion and is most likely to attach to the closest Al-droplet. In the capture-zone model, the growth rate of an Al-droplet is thus assumed to be proportional to the VC-area. If all Al-droplets form at about the same time (sudden nucleation [221]), it leads to a correlation between Al-droplet volume and VC-area. For an Al-droplet with a small VC-area, much material nucleates at its nearest neighbors reducing its own accumulation rate. In turn, an Al-droplet with a larger VC-area accumulates more atoms. Thus, the droplet-volume V_d becomes larger. For a larger Al-droplet, the nano-hole etched underneath it becomes deeper [201]. The QD subsequently formed from this nano-hole has a weaker confinement in the growth direction lowering its emission energy.

We obtain a quantitative relation between A_{VC} and the emission energy by the following considerations. In the capture-zone model, the volume of each Al-droplet is proportional to A_{VC}. We assume that all Al-droplets have a similar aspect ratio [215, 227]. Then the droplet-height H_d is connected to the droplet-volume V_d and to the VC-area by $H_d \propto V_d^{1/3} \propto A_{\mathrm{VC}}^{1/3}$. For the relation between QD-height H (nano-hole depth, respectively) and the droplet-height H_d [201], we assume a phenomenological relation $H \propto H_d^{\beta}$. Since H is much smaller than the lateral extent of a QD [201], it is this parameter which mainly determines the emission energy of the QD. In the case of a hard-wall confinement and without considering Coulomb interaction terms, the emission energy of a QD is given by the bandgap plus electron and hole confinement energy: $E = E_0 + \frac{h^2}{8\mu H^2}$, where $E_0 = 1.519$ eV is the bandgap of the QD-material (GaAs) and $\mu = \left(\frac{1}{m_e^*} + \frac{1}{m_h^*}\right)^{-1}$

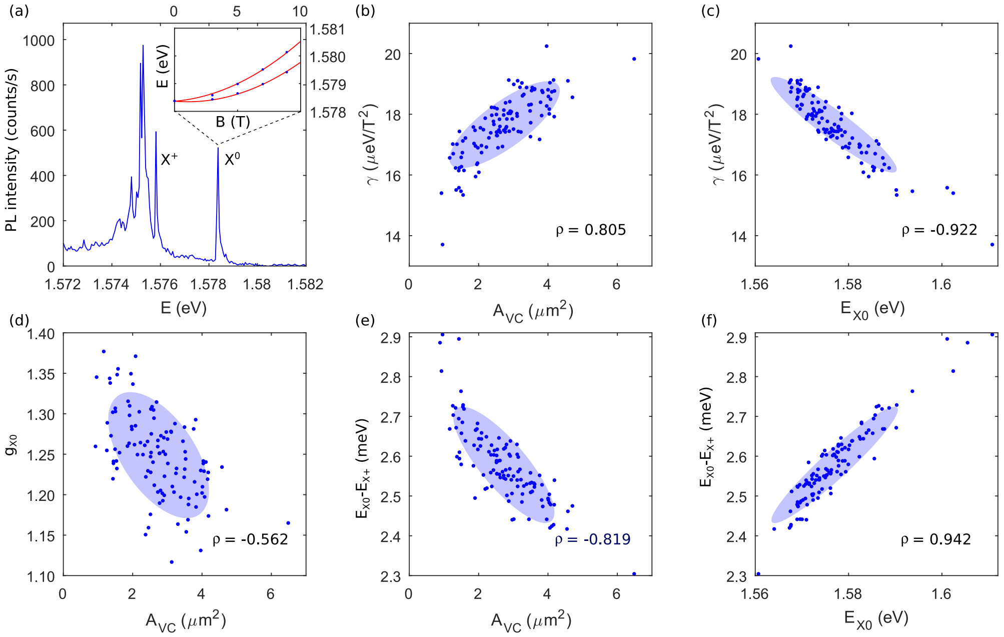

Fig. 4.2: (a) An exemplary PL-spectrum of a QD. The emission line at the highest energy is the neutral exciton (X^0). At lower energy, emission of a singly-charged exciton (X^+) and a broad emission from further excitons appear. The inset shows the X^0 emission energy as a function of the magnetic field. A diamagnetic shift and a Zeeman splitting are observed. The following sub-figures refer to emission from X^0 on sample A. (b) Diamagnetic shift as a function of A_{VC} ($\rho = 0.805$). The light blue ellipse has the same slope as a linear fit to the data points; its widths indicate a 1.5σ-interval parallel and perpendicular to the slope. (c) Diamagnetic shift as a function of the emission energy of the neutral exciton. These parameters are negatively correlated (correlation coefficient $\rho = -0.922$). (d) A weak correlation between the exciton g-factor and the Voronoi-cell area, A_{VC}. (e) Splitting between neutral and positively-charged excitons ($E_{X0} - E_{X+}$) as a function of A_{VC} ($\rho = -0.819$). (f) $E_{X0} - E_{X+}$ as a function of X^0 emission energy ($\rho = 0.942$).

the reduced electron-hole effective mass ($m_e^* = 0.067 m_e$, $m_h^* = 0.51 m_e$). Including the $d = 2$ nm thick quantum well above the QDs leads to $E = E_0 + \frac{h^2}{8\mu(H+d)^2}$. Using the above relations one obtains an equation connecting A_{VC} and the emission energy E of the QD:

$$E = E_0 + \frac{h^2}{8\mu} \cdot \left((\alpha \cdot A_{\mathrm{VC}})^{\beta/3} + d \right)^{-2} \tag{4.1}$$

A fit of Eq. 4.1 to the data is shown in Fig. 4.1(f). With the fit parameters $\alpha = 1.268 \cdot 10^{-32}$ m$^{3/\beta - 2}$ and $\beta = 0.556$, we find a very good agreement with the data.

The average height of a QD resulting from this fit is $H = 8.7$ nm which agrees well with AFM-measurements (see section 4.7). A direct correlation between the measured emission energy E_{X^0} and the term on the right-hand side of Eq. 4.1 shows an even higher correlation of $\rho = 0.879$ (see section 4.8) than that between emission energy and A_{VC}. This strong correlation supports our model for the connection between QD-properties and capture zone.

We consider further QD-properties and their connection to the VC-area, A_{VC}: the diamagnetic shift of the QD-emission, and the splitting between neutral and positively-charged exciton, $E_{X^0} - E_{X^+}$. Both of these QD-properties are connected mainly to the lateral rather than the vertical confinement of the QD.

We measure the energy of the PL-emission (X^0) as a function of a magnetic field applied in the growth direction (inset to Fig. 4.2(a)). The magnetic field splits the emission lines by the Zeeman energy and leads to a diamagnetic shift. For every QD we fit the relation [76, 228]

$$E\,(B) = E(B = 0) + \gamma B^2 \pm \frac{1}{2} g \mu_B B, \tag{4.2}$$

where g is the exciton g-factor and μ_B the Bohr magneton. We approximate the diamagnetic shift with a parabola with prefactor γ [76, 228]. The fine structure splitting of the studied QDs [215] is negligibly small in this context. For the diamagnetic shift, a probe of the lateral area of the exciton, we find values in the range $\gamma = 15 - 20$ μeV/T^2, in good agreement with Ref. [229]. The dependence of γ on the VC-area (A_{VC}) is shown in Fig. 4.2(b). We find a correlation of $\rho = 0.805$ between A_{VC} and γ, which reveals a connection between the capture-zone area and the lateral size of a QD. An Al-droplet with a larger VC-area has a larger lateral extent leading to a QD with a weaker lateral confinement potential. This finding is also fully compatible with the capture-zone model. For the direct dependence between the emission energy, E_{X^0}, and the diamagnetic shift, γ, we find an approximately linear relation (Fig. 4.2(c)) associated with a correlation of $\rho = -0.922$. This connection between vertical and lateral confinement is consistent with a reported correlation between emission energy and s-to-p-shell–splitting [226].

A plot of the exciton g-factor versus A_{VC} is shown in Fig. 4.2(d). The g-factor shows a slight dependence on A_{VC} with $\rho = -0.562$. For these QDs, the electron g-factor is very small such that the exciton g-factor is determined largely by the hole g-factor [195, 229]. The hole states are predominantly heavy hole in character. However, even a small admixture of light-hole states reduces the g-factor from the heavy hole limit by a large amount [230, 231]. This light-hole admixture is size-dependent, which can explain the dependence of the g-factor on A_{VC}. However, the g-factor is more weakly correlated with A_{VC} than the emission energy. We speculate that the hole g-factor is sensitive to the shape and not just the volume of the QD leading to a weaker correlation with A_{VC}.

Shown in Fig. 4.2(e) is the splitting between neutral and positively-charged exciton ($E_{X^0} - E_{X^+}$) as a function of A_{VC}. Using single-particle wavefunctions, $E_{X^0} - E_{X^+}$ can be associated with the term $E_{eh} - E_{hh}$, where E_{hh}, E_{eh} are the direct Coulomb integrals between two holes, and an electron and a hole, respectively [71, 172]. Both terms decrease with increasing lateral size of the QD and hence with increasing size of the VC-area, A_{VC}. Experimentally, we observe a monotonic relation between A_{VC} and $E_{X^0} - E_{X^+}$ with a negative correlation ($\rho = -0.819$). For the direct relation between $E_{X^0} - E_{X^+}$ and the emission energy E_{X^0}, we find a linear dependence corresponding to a pronounced correlation of $\rho = 0.942$ [232] (see Fig. 4.2(f)). This dependence also indicates a connection between the lateral and vertical confinements.

4.4 Conclusions

We show how the optical properties of QDs grown by GaAs-infilling of Al-droplet-etched nano-holes are connected to the capture-zone model, a concept from nucleation theory. The QD-positions and the optical QD-properties are obtained simultaneously by spatially resolved photoluminescence. The capture zone of QDs is determined by the Voronoi-diagram of the QD-positions. We find a strong negative correlation between the VC-area and the emission energy of QDs. This result can be explained with the capture-zone model applied to the growth-phase of the Al-droplets. A relation between VC-area and further optical properties (diamagnetic shift and neutral-to-charged exciton splitting) shows that not only the vertical but also the lateral QD-size is correlated with the area of the capture zone. We measure these correlations on samples with low QD-densities ($n_{\mathrm{QD}} < 1\ \mu\mathrm{m}^{-2}$). Properties of a QD on a nm-scale, which determine its optical emission, are therefore connected to its surroundings on a μm-scale. This result might be transferable to other nanostructures when strong material diffusion is present during the growth. The correlations between different QD-parameters facilitate the preselection of QDs for applications that place stringent requirements on the QD-properties. The correlation between emission energy and capture-zone area has a powerful implication: If all capture-zone areas are identical – e.g. by forcing the nucleation of the Al-droplets on a lattice – then a spectrally narrow wavelength distribution of the QD-ensemble can potentially be engineered. This idea has been successfully applied to stacked QD-layers, and QDs in pyramidal nanostructures [233, 234, 235, 236, 237, 238, 239]. For the system

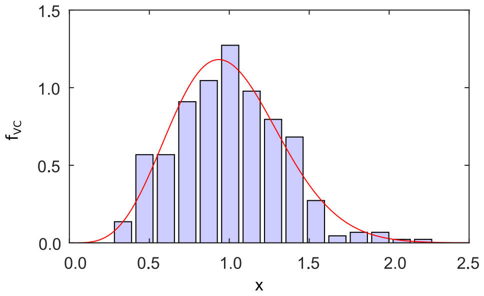

Fig. 4.3: Frequency distribution, f_{VC}, of the normalized Voronoi-cell area, $A_{\mathrm{VC}}/\langle A_{\mathrm{VC}}\rangle \equiv x$. For better visibility, the normalized Voronoi-cell areas are divided in finite intervals. The red line is a fit of Eq. 4.3 obtained by likelihood optimization.

investigated here, Fig. 4.1(f) indicates that the QD-ensemble would narrow by a factor of two if all Voronoi-cell areas were in a range of $3-4\ \mu\mathrm{m}^2$.

4.5 Frequency Distribution of the Voronoi-Cell Areas

The frequency distribution of the VC-areas gives further information about the Al-droplet formation. The probability density distribution, f_{VC}, of the normalized Voronoi-cell areas, $A_{\mathrm{VC}}/\langle A_{\mathrm{VC}}\rangle \equiv x$, is often modeled by a generalized Wigner distribution [240, 241]:

$$f_{\mathrm{VC}}(x \mid \eta) = a_\eta \cdot x^\eta \cdot \exp\left(-b_\eta x^2\right). \tag{4.3}$$

In our notation, $f(x \mid \eta)$ corresponds to a probability density distribution for x under the condition η. The parameters b_η and a_η are defined by the constraint that f_{VC} is a normalized probability density distribution with a mean of 1. Explicit expressions for b_η, a_η are given in Refs. [242, 243]. The parameter η can be connected to the critical nucleus size, i, via $\eta \approx i+2$ [241, 243, 244].

We fit Eq. 4.3 to the distribution of normalized VC-areas via likelihood optimization, without making approximations such as Poissonian or Gaussian error estimation [245]. Let $\{A_{\mathrm{VC}}^{(i)}\}_{i\in\{1..N\}}$ be the set of the areas corresponding to the N different Voronoi cells. We define $\{x^{(i)}\}_{i\in\{1..N\}}$ as the set of all normalized Voronoi-cell areas, $x^{(i)} = A_{\mathrm{VC}}^{(i)}/\langle A_{\mathrm{VC}}\rangle$. Eq. 4.3 assigns a probability density to each value $x^{(i)}$. We assume that every value $x^{(i)}$ corresponds to an independent random variable, $X^{(i)}$. Then, under the condition of a fixed value for η, the probability density of measuring a set of normalized Voronoi cells,

$\{x^{(i)}\}_{i\in\{1..N\}}$, is given by:

$$P\left(\{x^{(i)}\}_{i\in\{1..N\}} \mid \eta\right) = \prod_{i=1}^{N} f_{\mathrm{VC}}(x^{(i)} \mid \eta). \tag{4.4}$$

This likelihood distribution is maximum for $\eta = \eta_{opt} = 3.66$. The mean of the likelihood distribution is $\eta_m = 3.68$. The difference between mean and maximum of the likelihood distribution is small because the distribution is close-to symmetric and only slightly biased. The found value of the parameter η corresponds to a critical nucleus size of $i \approx 2$.

The likelihood distribution, $P\left(\{x^{(i)}\}_{i\in\{1..N\}} \mid \eta\right)$, has a standard deviation of $\sigma_\eta = 0.33$ when varying η for a fixed measurement, $\{x^{(i)}\}_{i\in\{1..N\}}$. Bayes' theorem connects the probability density for measuring $\{x^{(i)}\}_{i\in\{1..N\}}$ under the condition of a fixed parameter η to the probability density for η under the condition of a measurement, $\{x^{(i)}\}_{i\in\{1..N\}}$:

$$P\left(\eta \mid \{x^{(i)}\}_{i\in\{1..N\}}\right) = \frac{P\left(\{x^{(i)}\}_{i\in\{1..N\}} \mid \eta\right) \cdot P\left(\eta\right)}{P\left(\{x^{(i)}\}_{i\in\{1..N\}}\right)}. \tag{4.5}$$

The distribution $P\left(\{x^{(i)}\}_{i\in\{1..N\}}\right)$ does not depend on η. Furthermore, we assume a uniform prior distribution, $P\left(\eta\right)$. In this case, both probability density distributions $P\left(\eta \mid \{x^{(i)}\}_{i\in\{1..N\}}\right)$ and $P\left(\{x^{(i)}\}_{i\in\{1..N\}} \mid \eta\right)$ are equal up to a prefactor which does not depend on η. Therefore, the width of both distributions is identical. The error on the parameter η is given by $\sigma_\eta = 0.33$, the standard deviation calculated for the likelihood distribution, $P\left(\{x^{(i)}\}_{i\in\{1..N\}} \mid \eta\right)$.

Shown in Fig. 4.3 is the distribution of the relative frequency, f_{VC}, of the normalized VC-area, $A_{\mathrm{VC}}/\langle A_{\mathrm{VC}}\rangle \equiv x$. In this figure, the normalized Voronoi-cell areas, $\{x^{(i)}\}_{i\in\{1..N\}}$, are divided in finite intervals. The solid red line is the fit ($\eta = \eta_{opt} = 3.66$) of Eq. 4.3 to the data, $\{x^{(i)}\}_{i\in\{1..N\}}$.

4.6 Correction of the Non-Linearity of the Piezo-Scanners

The determination of Voronoi-cell sizes is based on measuring the PL as a function of the position. Such a PL-map is carried out by scanning the sample position with piezo-electric xy-scanners. The scanners have a hysteresis which, however, does not affect our measurements as we perform all measurements while scanning in the forward direction. Besides, the piezo-scanner position depends non-linearly on the applied voltage. This non-linearity could potentially be corrected by calibrating the piezo-scanners with a well-defined reference-structure. Here, we use a different approach: The emission spot of a QD appears differently in size depending on the absolute position of the scanner. The QD spot size is a direct measure of the non-linear dependence between the applied piezo-voltage and the position. The lateral size of a QD itself (< 40 nm) is negligible in comparison to the spot size. We can, therefore, use the widths of the QD spots as a reference to compensate for the distortion of the PL-map. The corresponding procedure is explained in the caption of Fig. 4.4. The distortion correction works well due to the large number of QDs on each PL-map. A comparison of a PL-map with and without distortion correction is shown in Fig. 4.4(c, d).

4.7 AFM-Measurement

We perform an AFM-measurement on a reference sample for which the growth is stopped after the etching of the nano-holes. An AFM-image of a 5×5 μm^2 large region is shown in Fig. 4.5. The measurement suggests that nano-holes with other nano-holes in their proximity are shallower in comparison to more separated ones. This finding is consistent with the capture zone model and the results obtained by spatially resolved photoluminescence. The size of the AFM-image does not allow for a quantitative analysis comparable to which is done based on the spatially resolved PL-measurements.

4.8 Emission Energy and Voronoi-Cell Area

Shown in Fig. 4.6 is the dependence between the emission energy and the Voronoi cell (VC) area, A_{VC}, for the two different samples (A, B). For both samples, we observe that the emission energy decreases with increasing Voronoi-cell area, A_{VC}.

Eq. 4.1 suggests that the relation between A_{VC} and emission energy is non-linear. In Fig. 4.6 we plot the emission energy as a function of the expression on the right-hand side of Eq. 4.1. The correlation of this dependence is higher ($|\rho| = 0.879$) than the correlation between emission energy and A_{VC} ($|\rho| = 0.812$). This result suggests that Eq. 4.1 is a better description of the data than a linear approximation.

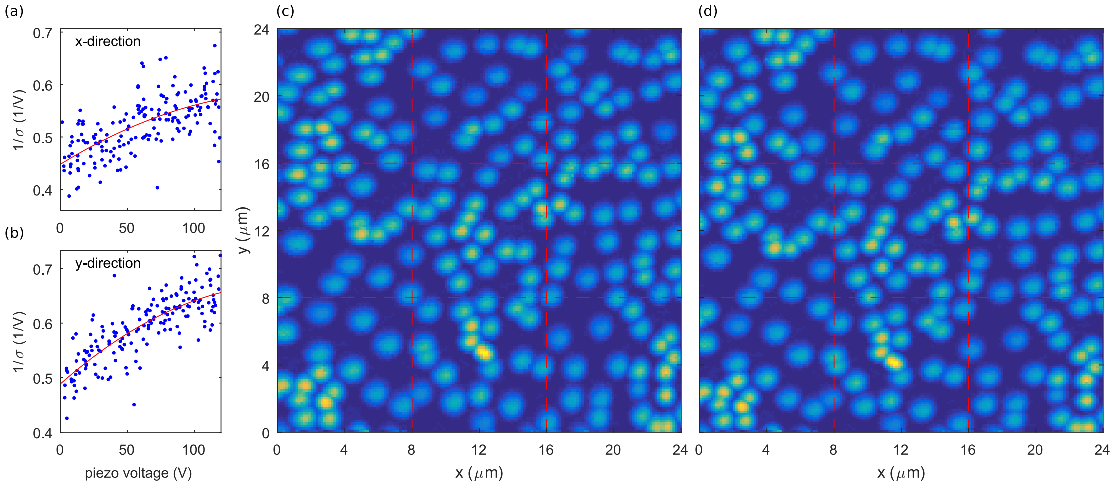

Fig. 4.4: Correction of the distortion due to the non-linearity of the piezo-scanners. The QD-position is set by the voltages $V_{x/y}$ applied to the piezo-scanners. The distortion correction is carried out independently for the (a) x- and (b) y-directions (x-direction in the following explanation). Initially, the spot size σ_x is measured for every QD in units of the voltage applied to the piezo-scanner. It is obtained by fitting a 2D Gaussian to the PL-intensity. The PL is spectrally filtered to select individual QDs. For a larger derivative $\frac{\mathrm{d}x}{\mathrm{d}V_x}$, the spot size appears smaller than for a smaller value of $\frac{\mathrm{d}x}{\mathrm{d}V_x}$. The spot size σ_x is therefore inversely proportional to the derivative $\frac{\mathrm{d}x}{\mathrm{d}V_x}$. The red curves in (a), (b) are fits to a phenomenological parabolic dependence between applied piezo-voltage V_x and $1/\sigma_x$: $\frac{\mathrm{d}x}{\mathrm{d}V_x} = \tilde{c}/\sigma_x = \tilde{c}(a_0 + a_1 V_x + a_2 V_x^2)$. We use the fit results to map V_x to the position $x(V_x) = \tilde{c}\int_0^{V_x}(a_0 + a_1 V + a_2 V^2)\,\mathrm{dV}$. The prefactor $\tilde{c}$ is obtained by the constraint that the highest voltage corresponds to the full scan range. (c) PL-intensity as a function of the xy-position. The PL is integrated over the full QD-ensemble. The PL-map is shown without the distortion correction, assuming that position and applied piezo-voltage are related linearly. Due to the described non-linearity of the piezo-scanners, the QD-spots at low voltages appear slightly larger in comparison to the QD-spots at high voltages – the PL-map is distorted. (d) The same PL-map with a distortion correction using the above method. The QD-spot sizes are homogeneous indicating a successful correction of the distortion.

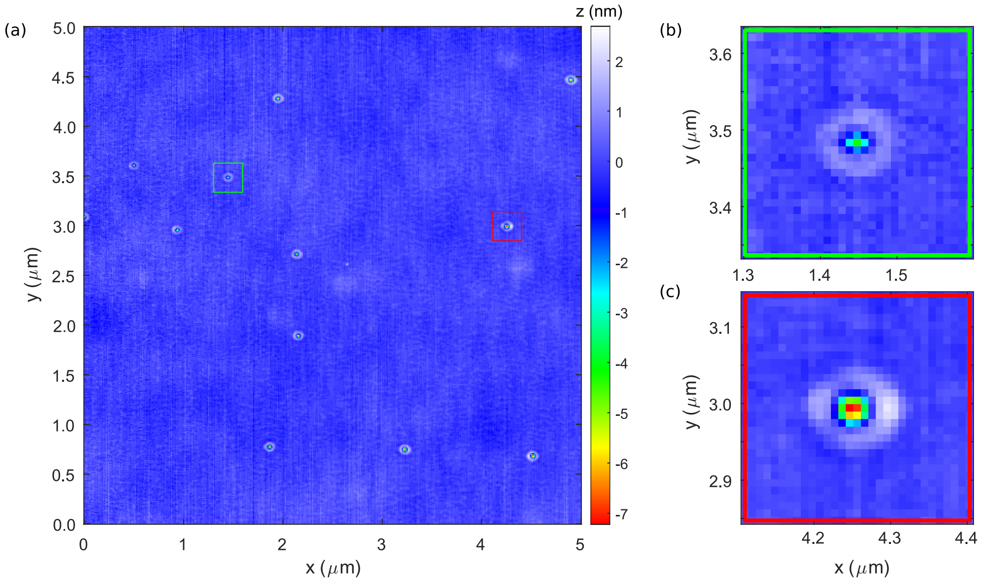

Fig. 4.5: (a) An atomic force microscopy (AFM) image on a sample similar to sample A. The growth is stopped after etching the nano-holes. The size of the AFM-scan is $5 \times 5\ \mu m^2$ with 512×512 pixels. The AFM-image indicates that the more separated nano-holes (with a larger VC-area) are deeper than those with a close-by neighbor. This finding is in good agreement with the results shown in section 4.3. A zoom-in of two nano-holes is shown in (b, c) to illustrate this observation. The first nano-hole has several close-by neighbors and is shallow. In contrast, the second nano-hole is more isolated and is particularly deep. The image size and resolution are too low to allow for a quantitative statistical analysis comparable to section 4.3. Note that an AFM-image comparable in size to the presented PL-measurements, simultaneously imaging individual nano-holes with ~ 2 nm resolution, would have to be $\sim 10^4 \times 10^4$ pixels large – a very time-consuming measurement.

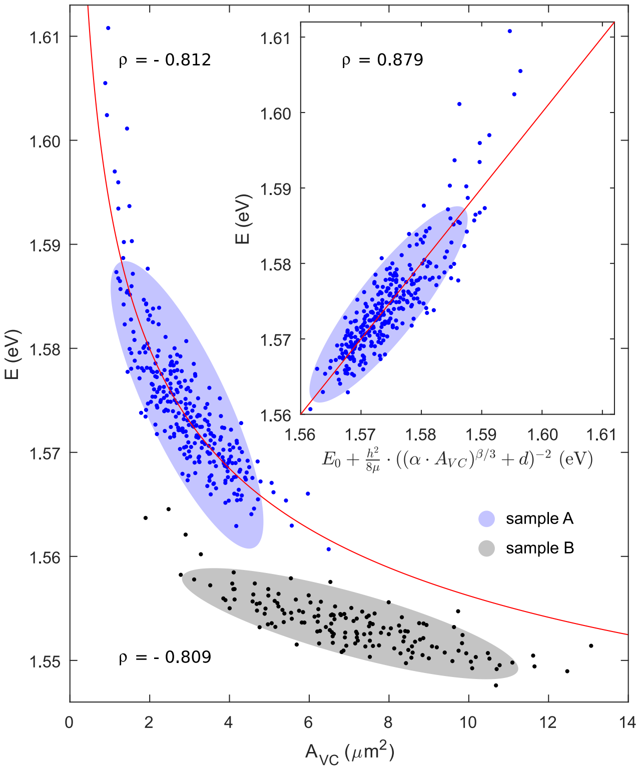

Fig. 4.6: Emission energy (X^0) as a function of Voronoi-cell area (A_{VC}). The red line is a fit to Eq. 4.1 for QDs on sample A (blue points). Inset: emission energy of QDs on sample A as a function of the expression on the right-hand side of Eq. 4.1. The relation between both quantities is more linear (correlation coefficient $|\rho| = 0.879$) than the direct relation of emission energy and A_{VC} ($|\rho| = 0.812$) which supports Eq. 4.1. QDs on sample B (black data points) are red-shifted compared to QDs on sample A.

Chapter 5

Radiative Auger Process in the Single-Photon Limit

This section is partly adapted from Ref. [246]: ”Radiative Auger Process in the Single Photon Limit on a Quantum Dot”, Matthias C. Löbl, Clemens Spinnler, Alisa Javadi, Liang Zhai, Giang N. Nguyen, Julian Ritzmann, Leonardo Midolo, Peter Lodahl, Andreas D. Wieck, Arne Ludwig, and Richard J. Warburton, arXiv:1911.11784 (2019).

Abstract: In a multi-electron atom, an excited electron can decay by emitting a photon. Typically, the leftover electrons are in their ground state. In a radiative Auger process, the leftover electrons are in an excited state and a red-shifted photon is created [247, 248, 249, 250]. In a quantum dot, radiative Auger is predicted for charged excitons [251]. However, this process has not been observed on any single-photon emitter. Here, we report the observation of radiative Auger on trions in single quantum dots. For a trion, a photon is created on electron-hole recombination, leaving behind a single electron. We show that the red-shifted radiative Auger lines determine the quantization energies of this single electron precisely, information which is otherwise difficult to acquire. For this reason, radiative Auger is a powerful tool. Going beyond the original theoretical proposals, we show experimentally how quantum optics – an analysis of the photon correlations – gives access to the single-electron dynamics, notably relaxation and tunneling. All these properties of radiative Auger can be exploited on other semiconductor nanostructures and quantum emitters in the solid-state.

5.1 Introduction

In an atom or a semiconductor, an excited electron can relax by the emission of a photon. The excited electron can also relax nonradiatively by the excitation of another electron – an Auger process [252, 253]. Nonradiative Auger processes involving continuum states

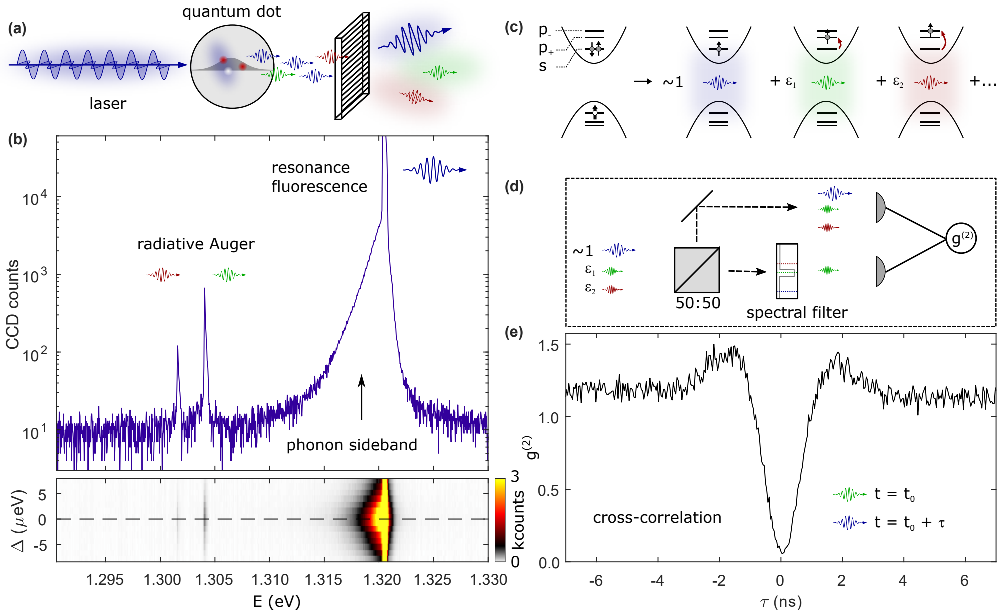

Fig. 5.1: **Observation of a radiative Auger process on a single quantum dot. (a)** Schematic setup: the quantum dot (QD) is resonantly excited with a narrow-bandwidth laser, and its emission is spectrally resolved. **(b)** Emission spectrum of the negative trion (X^{1-}) in an InGaAs QD under resonant excitation ($T = 4.2$ K). The strong peak at $E \simeq 1.321$ eV is the resonance fluorescence. Red-shifted by $\hbar\omega_0 \sim 18$ meV there are two additional emission lines, stemming from the radiative Auger process. The QD can be tuned in and out of the resonance with the laser via a gate voltage, V_g. The shown spectrum is measured at zero detuning, Δ, between QD and laser (dashed line). Resonance fluorescence and radiative Auger are maximum when QD and laser are in resonance ($\Delta = 0$). **(c)** The radiative Auger process: with a probability close to one, the trion recombination results in an emission of a resonant photon and leaves the remaining electron in the s-shell. With small probabilities $|\epsilon_1|^2$ and $|\epsilon_2|^2$, the remaining electron is promoted into one of the p-shells, and the photon is consequently red-shifted. **(d)** Setup for the cross-correlation between the radiative Auger emission and the resonance fluorescence. The delay τ corresponds to the duration between the arrival of a resonant photon on detector 2 after the detection of an Auger photon on detector 1. **(e)** Cross-correlation measurement between radiative Auger and resonance fluorescence.

have been observed in quantum dots [90], two-dimensional materials [254], color centers [255], and are a major factor in determining the efficiency of semiconductor lasers [256].

As originally predicted for atoms, an Auger process can also take place together with a radiative transition [249, 250]. In such a radiative Auger process, part of the available energy is transferred to another electron and the emitted photon is correspondingly red-shifted. The radiative Auger process has been observed in X-ray spectra [247, 248]. The so-called electron shake-off, which follows the beta-decay of a radioactive atom, has a similar physical origin [257]. At optical frequencies, the radiative Auger process has been described in ensembles of donors [258] and as a so-called shake-up process in the Fermi-sea [85, 259, 260], a many-particle effect. On a single-photon emitter or in a few-electron configuration, the radiative Auger process has not been observed. The prospect of applying quantum optics techniques to the radiative Auger photons has not been considered so far.

We measure the radiative Auger process at optical frequencies for the minimum number of two excited electrons. Radiative Auger is observed for a negative trion (an exciton consisting of two electrons and one hole), which is confined to a zero-dimensional quantum dot (QD) [251]. The radiative Auger process promotes the additional (Auger) electron to a higher shell of the QD. No continuum states are involved. The emitted photon is red-shifted by the energy which is transferred to the Auger electron. We show that the radiative Auger effect is a powerful probe for single electrons: the energy separations between the resonance fluorescence and the radiative Auger emission directly measure the single-particle splittings of the QD with very high precision. In semiconductors, these single-particle splittings are otherwise hard to access by optical means since particles are generally excited in pairs, as excitons. After the radiative Auger excitation, the Auger carrier relaxes back to the lowest shell of the confinement potential. With a quantum optics-based correlation measurement, we determine the rate corresponding to this single-particle relaxation in the absence of any other particles. Also this is typically hard to achieve by optical means: even for quasi-resonant *p*-shell excitation, electron relaxation takes place in the presence of a hole, which complicates the relaxation dynamics.

5.2 Experimental Results

We observe the radiative Auger process on two different systems: first, a self-assembled InGaAs QD in GaAs grown in the Stranski-Krastanov mode [251] and second, a GaAs QD in AlGaAs grown by infilling of droplet-etched nano-holes [211]. We resonantly excite the negative trion (X^{1-}) of a QD with a narrow-bandwidth laser. In both QD systems, the charge state of the QD is precisely controlled via Coulomb blockade [79]. We collect the emission of the QD and resolve it spectrally, as schematically shown in Fig. 5.1(a). Shown in Fig. 5.1(b) is the result of such a measurement for an InGaAs

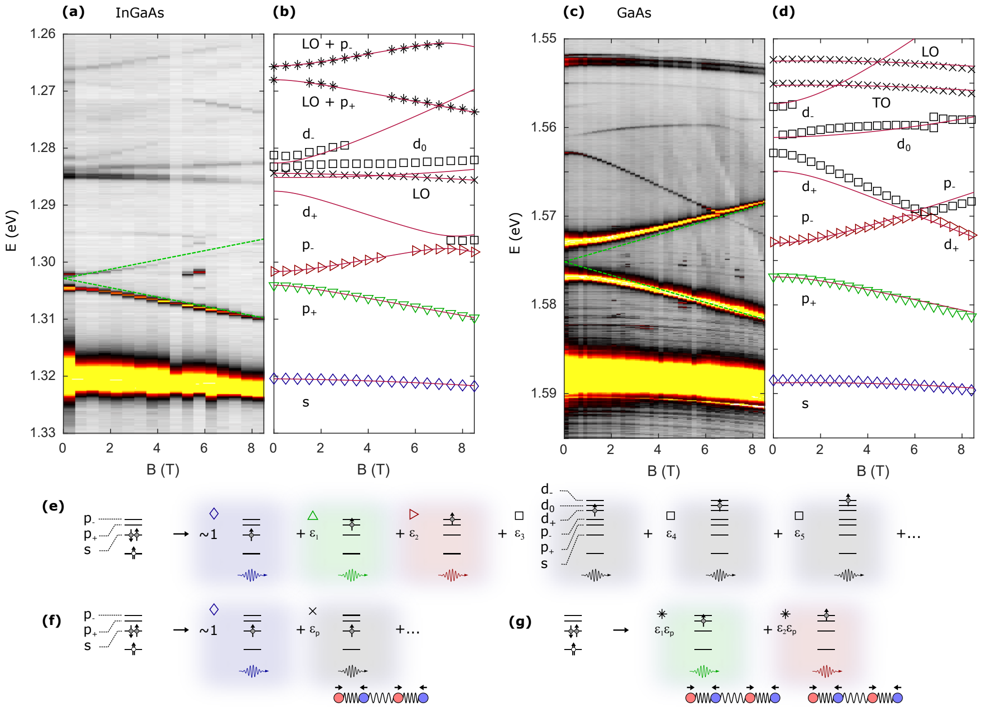

Fig. 5.2: **Magnetic field dispersion of the radiative Auger emission.** **(a)** Emission spectrum under resonant excitation as a function of the magnetic field measured on an InGaAs quantum dot (QD). The two green lines indicate the radiative Auger emission where one electron is promoted into the *p*-shells. This emission follows a dispersion of $\sim \pm\frac{1}{2}\hbar\omega_c$, with $m^* \simeq 0.071\ m_e$, *s*-to-*p*-splitting $\hbar\omega_0 \simeq 17.7$ meV. **(b)** Magnetic field dispersion of the radiative Auger emission. The emission lines above the *s*-shell can be well described by the Fock-Darwin spectrum. The red lines represent a fit of our analytical model of the radiative Auger emission (see Supplement section 5.4). **(c)** Radiative Auger emission as a function of the magnetic field measured on a GaAs QD ($m^* \simeq 0.076\ m_e$, $\hbar\omega_0 \simeq 13.8$ meV). **(d)** Magnetic field dispersion of the radiative Auger emission for the GaAs QD. **(e)** Schematics of the radiative Auger process involving both *p*- and *d*-shells. **(f)** Optical recombination involving the creation of an LO- or a TO-phonon. This process is observed for the trion and the neutral exciton (see Supplement Fig. 5.4(a)). **(g)** Schematics of the radiative Auger process involving both carrier excitation to the *p*-shell and the creation of a phonon.

QD. The main peak at photon energy ∼ 1.321 eV is the resonance fluorescence of the trion. This spectrally narrow emission is accompanied by an LA-phonon sideband on the red side [133, 134, 261]. Additionally, we observe two weak emission lines, red-shifted by ∼ 18 meV from the main fluorescence peak. In the following, we show that these emission lines originate from a radiative Auger process as illustrated in Fig. 5.1(c):

an electron and a hole recombine optically and with a small probability, the second electron is promoted to an excited state, the p-shell of the QD. In the case of resonance fluorescence, in contrast, the optical recombination of the trion leaves behind a single electron in the ground state (s-shell of the QD).

Several observations substantiate the interpretation that the two red-shifted lines originate from a radiative Auger process. First, the Auger lines disappear on removing the additional electron – they are absent in the emission spectrum of the neutral exciton, X^0 (see Supplement Fig. 5.4). Secondly, the red-shifted emission lines only appear when the laser is in resonance with the QD (Fig. 5.1(b)). Thirdly, the time-resolved cross-correlation between the radiative Auger emission and the resonance fluorescence (Fig. 5.1(d,e)) shows a pronounced anti-bunching at zero time-delay. This measurement demonstrates that the different emission lines originate from the same QD. The emitter produces either a resonance-fluorescence photon or a radiative-Auger photon, but never two photons at the same time. Finally, to prove that the radiative Auger process leaves an electron in a higher shell, we measure the optical emission as a function of the magnetic field (Faraday geometry). The magnetic field dispersion of the radiative Auger emission is shown in Fig. 5.2(a,b) for an InGaAs QD and in Fig. 5.2(c,d) for a GaAs QD. At high magnetic fields, the two red-shifted emission lines, which are the closest in energy to the resonance-fluorescence, have a dispersion of $\pm\frac{1}{2}\hbar\omega_c$ (cyclotron frequency: $\omega_c = \frac{eB}{m^*}$, electron effective mass m^*). This magnetic field dispersion shows that the emission is connected to an energy transfer to the p-shells. More generally, the strong magnetic field dispersion of the radiative Auger emission arises because the magnetic field creates an additional orbital confinement, which leads to a strong magnetic field dependence of higher QD-shells [63, 69, 70]. The magnetic field dependence is important to distinguish radiative Auger emission from phonon-related features.

The separation between resonance fluorescence and radiative Auger emission corresponds to the single-particle splittings. The radiative Auger lines, therefore, allow the single-particle spectrum of a quantum dot to be determined with high precision. At zero magnetic field ($B = 0$ T), there is a splitting between the two p-shell-related Auger lines, revealing an asymmetry of the QD. This asymmetry lifts the four-fold degeneracy of the p-shells into two doublets at zero magnetic field. For both types of QDs, we also observe radiative Auger emission at even lower energies (see Fig. 5.2(a,c)). These emission lines correspond to a radiative Auger process involving d-shells (Fig. 5.2(e)). At high magnetic fields, the upper p-shell (p_-) shows an anti-crossing with the lowest d-shell (d_+). For the GaAs QD, we even observe radiative Auger emission lines involving all three d-shells. For the InGaAs QD, the d_+-shell is only visible in the radiative Auger

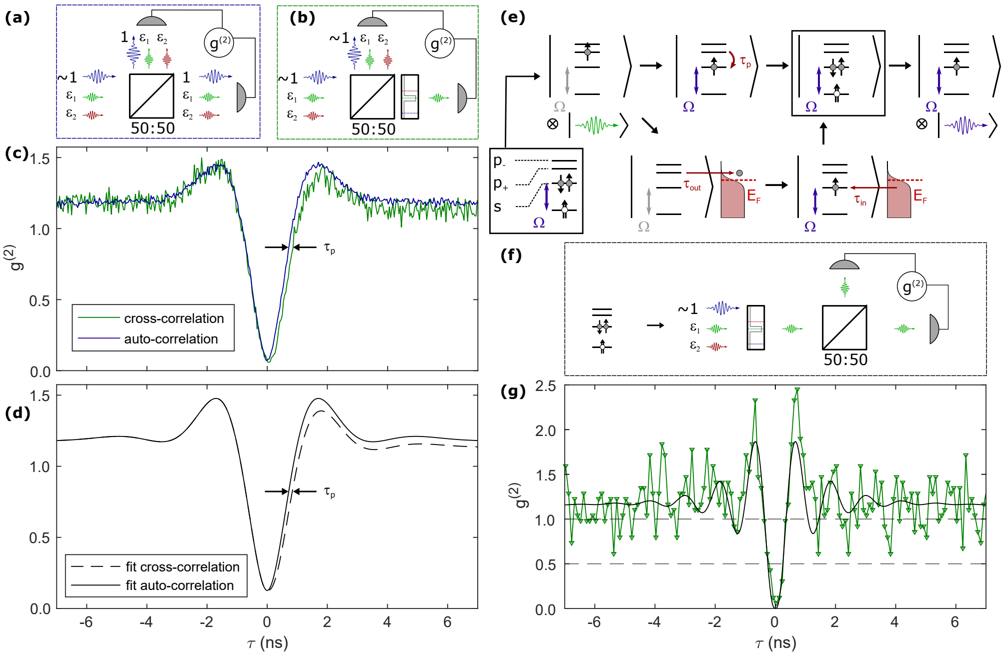

Fig. 5.3: **Time-resolved correlation measurements.** **(a)** Schematic of the measurement to determine the auto-correlation of the resonance fluorescence from a quantum dot (QD). The signal is split by a 50:50 beamsplitter; photon arrival times are recorded on two single-photon detectors ($g^{(2)}$-measurement). **(b)** Schematic of the cross-correlation measurement between resonance fluorescence and radiative Auger emission. The Auger emission is spectrally filtered to remove all resonant photons. **(c)** Cross-correlation between the resonance fluorescence and the radiative Auger emission (green), measured on the InGaAs QD shown in Fig. 5.1. An auto-correlation of the resonance fluorescence (blue) is shown for comparison. A time offset of $\tau_p \sim 85$ ps between the auto-correlation and the cross-correlation is a measure of the relaxation time of a single electron from the p- to the s-shell. **(d)** Fits to the auto- and cross-correlation measurements. (Parameters listed in Tab. 5.3) **(e)** Model for the dynamics connected to the radiative Auger process. After the radiative Auger excitation, the second electron occupies the p-shell of the QD. When the electron occupies the p- rather than the s-shell, the Coulomb interactions are different, tuning the s-to-s transition out of resonance with the laser. The QD cannot be re-excited until the electron has relaxed to the s-shell. There are two relaxation channels: a direct relaxation to the s-shell on a time scale τ_p; and ionization of the QD by tunneling from the p-shell to the Fermi-reservoir of the back gate (τ_{out}) followed by slower tunneling from the Fermi reservoir to the s-shell (τ_{in}). After relaxation, the QD is re-excited by the laser. **(f)** Schematic setup for the auto-correlation measurement of the radiative Auger emission. The radiative Auger signal is split and sent to two single-photon detectors. **(g)** Auto-correlation of the radiative Auger process involving the lower energy p-shell (green). The solid black line is a model where all parameters are identical to the simulation of the cross-correlation. Only the Rabi-frequency is higher compared to the cross-correlation measurement.

emission when it is coupled to the p_--shell. For both types of QDs, we model the dispersion of the emission lines by the Fock-Darwin spectrum [69, 70] (details in Supplement section 5.4). The model assumes a harmonic confinement potential and matches well for the lower QD-shells (see Fig. 5.2(a,c)). Differences between model and data (e.g. for the d-shells) reveal the deviation from a harmonic confinement potential towards higher single-particle energy.

For a rotationally symmetric confinement potential, angular momentum is a good quantum number such that promotion of the Auger electron to the d_0-shell is possible, but promotion to the other p- and d-shells is forbidden. In practice, we find that the radiative Auger involving the p-shells is relatively strong and that the intensity of these processes is not strongly dependent on the magnetic field. Besides, the p-shells are not degenerate at zero magnetic field. These observations show that angular momentum is not a good quantum number. However, we do not observe Zeeman splittings in the radiative Auger lines, which shows that the processes are spin-conserving. Spin is a good quantum number; equivalently, spin-orbit interactions of the electron states are weak.

There are several additional red-shifted emission lines that are not related to electron shells or continuum states (see Fig. 5.2(a,b)): An emission red-shifted by ~ 36 meV (labeled LO in Fig. 5.2(b,d)) corresponds to an optical recombination along with the creation of an LO-phonon (Fig. 5.2(f)). The magnetic field dispersion is weak and follows the QD s-shell – no higher QD-shells are involved. At lower photon energies, even the LO-phonon replica of the radiative Auger emission is visible (labeled LO + $p_\pm$ in Fig. 5.2(b), schematic illustration in Fig. 5.2(g)). In this case, Auger carrier excitation into p-shells and LO-phonon creation occur simultaneously with the optical recombination. The identification of these lines is confirmed by the magnetic field dispersion which equals the dispersion of the radiative Auger emission (see Fig. 5.2(b)).

We turn to the dynamics of the radiative Auger process, i.e. the dynamics of the electron left in an excited state after a radiative Auger process. Detecting a photon from a radiative Auger process projects the Auger electron into one of the excited electron states. The dynamics of this single electron can be investigated by determining the time of subsequent emission events. The experiment involves measuring the $g^{(2)}(\tau)$ correlation function with high precision in the delay τ. We compare the auto-correlation of the resonance fluorescence (Fig. 5.3(a)) to the cross-correlation between the radiative Auger emission and the resonance fluorescence (Fig. 5.3(b)). This comparison provides immediate insight into the carrier relaxation mechanism following the radiative Auger process. The corresponding $g^{(2)}$-measurements are shown in Fig. 5.3(c).

The auto-correlation (blue curve) shows an anti-bunching ($g^{(2)} < 1$) at zero time delay, proving the single-photon nature of the resonance fluorescence. The anti-bunching is surrounded by a bunching ($g^{(2)} > 1$) at a non-zero time delay. This effect is caused by the onset of Rabi-oscillations under strong resonant driving. The cross-correlation (green curve) differs from the auto-correlation in two aspects: The $g^{(2)}(\tau)$ is a slightly asymmetric function of τ and has a time-offset towards positive τ. We can explain these features (see fit in Fig. 5.3(d)) with the mechanism shown in Fig. 5.3(e): After the emission of a radiative Auger photon, the second electron is located in a higher shell. Before re-excitation of the trion can take place, this electron has to relax down to the s-shell – in contrast to the resonance fluorescence where re-excitation is immediately possible. By comparing auto- and cross-correlation, we determine the relaxation time for an isolated electron to be $\tau_{\mathrm{p}} \simeq 85$ ps. The time-scale of the electron relaxation is comparable to numbers reported for weak nonresonant excitation [262, 263]. The relaxation is probably caused by a multi-phonon emission process [80, 264]. We stress the advantage of the present method: the radiative Auger process leaves only a single electron in a higher shell. In contrast to nonresonant excitation, all other carriers have disappeared and the relaxation of the electron can be investigated independently of other relaxation mechanisms.

The asymmetry of the cross-correlation measurement can be explained by ionization of the QD following the radiative Auger emission. In a higher shell, the electron has an enhanced tunneling rate out of the QD [114]. Following very fast relaxation down to the Fermi-energy, tunneling back into the s-shell of the QD takes about ten times longer, and the QD is ionized for a finite time. We estimate the corresponding tunneling times by modeling the auto- and cross-correlation measurements. The full model and the fit results are given in the Supplement (section 5.6); the fits describe the experimental data well (see Fig. 5.3(d)).

Finally, we perform the first auto-correlation measurement of the radiative Auger emission. For this measurement, all the resonance fluorescence is filtered out (Fig. 5.3(f)). To maximize the count rate of the weak radiative Auger emission, we use a higher Rabi-frequency compared to the cross-correlation measurement. The auto-correlation measurement is shown in Fig. 5.3(g). At zero time delay, there is a clear anti-bunching in the $g^{(2)}$-measurement, which proves the single-photon nature of the emission connected to the radiative Auger process. At non-zero time-delay, the onset of Rabi-oscillations in the s-to-s transition is visible as a photon bunching of the radiative Auger emission. Both features are well described by our model (see Supplement section 5.6).

The radiative Auger process takes place because the interactions between the carriers forming the trion change the eigenfunctions of the system (see Supplement section 5.5).

In a single-particle basis, the initial state contains admixtures of Slater determinants [265, 266] of higher single-particle shells. The optical recombination removes an electron-hole pair from the initial trion state, leading to a final state which is a superposition of single-electron single-particle states. Every state in that superposition consists of an electron in a particular shell along with a photon of a certain energy. Since the initial state is always the same, the energy separations between the different emission lines correspond to precise single-particle splittings. The ratio of radiative Auger emission and resonance fluorescence reflects the expansion of the trion state in single-particle states. Compared to the resonance fluorescence, the radiative Auger emission is weaker by about 2–3 orders of magnitude for both types of QDs. It is slightly stronger for the larger GaAs QDs. The trion wavefunctions are close, yet not equal to, single-particle states.

In conclusion, we experimentally demonstrate that there is a radiative Auger process connected to the optical recombination of a trion in a single QD. The measurements are performed on negatively-charged trions in two different types of semiconductor QDs. We show how the radiative Auger process enables the behavior of a single electron to be determined in the QD (energy quantization, relaxation and tunneling dynamics) using the precise, sensitive and fast tools of quantum optics. The radiative Auger process only requires significant Coulomb interactions within the trion, a very general feature. Therefore, this process should also be observable for the positively-charged trion and other quantum emitters in the solid-state.

5.3 Experimental Methods

The samples are grown by molecular beam epitaxy. Sample A contains InGaAs QDs embedded in a *p*-*i*-*n*-*i*-*n*-diode structure [91, 107, 120, 267]. Sample B contains GaAs QDs in AlGaAs, which are grown by GaAs-infilling of Al-droplet etched nano-holes [66, 211]. The photon out-coupling is enhanced by a distributed Bragg mirror below the QDs. For both samples, the QDs are placed between a *p*-doped top gate and an *n*-type doped back gate. The QDs are tunnel-coupled to the back gate. This configuration stabilizes the charge environment of the QDs and enables tuning the QD charge state by applying a voltage between top and back gate [20, 87]. For the InGaAs QDs, the back gate has a distance of 40 nm to the QDs, 30 nm for the GaAs QDs. In a magnetic field, there is optical spin-pumping in the center of the trion charge plateau [23, 98]. Therefore, we perform all experiments at the plateau edges, where co-tunneling randomizes the electron spin [112].

All time-resolved measurements are performed by using superconducting single-photon detectors. The overall timing resolution for the $g^{(2)}$-measurements is IRF $\simeq 35$ ps (full width at half maximum). Optical measurements are carried out at 4.2 K in a helium bath cryostat. Resonant excitation of the QDs is performed with a narrow-bandwidth (~ 1 MHz) tunable diode laser (Toptica DLpro), which is additionally filtered with a home-built grating setup in order to remove any background from the gain medium of the laser. Resonance fluorescence of individual QDs is measured by suppressing the reflected laser light with a cross-polarization technique.

5.4 Modeling the Magnetic Field Dispersion

The radiative Auger emission appears on resonantly exciting the trion. Fig. 5.4(a) shows a comparison of the emission spectrum from a neutral exciton and a trion. The emission spectrum of the neutral exciton (X^0) only shows phonon-related features. A radiative Auger emission is impossible for the X^0 due to the absence of an Auger electron.

The final states after the optical recombination of the trion are single-particle states. Therefore, the separations between the different emission lines are precise single-particle splittings. Shown in Fig. 5.4(b,c) is the magnetic field dispersion of the extracted single-particle splittings for two different QDs. Fig. 5.4(d,e) shows the single-particle dispersion for the two QDs shown in Fig. 5.2. At zero magnetic field, we measure an s-to-p-splitting of 17.7 meV respectively 21.0 meV on the InGaAs QDs; and 13.8 meV respectively 17.6 meV on the GaAs QDs. We can determine many further parameters of the single-particle spectrum by fitting the data to a model which assumes states of an asymmetric harmonic confinement potential. The red lines in Fig. 5.4(b-e) represent the model that is developed in this section. It reproduces the data very well.

For a symmetric, two-dimensional, and harmonic confinement potential, the magnetic field dependence of the single-particle states forms the Fock-Darwin spectrum [69, 70]. The eigenergies $E_{n,L}$ depend on two quantum numbers, the radial quantum number, n, and the angular momentum quantum number, L [63]. In this model, the two p-shells are degenerate at zero magnetic field. This is clearly not the case in our experiments. To describe the single-particle dispersions, we therefore assume an asymmetric harmonic confinement potential of the form $V(x,y) = \frac{1}{2}m_e^*\left(\omega_x^2x^2 + \omega_y^2y^2\right)$. When the radial symmetry is broken, angular momentum is no longer a good quantum number, and the eigenenergies are $E_{n_x,n_y} = \hbar\omega_x\left(n_x + \frac{1}{2}\right) + \hbar\omega_y\left(n_y + \frac{1}{2}\right)$, with the two quantum numbers n_x and n_y. The eigenenergies of such an asymmetric harmonic confinement as a function of the magnetic field are given in Ref. [74].

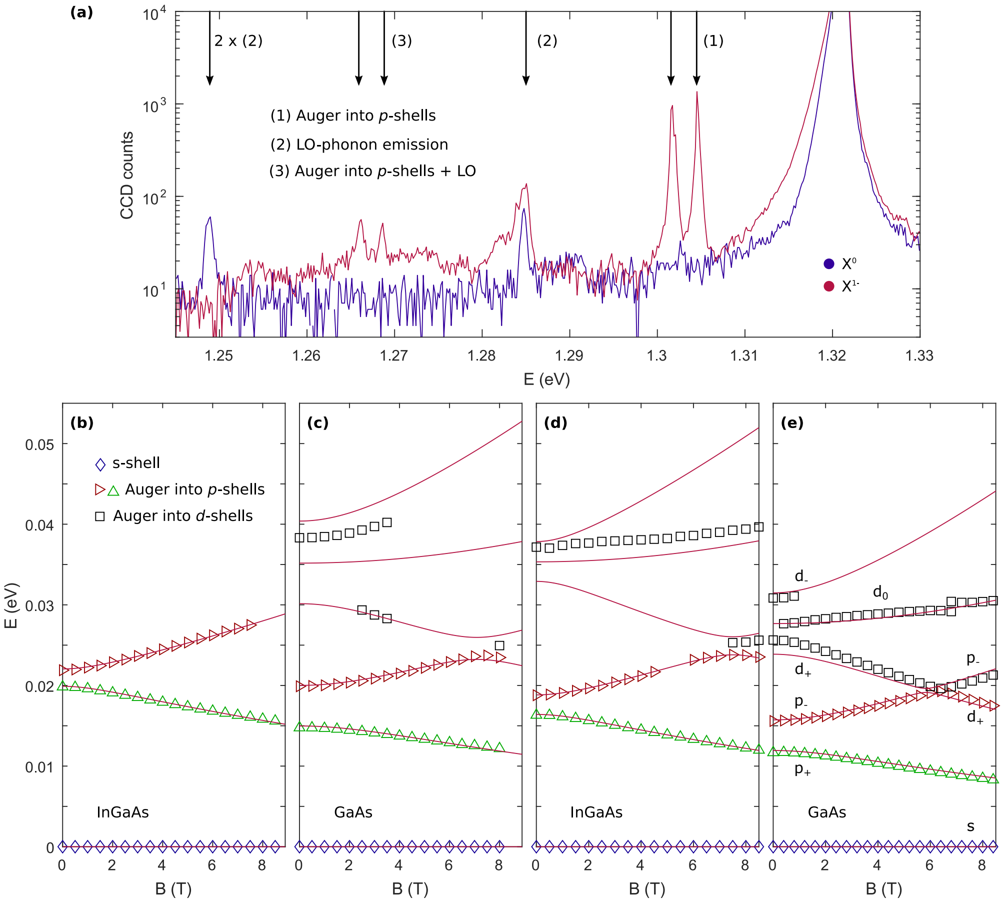

Fig. 5.4: **(a)** Emission spectrum for resonant s-to-s excitation of the InGaAs quantum dot (QD) in Fig. 5.2(a). For better comparability, X^0 (blue) is shifted in energy such that the resonance fluorescence peak overlaps with X^{1-} (red). The resonance fluorescence ($E \simeq 1.321$ eV) dominates, emission at lower energies is caused by an energy transfer to either phonons or an additional carrier via the radiative Auger process. The radiative Auger process is only possible for X^{1-}, not for X^0. **(b)** Magnetic field dispersion of the single-particle splittings for another InGaAs QD. To obtain the single-particle splittings, the s-shell energy is subtracted. **(c)** Single-particle splittings for another GaAs QD embedded in AlGaAs. **(d)** Single-particle splittings for the QD shown in Fig. 5.2(a). **(e)** Single-particle splittings for the QD shown in Fig. 5.2(c).

The absolute energies of the emission lines correspond to the energy differences between the initial state (E_{trion}) and the final states (E_{f}). To fit the dispersions of these emission lines, we compute the energy of the initial trion state as the sum of its single-particle energies plus the corresponding Coulomb and exchange terms. For the Coulomb

label	description
$\hbar$	reduced Planck constant
μ_B	Bohr magneton
ϵ_0, ϵ_r	permittivity of vacuum, relative permittivity
g_e, g_h	electron and hole g-factor
E_0	bandgap of the QD-material
m_e^*, m_h^*	electron, hole effective mass
$\hbar\omega_c = \frac{\hbar e B}{m_e^*}$	electron cyclotron energy
$\hbar\omega_x$, $\hbar\omega_y$	confinement energies of the asymmetric harmonic oscillator
$\hbar\omega_0 \equiv \hbar\omega_x + \Delta_p \equiv \hbar\omega_y - \Delta_p$	confinement energy of the symmetric harmonic oscillator
n, L	quantum numbers for the symmetric harmonic oscillator
n_x, n_y	quantum numbers for the asymmetric harmonic oscillator
$E_{n,L}$	eigenenergies of the symmetric harmonic oscillator
Δ_{pd}	coupling between p_-- and the d_+-shell
Ω_R	Rabi frequency
$\Gamma_r = \tau_r^{-1}$	radiative decay rate
$\Gamma_A = \tau_A^{-1}$	radiative Auger decay rate
$\Gamma_p = \tau_p^{-1}$	relaxation rate from p- to s-shell
$\Gamma_\mathrm{out} = \tau_\mathrm{out}^{-1}$	tunnel rate out of the QD after a radiative Auger decay
$\Gamma_\mathrm{in} = \tau_\mathrm{in}^{-1}$	tunnel rate into the ionized QD
$E_\mathrm{f}^{p\pm}, E_\mathrm{f}^{d\pm}$, and $E_\mathrm{f}^{d_0}$	final state energies after Auger excitation into p- and d-shells
Δ_{LO}, Δ_{TO}	energies of longitudinal and transverse optical phonon

Table 5.1: List of definitions.

energy terms, we assume a symmetric confinement as the corresponding energy terms can be easily computed analytically [45, 71, 172]. Coupling terms admixing higher shells are not considered in this estimation [71, 172].

At a magnetic field of $B \simeq 8$ T, the p_-- and the d_+-shells anticross. This is not a feature of the energy spectrum of an asymmetric harmonic oscillator. The anti-crossing is included by a phenomenological coupling Δ_{pd} between p_-- and d_+-shell. We speculate that the coupling between both shells arises due to the deviation from a harmonic confinement.

When part of the energy is transferred to an LO-phonon, the corresponding photon energy is given by, $E_\mathrm{trion} - E_\mathrm{f}^s - \Delta_{LO}$. This emission has the same weak magnetic field dependence as the resonance fluorescence (s-shell emission).

The results of fitting our model are shown in Fig. 5.4 and Fig. 5.2. A list of definitions is given in Tab. 5.1, and the fit parameters are given in Tab. 5.2. For all measured QDs, the strong magnetic field dispersion of the radiative Auger emission lines is well reproduced.

	E_0 (eV)	m_e^* (m_0)	$g_h - g_e$ (a. u.)	$\hbar\omega_0$	Δ_p	Δ_{pd}	Δ_{LO}	Δ_{TO}
1)	1.3214	0.0712	1.505	17.67	1.26	1.12	36.1	–
2)	1.5925	0.0757	1.135	13.84	1.90	0.25	36.3	33.5
3)	1.3152	0.0762	1.968	20.98	1.08	–	–	–
4)	1.5757	0.0737	1.1	17.59	2.61	1.37	36.5	–

Table 5.2: Fit results for the magnetic field dispersion. Unless otherwise stated, all parameters are given in meV. (1) InGaAs, Fig. 5.2(b) (2) GaAs, Fig. 5.2(d) (3) InGaAs, Fig. 5.4(b) (4) GaAs, Fig. 5.4(c).

In the case of the InGaAs QD shown in Fig. 5.2(a,b), we fit the energies of the s-shell emission and the radiative Auger emission into both p-shells simultaneously. The coupling term Δ_{pd} is included as a fit parameter. The exciton g-factor is measured independently by mapping out the charge plateau of the trion in a magnetic field. The fit reproduces the data very well and gives a good description of the radiative Auger excitation into some of the d-shells. The LO-phonon replica of the radiative Auger excitation into the p-shells is also excellently reproduced by the fit.

To fit the magnetic field dispersion of the InGaAs QD shown in Fig. 5.4(b), we also make a simultaneous fit to the energies of the s-shell emission and the radiative Auger emission into both p-shells. The coupling term Δ_{pd} is not included as there is no hint of an anticrossing with the d_+-shell.

For the GaAs QD shown in Fig. 5.2(c,d), we again fit the energies of the s-shell emission and the radiative Auger emission into both p-shells simultaneously. The coupling term Δ_{pd} is included as a fit parameter. The exciton g-factor is measured independently and not fitted.

For the GaAs QD shown in Fig. 5.4(c), we also fit the energies of the s-shell emission and the radiative Auger emission into both p-shells simultaneously. The exciton g-factor is fixed to a value typical for GaAs QDs.

When observable, all phonon-related features are described using the fit results described above. A constant phonon energy is used as a single fit parameter.

5.5 Radiative Auger Process: Theory

To explain the radiative Auger process, we consider the interactions between the three particles forming the trion. We determine the multi-particle eigenstates, Ψ, for several carriers in the same QD by numerically solving the time-independent Schrödinger equation, $\hat{H}\Psi = E \cdot \Psi$, via exact diagonalization. The Hamiltonian, $\hat{H}$, of the system is:

$$\hat{H} = \sum_{i=1}^{N} \left[\frac{-\hbar^2}{2m_i^*} \Delta_i + V(\vec{x}) \right] + \hat{C}. \tag{5.1}$$

$\hat{C}$ is the Coulomb operator, which is given by:

$$\hat{C} = \frac{1}{4\pi\epsilon_0\epsilon_r} \sum_{i,\ j,\ i<j}^{N} \frac{c_i \cdot c_j}{|r_i - r_j|}. \tag{5.2}$$

The term $c_i = \pm e$ is the charge of a particle (electron or hole). As we are considering fermionic particles, the overall wavefunction is antisymmetric under particle exchange. Therefore, we consider $\hat{H}$ in a basis, $\{\Psi_{\mathbf{n}}\}$, of antisymmetrized Slater determinants:

$$\Psi_{\mathbf{n}} = \hat{\mathcal{A}} \prod_{i=1}^{N} \phi_{n_i}(x_i,\ \sigma_i). \tag{5.3}$$

The Slater determinants are constructed from the single-particle solutions, $\phi_{n_i}(x_i,\ \sigma_i)$, of Eq. 5.1. The index $\mathbf{n}$ represents the quantum numbers required to describe all particles. The asymmetrization operator, $\hat{\mathcal{A}}$, constructs a Slater determinant, which is asymmetric under the exchange of identical particles. To express $\hat{H}$ in the basis $\{\Psi_{\mathbf{n}}\}$, the matrix elements $\langle \Psi_{\mathbf{n}} | \hat{H} | \Psi_{\mathbf{m}} \rangle$ are computed. The Slater-Condon rules [265, 268] transform these multi-particle matrix elements into two-particle Coulomb matrix elements. The Slater-Condon rules for the two-particle Coulomb operator, $\hat{C}$, are:

$$\langle \Psi_{\mathbf{n}} | \hat{C} | \Psi_{\mathbf{n}} \rangle = \frac{1}{2} \sum_{i,\ j,\ i\neq j}^{N} \left[V_{ijij} - V_{ijji} \right] \tag{5.4}$$

$$\langle \Psi_{\mathbf{n}} | \hat{C} | \Psi_{\mathbf{n}(h,k)} \rangle = \sum_{i=1}^{N} \left[V_{hiki} - V_{hiik} \right] \tag{5.5}$$

$$\langle \Psi_{\mathbf{n}} | \hat{C} | \Psi_{\mathbf{n}(h,k,l,m)} \rangle = V_{hlkm} - V_{hlmk}. \tag{5.6}$$

The index $\mathbf{n}(h,k)$ indicates that this wavefunction is obtained from $\Psi_{\mathbf{n}}$ by replacing the single-particle wavefunction ϕ_h of particle number h by ϕ_k. The index $\mathbf{n}(h,k,l,m)$ means that two wavefunctions are changed correspondingly. The two-particle Coulomb matrix elements, V_{hklm}, are given by the following integral:

$$\begin{aligned} V_{hklm} &= \langle\phi_h\phi_k|\,\hat{C}\,|\phi_l\phi_m\rangle \\ &\equiv \frac{e^2}{4\pi\epsilon_0\epsilon_r}\int\int\frac{\phi_h(\mathbf{r}_1)^*\,\phi_k(\mathbf{r}_2)^*\,\phi_l(\mathbf{r}_2)\,\phi_m(\mathbf{r}_1)}{|\mathbf{r}_1-\mathbf{r}_2|}\,d\mathbf{r}_1\,d\mathbf{r}_2. \end{aligned} \tag{5.7}$$

Depending on the order of the indices, these integrals include the direct Coulomb and the Coulomb exchange terms. For a symmetric harmonic confinement potential, analytic solutions for the Coulomb integrals can be found e.g. in Refs. [71, 172].

The eigenfunctions of Eq. 5.1 are obtained by diagonalizing $\hat{H}$ in the basis $\{\Psi_\mathbf{n}\}$. The trion ground state has a small admixture of higher single-particle shells, which is the origin of the radiative Auger process. Upon optical recombination of one electron and a hole, the remaining electron of the trion is in a superposition including these higher shells. Detection of the frequency of the emitted photon projects the state of the remaining electron to the corresponding shell. For the trion, it is sufficient to carry out exact diagonalization for the initial state only since the final states are single-particle states.

In the dipole approximation, the emission spectrum can be computed with Fermi's golden rule [251, 269]:

$$I(\omega)\propto\sum_f|\langle\Psi^{(f)}|\,\hat{P}\,|\Psi^{(i)}\rangle|^2\cdot\delta(E_i-E_f-\hbar\omega)\cdot D(\omega), \tag{5.8}$$

where $\Psi^{(i)}$ is the initial state, $\Psi^{(f)}$ are the possible final states, and $D(\omega)$ is the density of states for an emitted photon. $\hat{P}=\sum d_{ij}\hat{h}_{i,\sigma}\hat{e}_{j,-\sigma}$ adds up all dipole-matrix (d_{ij}) allowed electron-hole recombinations, where i, j sum over orbital and σ over spin degrees of freedom [251, 269].

With the presented formalism, we estimate that the intensity of the radiative Auger transition from s- to the d_0-shell is about a hundred times weaker than the resonance fluorescence. However, this intensity is tendentially overestimated compared to the experimentally obtained values. The issue could be that the exact diagonalization only converges when taking into account very high single-particle shells. In reality, not all of these states exist due to close-by continuum states. Furthermore, the envelope wave approximation is a simplification compared to a fully atomistic treatment [270]. Finally, this approach assumes that angular momentum is a good quantum number, allowing radiative Auger with the d_0-shell but not with p-shells. In the experiment, radiative Auger with the p-shells is clearly observed, also in the limit of high magnetic field, suggesting

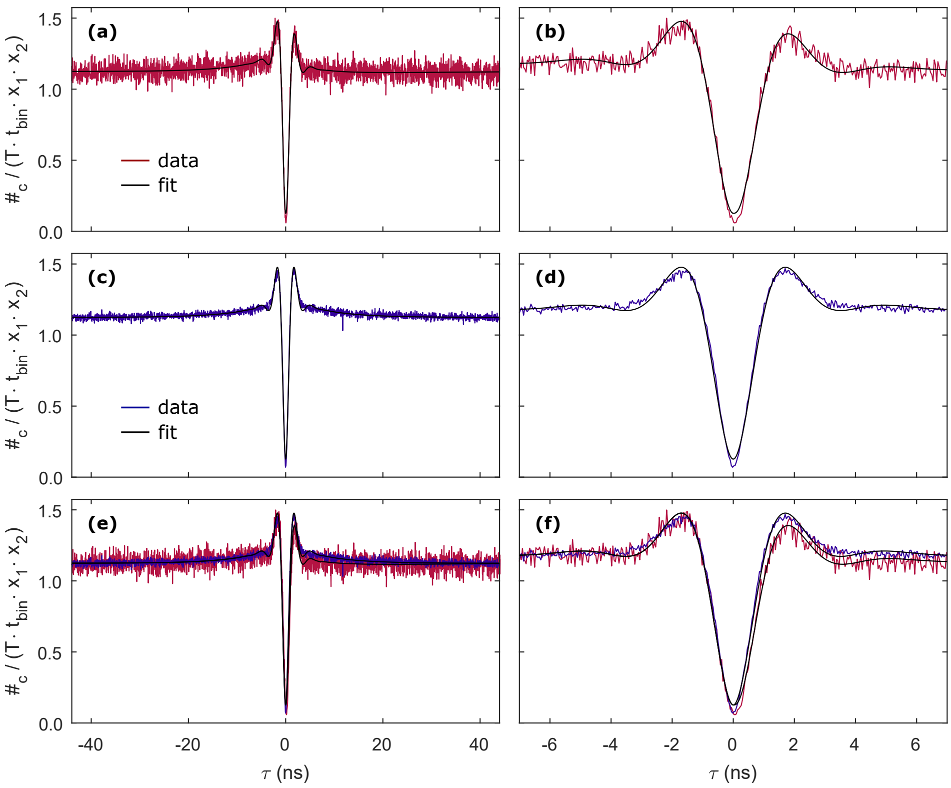

Fig. 5.5: Fits to the $g^{(2)}$-measurements shown in Fig. 5.3(c). Simultaneous fitting of Eqs. 5.12 and 5.13 to the corresponding auto- and cross-correlation data is performed. In the following sub-figures, the black lines correspond to the fit result. **(a)** Red line: cross-correlation measurement between resonance fluorescence and the radiative Auger emission where the second electron is transferred into the p_+-shell of the quantum dot. **(b)** Cross-correlation measurement from (a) on a shorter time-scale. **(c)** Blue line: auto-correlation measurement of the resonance fluorescence. **(d)** Auto-correlation measurement from (c) on a shorter time-scale. **(e)** Comparison of the auto- and the cross-correlation measurement together with the corresponding fits. **(f)** Comparison of the auto- and the cross-correlation measurement, plotted on a short time-scale.

that angular momentum is not a good quantum number.

5.6 Cross-Correlation: Theory

The $g^{(2)}$-measurements are modeled with the level scheme shown in Fig. 5.6. There are 4 different states which are taken into account for our simulation: the ground state, $|g\rangle$, with a single electron in the QD; the excited state, $|e\rangle$, a trion with two s-shell electrons;

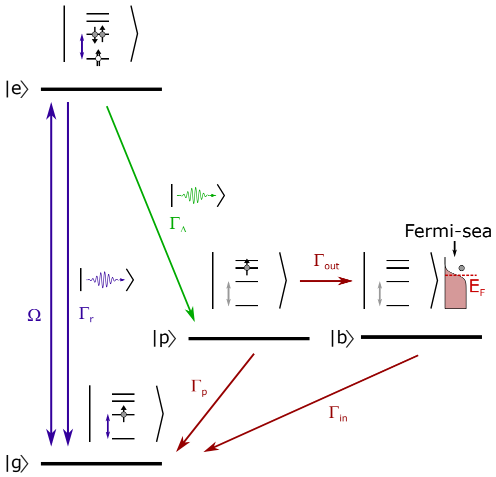

Fig. 5.6: Model used for the simulation of the auto-correlation measurement of the resonance fluorescence together with the cross-correlation between the resonance fluorescence and the radiative Auger emission.

the state after a radiative Auger emission, $|p\rangle$, where a single electron occupies the p-shell of the QD; and the ionized QD-state, $|b\rangle$, where the electron has tunneled out of the QD. We simulate the system by assuming the Hamiltonian ($\hbar = 1$):

$$\hat{H} = \frac{\Omega}{2} \left(|g\rangle \langle e| + |e\rangle \langle g| \right). \tag{5.9}$$

All decay channels are modeled following the scheme shown in Fig. 5.6. The Lindblad operator is:

$$\hat{\mathcal{L}} = \sqrt{\Gamma_r}\, |g\rangle \langle e| + \sqrt{\Gamma_A}\, |p\rangle \langle e| + \sqrt{\Gamma_p}\, |g\rangle \langle p| \tag{5.10}$$

$$+ \sqrt{\Gamma_{\text{out}}}\, |b\rangle \langle p| + \sqrt{\Gamma_{\text{in}}}\, |g\rangle \langle b|. \tag{5.11}$$

We compute the steady-state density matrix, ρ_s, and obtain the auto- and cross-correlation by using the Quantum Toolbox in Python (QuTiP [271]). The operator for the resonant decay is $\hat{a} = \sqrt{\Gamma_r}\, |g\rangle \langle e|$, and the operator for the radiative Auger decay is $\hat{a}_A = \sqrt{\Gamma_A}\, |p\rangle \langle e|$. Auto- and cross-correlations are computed numerically by applying the quantum regression theorem. The auto-correlation of the resonance fluorescence is given by:

$$g^{(2)}(\tau) = \frac{\langle \hat{a}^\dagger(t) \hat{a}^\dagger(t+\tau) \hat{a}(t+\tau) \hat{a}(t) \rangle}{\langle \hat{a}^\dagger(t) \hat{a}(t) \rangle^2}. \tag{5.12}$$

Ω	Γ_r	Γ_A	Γ_p	Γ_{out}	Γ_{in}	t_{bl} (ns)
1.85	1.22	0.001	11.7	0.82	0.07	7.2

Table 5.3: Parameters obtained from simultaneously fitting the auto- and cross-correlation measurements shown in Fig. 5.5. The radiative decay rate, Γ_r, is obtained from a different measurement and is not included in the fit. The parameters associated to blinking and laser background are: $c_0 = 1.143$, $c_1 = 0.153$, $c_l = 0.126$. Γ_A is estimated from the intensity ratio between radiative Auger emission and resonance fluorescence and is also not included in the fit. Unless otherwise stated, all parameters are given in GHz.

The cross-correlation is given by:

$$g^{(2)}(\tau) = \frac{\langle \hat{a}_A^\dagger(t)\hat{a}^\dagger(t+\tau)\hat{a}(t+\tau)\hat{a}_A(t)\rangle}{\langle \hat{a}^\dagger(t)\hat{a}(t)\rangle\langle \hat{a}_A^\dagger(t)\hat{a}_A(t)\rangle}. \tag{5.13}$$

The auto-correlation of the radiative Auger emission is:

$$g^{(2)}(\tau) = \frac{\langle \hat{a}_A^\dagger(t)\hat{a}_A^\dagger(t+\tau)\hat{a}_A(t+\tau)\hat{a}_A(t)\rangle}{\langle \hat{a}_A^\dagger(t)\hat{a}_A(t)\rangle^2}. \tag{5.14}$$

We multiply the result of this simulation by $1 + c_1 \cdot \exp(-|\tau|/t_{bl})$ to take into account a weak blinking on short time-scales [88], which might be caused by electron spin pumping enabled by a weak nuclear magnetic field [272]. Additionally, the model function is multiplied with a global prefactor c_0, which takes into account a weak blinking on a time-scale of ~ 0.1 ms, probably caused by charge noise. For the resonance fluorescence, a small fraction c_l of reflected laser in the resonant emission is taken into account via $g^{(2)} \to g^{(2)} \cdot (1 - c_l) + c_l$. We perform a simultaneous fit of this model to the auto-correlation of the resonance fluorescence and the cross-correlation between the resonance fluorescence and the radiative Auger emission. The result of this fit is shown in Fig. 5.5. The obtained fit parameters are stated in Tab. 5.3. These parameters also give a good fit to the auto-correlation of the radiative Auger emission, which is shown in Fig. 5.3(g). All fit parameters are kept the same, and only the Rabi-frequency is increased ($\Omega_{\text{R}} = 5.4$ GHz), taking into account that the auto-correlation of the radiative Auger emission has been measured at higher power.

5.7 Evaluation of Correlation Measurements

All $g^{(2)}$-measurements are performed in a time-tagged, time-resolved mode. The arrival times of all photons are recorded over the full integration time, T, on two single-photon detectors. Any analysis is carried out post-measurement. We compute the cross-correlation ($g^{(2)}$) between both signals by counting the coincidence events between the two detectors as a function of a time delay, τ, between the signals.

Let x_1, x_2 be the count rates on detectors 1 and 2, respectively. We divide the full integration time into time-intervals of length, t_{bin}. The value for t_{bin} is chosen to be small enough such that the probability of a photon in the corresponding time-interval is very small: $t_{bin} \cdot x_{1/2} \ll 1$. For each detector, we determine the number of detection events in every small time interval. This number is either 0 for no photon or 1 for one photon since the probability of having more than one photon in an interval is negligibly small (for $t_{bin} \cdot x_{1/2} \ll 1$). When there is one detection event on detector 1 in an interval at time t and another detection event on detector 2 in an interval at time $t + \tau$, we call it a coincidence event for time delay τ. For different time delays, we count the number of coincidence events, $\#_c$, over the full integration time. The cross-correlation between both detectors is obtained by dividing $\#_c(\tau)$ by its expectation value for the case of two uncorrelated detection channels: $\langle \#_c \rangle = T \cdot t_{bin} \cdot x_1 \cdot x_2$. This expression for $\langle \#_c \rangle$ is obtained by the following consideration: the probability of finding a detection event in a certain time interval is $t_{bin} \cdot x_1$ and $t_{bin} \cdot x_2$. If both detection channels are uncorrelated, the probability of finding a detection event for the first detector at time t and a detection event for the second detector in the time-interval at $t + \tau$ is $p_c = t_{bin}^2 \cdot x_1 \cdot x_2$. For $T \gg \tau$, the probability density distribution of $\#_c$ is thus a binomial distribution:

$$P(\#_c) = \binom{T/t_{bin}}{\#_c} \cdot (1 - p_c)^{T/t_{bin} - \#_c} \cdot p_c^{\#_c} \tag{5.15}$$

The expectation value of this distribution is the corresponding normalization factor: $\langle \#_c \rangle = T \cdot t_{bin} \cdot x_1 \cdot x_2$.

5.8 Power Dependent Excitation

We measure the intensity of the radiative Auger emission as a function of resonant excitation power and laser detuning. This measurement is shown in Fig. 5.7. In a first measurement, we keep the narrow-band laser at a fixed frequency and sweep the detuning between trion transition and laser by applying a gate voltage, V_g. The gate voltage shifts

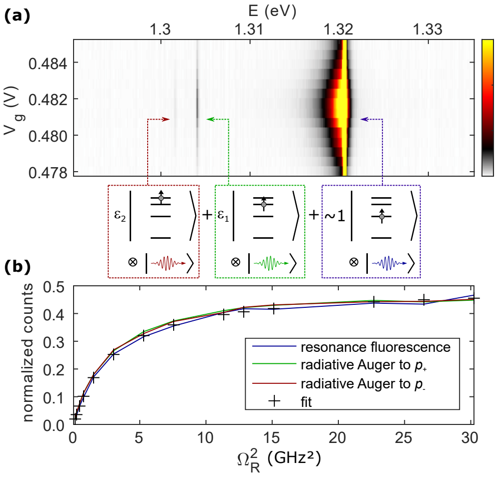

Fig. 5.7: **(a)** Resonance fluorescence and radiative Auger emission. The excitation laser is fixed ($E \simeq 1.321$ meV), and the QD is swept through the resonance by tuning the gate voltage, V_g. **(b)** Dependence of resonance fluorescence and radiative Auger emission on the power of the resonant laser. For the power dependence, the laser is kept on resonance with the trion (X^{1-}). When normalized, the resonance fluorescence and the radiative Auger emission intensity depend equally on the excitation power. Both are proportional to the upper state occupation of a resonantly driven two-level system (Eq. 5.16).

the trion energy via the quantum-confined Stark effect. The intensity and the energy of the emission are recorded on a spectrometer. This measurement is shown in Fig. 5.7(a). When laser and trion energy are on resonance, there is a bright emission at ~ 1.321 eV, the resonance fluorescence. This emission is spectrally asymmetric due to the LA-phonon sideband around the resonant peak. At lower energy, ~ 18 meV below the resonance fluorescence, there is the emission corresponding to the radiative Auger excitation into the p-shells. This emission is strongest when also the resonance fluorescence is at its maximum, indicating that the intensity of the radiative Auger emission is proportional to the excited state population of the QD. Our model of the radiative Auger process implies this proportionality since the process only takes place in the excited state (trion) of the QD.

To investigate this dependence further, we keep the laser on resonance with the trion and measure the emission intensities as a function of power. This measurement is shown in Fig. 5.7(b). The power dependence of the resonance fluorescence and the radiative Auger emission follows the power saturation curve of a two-level system very well. This result also confirms that the radiative Auger process is entirely related to the trion. Its

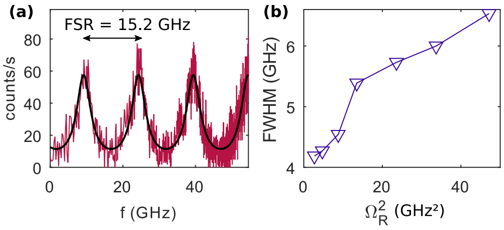

Fig. 5.8: **(a)** Radiative Auger emission at $\Omega_R = 0.73$ GHz transmitted trough a 0.41 GHz Fabry-Perot cavity. **(b)** Linewidth of the radiative Auger emission as a function of the resonant Rabi frequency.

rate is proportional to the trion occupation, ρ_{22}, under resonant excitation [273]:

$$\rho_{22} = \frac{1}{2}\frac{\Omega_{\mathrm{R}}^2}{2\Gamma_r^2 + \Omega_{\mathrm{R}}^2}. \tag{5.16}$$

We expect that the ratio of the radiative Auger and the resonance fluorescence intensities roughly reflects the ratio Γ_A/Γ_r. This way, we estimate the value for Γ_A to be on the order of ~ 1 MHz.

Finally, we measure the linewidth of the radiative Auger emission. We pass the emission through a Fabry-Perot cavity (15.2 GHz free spectral range, 0.41 GHz linewidth) and sweep the cavity length. The result of this measurement on the p_+-emission is shown in Fig. 5.8(a). We determine the linewidth of the radiative Auger emission by fitting a multi-Lorentzian which is convoluted with the cavity linewidth. At low power, we measure a minimum linewidth of 4.19 GHz. For comparison, the lifetime limited linewidth is estimated by the decay rate of the p_+-state after the radiative Auger process: $\frac{\Gamma_r}{2\pi} = 1.99$ GHz. We repeat the linewidth measurement for different excitation Rabi frequencies. This measurement is shown in Fig. 5.8(b) and shows a linear increase of the linewidth as a function of the excitation power. The reason for the additional contribution to the linewidth and its linear broadening with the excitation power requires further investigations.

5.9 Spin Pumping and Rabi Oscillations

Fig. 5.9(a) shows a measurement of the resonance fluorescence of the negative trion as a function of the gate voltage and the laser wavelength. This measurement is performed on the quantum dot which is presented in Fig. 5.1(b). The trion is stable in the gate voltage range between $V_g = -0.52$ V and $V_g = -0.48$ V. This charge plateau splits

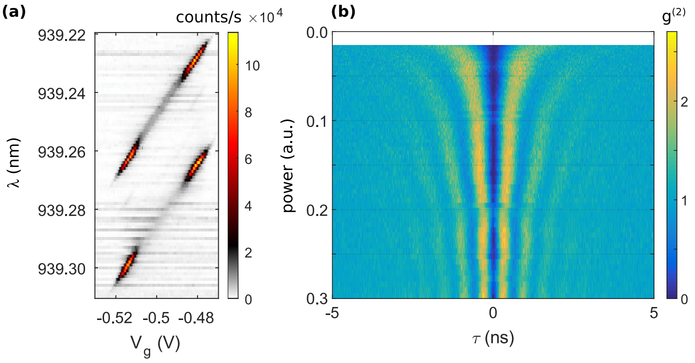

Fig. 5.9: **(a)** The charge plateau of the resonantly excited trion at a magnetic field of 0.6 T. This measurement is carried out on the InGaAs quantum dot (QD) shown in Fig. 5.1(b). At the edges of the charge plateau, a strong resonance fluorescence is detected. In the plateau center, the resonance fluorescence intensity is strongly reduced due to electron spin pumping. All radiative Auger measurements are performed at the plateau edges. **(b)** Power dependent $g^{(2)}$-measurement on the negative trion of the same QD.

into two due to the electron spin Zeeman energy. We perform the measurements of the radiative Auger emission on one Zeeman branch. No Zeeman splitting is observed in the emission spectrum, which shows that the radiative Auger process is spin-conserving. In the center of the charge plateau, the resonance fluorescence disappears due to optical spin pumping. At the edges of the charge plateau, the resonance fluorescence is strong due to spin co-tunneling with the back gate [23, 112]. For this reason, we perform all measurements in the co-tunneling regime.

Fig. 5.9(b) shows resonantly driven Rabi-oscillations as a function of the excitation power. The measurement is performed on the trion state of the same QD. These coherent oscillations in the auto-correlation ($g^{(2)}$) measurement show that the QD can be approximately described by a two-level system [82]. However, radiative Auger is a fundamental process that limits this two-level approximation in the case of a trion.

Chapter 6

Conclusions and Outlook

Self-assembled quantum dots (QDs) are useful as single-photon sources [13, 20] and for quantum optics experiments in the solid-state [60]. They are also promising for interfacing other quantum systems which only weakly couple to light – e.g., mechanical resonators [274, 275] or gate-defined quantum dots [54, 55, 58]. For such applications, the rate of the photon stream emitted by the quantum dot is an important figure of merit. To boost this rate, cavities and nanobeam waveguides can be used [10]. However, especially nanostructuring can be problematic since interfaces close to the QD cause charge noise, and charge-control of the QD is difficult to implement.

The issue of charge noise in nanostructures motivated the development of a new *p*-*i*-*n*-*i*-*n*-diode structure for hosting the QDs (Chapter 2). The developed diode-structure has been successfully used for electron-spin experiments in nanostructured devices [34, 107, 120]. In these nanostructures, QDs can be operated at close-to-zero bias voltage and low tunneling current, which has been an issue before [97]. For future experiments, hole-spins might have advantages due to their reduced interaction with nuclear spins [17, 46]. However, the deterministic charging of QDs with holes requires a tunnel coupling to a *p*-doped layer. A problem is that growing QDs above layers with carbon *p*-doping tends to degrade their optical properties [125]. Therefore, the *p*-*i*-*n*-*i*-QD-*i*-*n* concept cannot be directly transferred to a *p*-*i*-QD-*i*-*p*-*i*-*n* diode where the QDs are tunnel-coupled to a Fermi-sea of holes. Alternatives might be using meta-stable hole states [276] where there is an extra AlGaAs-barrier above the QDs or a *p*-*i*-*n* diode where the QDs are grown close to a *p*-doped top gate.

InGaAs QDs are surrounded by a two-dimensional wetting layer which strongly hybridizes with highly charged excitons in the QD. Chapter 3 shows that the wetting layer states in the conduction band can be removed by a slight modification to the QD-growth. As a result, highly charged excitons have much better spectral properties in comparison to conventional InGaAs QDs [79, 151]. This improvement is useful for implementing multi-carrier qubits in QD-molecules [144]. Theoretical results indicate that for the new

QDs, non-resonant absorption [140] and cavity feeding [147] could be reduced. An experimental investigation is missing so far. A simple experiment would be measuring the QD-luminescence as a function of the energy of a blue-detuned excitation laser. For conventional QDs, such photoluminescence excitation (PLE) experiments show a clear absorption background that increases towards the wetting layer energy [139]. The wetting-layer free QDs could also be interesting for studying multi-carrier effects in the solid-state. In this work, evidence for an intra-QD Auger process has been found for the triply charged exciton.

For a different type of QDs, consisting of GaAs in AlGaAs, a correlation between their optical properties and their Voronoi-cell areas is presented in Chapter 4. This result shows that the capture zone model applies very well to the growth of these QDs. It also shows that there is a strong material diffusion in the initial part of the QD-growth. The found correlations imply that site-control would narrow the QD-ensemble spectrally. A GaAs QD in AlGaAs is a promising system for application as a single-photon source which is frequency-matched to an atomic rubidium memory [88, 194]. Compared to InGaAs QDs, the GaAs QDs might have prolonged spin dephasing times due to their larger size and the reduced nuclear spin number. However, charge control of such QDs has been barely implemented so far, and narrow linewidths under resonant excitation have not been demonstrated in previous work [277, 278]. The main difficulty is that the doping of AlGaAs is not easy to realize due to the formation of DX-centers [279, 280]. In very recent work, we have demonstrated ultra-low noise and charge-control for GaAs QDs in a novel diode structure [281]. This achievement was crucial for the results presented in Chapter 5 and significantly improves the prospects for quantum optics [60, 282] and spin-experiments [51] with GaAs QDs.

Finally, it is shown that radiative Auger-processes within a QD can take place even for just three confined carriers (a trion) and under resonant excitation (Chapter 5). Upon optical recombination, the second electron of the trion is promoted to a higher shell. The emitted photon is correspondingly red-shifted. Especially interesting about the radiative Auger-process is that it is not limited to a single type of emitter. It is demonstrated here that this process takes place for both types of QDs presented before. The process arises due to the Coulomb interaction between charge carriers and the fact that optical recombination abruptly changes the eigenstates for the remaining carriers. In this work, the radiative Auger-process has been studied for the conduction band. It would also be interesting to investigate this process in the valence band of a QD. Similar to other weak processes [283, 284], the radiative Auger-process can potentially be enhanced with an optical microcavity [60, 282]. Radiative Auger has two powerful applications: it can be used to directly probe the single-particle spectrum of a QD, which is difficult to achieve by other optical techniques. Furthermore, the photon statistics of the radiative Auger emission reveals information about the relaxation of a single confined carrier.

Chapter 7

Acknowledgment

First of all, I would like to thank my parents and my two brothers Daniel and Sebastian for their support during my time as a PhD-student. I thank my supervisor Richard J. Warburton for giving me the great opportunity to work in his group and for his enormous support. I thank him for many discussions from which I have learned a lot about semiconductor quantum dots and physics in general. I thank Immo Söllner for great supervision as my postdoc during the first years of my PhD and for many discussions which significantly influenced my understanding of physics. In this context, I would also like to thank Jonas G. Roch, Martino Poggio, Lukas Sponfeldner, and especially Alisa Javadi for discussions about experimental and theoretical topics. I would like to thank Liang Zhai, Daniel Najer, and Clemens Spinnler for discussions and excellent teamwork on several projects. I would like to thank Arne Ludwig, Andreas D. Wieck, Armando Rastelli, and their groups, in particular also Rüdiger Schott and Sven Scholz, for providing the samples used in this work. Additionally, I would like to thank Arne Ludwig for many stimulating discussions about quantum dot growth. I also thank Peter Lodahl and his group, in particular Leonardo Midolo, Martin Hayhurst Appel, and Ravitej Uppu, for various conversations about recent projects and for providing nanostructured samples. I also would like to thank Clemens Spinnler, Natasha Tomm, Sigurd Flågan, Liang Zhai, and Alisa Javadi for carefully reading parts of this thesis. Finally, I thank all the people from our group for a very good team spirit and a nice working atmosphere.

Chapter 8

Appendix

8.1 Solving the Schrödinger Equation Numerically

Numerical solutions of the Schrödinger equation have been used in this work, in particular in section 3. In this section, two numerical methods to solve the Schrödinger equation are explained. Both methods translate the Schrödinger equation (a differential equation) into a system of linear equations. This set of equations is obtained by sampling the searched wavefunction at discrete points and approximating its derivatives by finite differences. Both methods are not restricted to the Schrödinger equation but can be applied to other differential equations. It depends on the particular context which of the two methods is more convenient to use.

The time-independent Schrödinger equation is:

$$\left(-\frac{\hbar^2}{2m^*}\Delta + V(\vec{x})\right)|\Psi(\vec{x})\rangle = E\,|\Psi(\vec{x})\rangle\,, \tag{8.1}$$

where $|\Psi(\vec{x})\rangle$ is the wavefunction of a particle with effective mass m^* and energy E in a potential $V(\vec{x})$.

We sample $|\Psi(\vec{x})\rangle$ at discrete points separated by a sufficiently small distance d. The second derivative $\frac{\partial\Psi}{\partial x^2}$ can be approximated by:

$$\frac{\Psi_{i+1} - 2\Psi_i + \Psi_{i-1}}{d^2}, \tag{8.2}$$

where the sampling points $\Psi_i = \Psi(x_i)$ and $\Psi_{i\pm1} = \Psi(x_i \pm d)$ have the distance d. Applying this relation for the derivatives along all three dimensions yields:

$$\begin{aligned}&-\frac{\hbar^2}{2m^*}\frac{1}{d^2}\left(-6\Psi_{i_x,i_y,i_z} + \Psi_{i_x+1,i_y,i_z} + \Psi_{i_x-1,i_y,i_z} + \Psi_{i_x,i_y+1,i_z} + \Psi_{i_x,i_y-1,i_z} + \Psi_{i_x,i_y,i_z+1} + \Psi_{i_x,i_y,i_z-1}\right)\\ &+V_{i_x,i_y,i_z}\Psi_{i_x,i_y,i_z} = E\cdot\Psi_{i_x,i_y,i_z},\ \text{with } i_x, i_y, i_z \in \mathbb{N}.\end{aligned} \tag{8.3}$$

Ψ_{i_x,i_y,i_z} and V_{i_x,i_y,i_z} are discrete sampling points of the wavefunction $\Psi(\vec{x})$ and the potential $V(\vec{x})$ at the positions $\vec{x}_{i_x,i_y,i_z} = d \cdot (i_x, i_y, i_z)^T$. Eq. 8.3 defines a set of linear equations. For simplicity, the one-dimensional version of Eq. 8.3 is considered in the following:

$$-\frac{\hbar^2}{2m^*}\frac{1}{d^2}\left(\Psi_{i+1} - 2\Psi_i + \Psi_{i-1}\right) + V_i\Psi_i = E \cdot \Psi_i, i \in \mathbb{N}. \tag{8.4}$$

8.1.1 Method 1: Transferring the Differential Equation into an Eigenvector Problem

Eq. 8.4 is an eigenvector problem for the vector $(\Psi_1, \Psi_2, ..., \Psi_N)^T$ composed of the wavefunction values Ψ_i at discrete sampling points. This becomes clear when putting Eq. 8.4 in a matrix form:

$$\left(\frac{\hbar^2}{2m^*}\frac{1}{d^2}\begin{bmatrix} 2 & -1 & & & \\ -1 & 2 & -1 & & \\ & \ddots & \ddots & \ddots & \\ & & -1 & 2 & -1 \end{bmatrix} + \begin{bmatrix} V_1 & & & \\ & V_2 & & \\ & & \ddots & \\ & & & V_N \end{bmatrix}\right) \cdot \begin{bmatrix} \Psi_1 \\ \Psi_2 \\ \vdots \\ \Psi_N \end{bmatrix} = E \cdot \begin{bmatrix} \Psi_1 \\ \Psi_2 \\ \vdots \\ \Psi_N \end{bmatrix} \tag{8.5}$$

The corresponding eigenfunctions are obtained as an eigenvector sampling the actual wavefunction at discrete points $(\Psi_1, \Psi_2, ..., \Psi_N)_n^T$; the eigenenergies are $E = E_n$. A similar expression compared to Eq. 8.5 can be found for the two- or three-dimensional case and requires a practical definition for ordering all sampling points.

To check the numerical implementation, results are compared to analytical solutions of the Schrödinger equation. In Fig. 8.1 this is carried out for a two-dimensional harmonic oscillator with confining potential $V(r) = \frac{1}{2}m_e^*\omega_0^2 r^2$ (see Ref. [45]). An analytical expression of the wavefunctions is given by Eq. 3.3, with $E_{n,L} = (2n + |L_z| + 1)\,\hbar\omega_1 - \frac{1}{2}L_z\hbar\omega_c$ being the corresponding eigenenergies.

The normalized numerically and analytically obtained wavefunctions coincide, as shown in Fig. 8.1(c). The eigenenergies coincide as well. For the chosen mesh (distance $d = 1$ nm between the sampling points), the eigenenergies of the first 30 states (lowest energy) agree with the analytic solution within 1%.

8.1.2 Method 2: Step from (Ψ_i, Ψ_{i+1}) to Ψ_{i+2}

One way of numerically solving Eq. 8.1 has been presented in the previous section. There are cases where the equation has to be solved differently: when computing the wavefunction overlap between a continuum state and a discrete state, for instance (Ref.

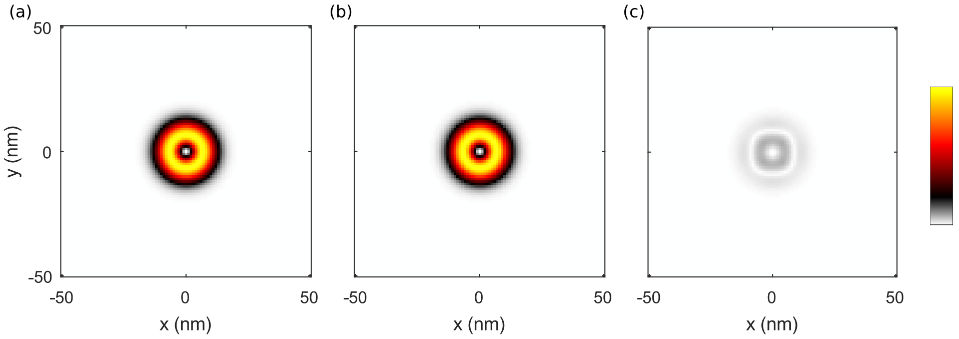

Fig. 8.1: (a) Probability density of the first excited state of a symmetric harmonic oscillator obtained by numerically solving the Schrödinger equation. The used parameters are: $\hbar\omega_0 = 25$ meV, $m^* = 0.067m_0$, $B = 0$ T. For the numerical computation, a mesh with $d = 1$ nm resolution is used. (b) Analytical solution of the probability density of the first excited state for a symmetric harmonic oscillator. (c) The absolute value of the difference between the numerical and the analytical solutions multiplied by a factor of 10. The numerical result has a maximum deviation from the exact solution by less than 1%.

[45]). For unbound particles, there is a solution to the Schrödinger equation for an arbitrary energy E of the particle. A set of discrete energy values E_n, as it results when solving Eq. 8.4, does not make sense. Instead, one would like to obtain a solution of the Schrödinger equation for an arbitrary (given) energy E. This can be done as follows: First, start with the two first points Ψ_1, Ψ_2 of the wavefunction, and set them to two values. In case Ψ_1, Ψ_2 are located in a potential-barrier where the wavefunction decays to zero, a good choice for the starting points is $\Psi_1 = 0$, $\Psi_2 = 1$. Eq. 8.4 can now be used to find iteratively the following sampling points of the wavefunction because based on the values Ψ_i, Ψ_{i+1} it uniquely determines the value of Ψ_{i+2}.

Again, the method is tested by comparing it to an analytical solution of the wavefunction. The analytical wavefunction of the Schrödinger equation for a given energy E in case of a potential $V(x) = \alpha \cdot x$ is given by the following expression [285]:

$$Ai\left(\left(\frac{2m_e^*}{\hbar^2 e^2 F^2}\right)^{1/3} \cdot (eFx - E)\right), \tag{8.6}$$

where $Ai(x)$ is an Airy function and F the electric field. Shown in Fig. 8.2 is a comparison between this analytical and a numerical solution. For the electron effective mass, $m^* = 0.067m_e$ is assumed; the electric field is chosen to be 40 kV/cm. For a mesh resolution of $d = 0.1$ nm, the numerical solution deviates from the analytical one by less than 1% over the depicted range.

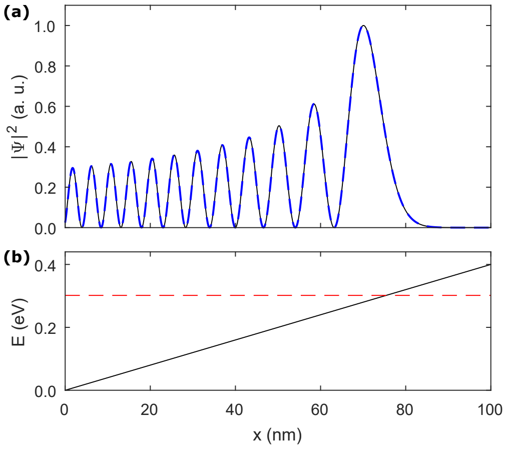

Fig. 8.2: (a) Analytical and numerical solutions of the Schrödinger equation in an electric field. The electron effective mass is assumed to be $m_e^* = 0.067m_0$. For the numerical solution a mesh resolution of $d = 0.1$ nm is assumed. (b) Solid black line: potential corresponding to a static electric field of 40 kV/cm. Dashed red line: energy of the wavefunction shown in (a).

Note that a modification of the described method can also be used to compute eigenenergies E_n in a case where the particle is fully confined [286].

How accurate a numerical solution is in comparison to the precise (analytical) solution is discussed in Ref. [286]. Generally, one must distinguish between accuracy in determining the eigenenergies E_n and the wavefunctions. According to Ref. [286], method 1 is better suited to determine wavefunctions, and a modification of method 2 is more accurate regarding the eigenenergies. There are two methods to make sure that numerically obtained eigenfunctions and eigenenergies are accurate: first, making a convergence test by decreasing the distance d between two sampling points (mesh size). With decreasing d the numerically obtained derivatives are more accurate. And second, checking the numerical routine by comparing its results to analytical solutions of specific problems.

8.2 Time-Resolved Measurements

8.2.1 Superconducting Single-Photon Detectors

Superconducting single-photon detectors (SSPDs) [288, 289] combine close-to unity detection efficiency with ultra-fast timing resolution. The SSPDs used in this work are based on superconducting Nb(Ti)N-nanowires with a meander geometry [289, 290, 291, 292]. The timing resolution of a single detector is < 20 ps (full width at half maximum).

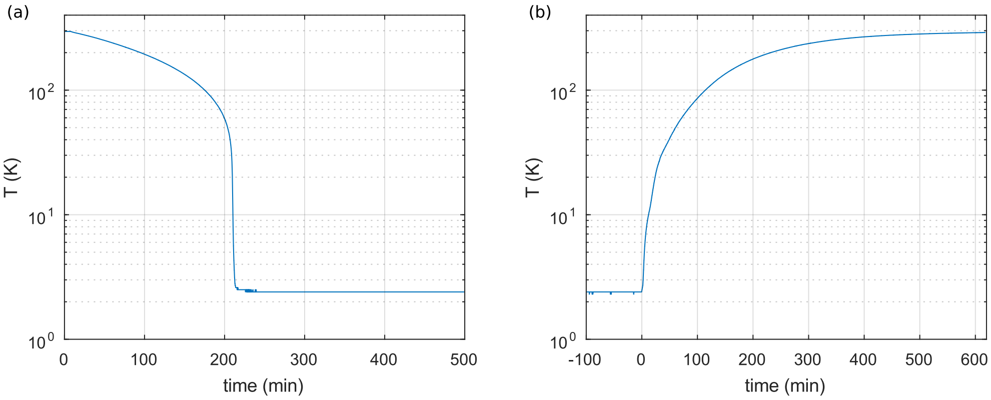

Fig. 8.3: (a) Cooldown: Temperature of the SSPD-cryostat as a function of time. The compressor is started at time $t = 0$. The SSPDs reach a base temperature of 2.4 K after the compressor system is running for ~ 250 minutes. (b) Warm-up of the SSPD-cryostat. After stopping the compressor system, the SSPDs reach room temperature after ~ 500 minutes.

The detection efficiency is optimized for $\lambda = 950$ nm reaching $\sim 80\%$ at this wavelength. The dark-count rate of the detector can be kept close-to-zero without reducing the detection efficiency. A brief description of the working principle of an SSPD is given in the following.

The Nb(Ti)N-meander-nanowire is kept below its critical temperature T_{c} so that it is superconducting. It is biased with a current below, but close to its critical current. A single photon impinging on the meander-nanowire provides the energy to break its superconductivity locally. Consequently, a finite voltage drop over the meander-nanowire is detected [287]. The corresponding voltage signal is pre-amplified spatially close to the meander-nanowire (in-cryo amplifier). The in-cryo amplification is important to reduce the contribution of electrical noise to the inaccuracy of measuring the arrival time of the photon (timing jitter). The signal is additionally amplified outside of the cryostat and is forwarded to a time tagger (PicoHarp 300), which measures the arrival time of the signal and records it on a hard-drive of a connected computer. The arrival time of the electrical signal corresponds to the arrival time of the initial photon plus an ideally constant delay. This setup allows for photon correlation measurements (e.g. the second-order auto-correlation function, $g^{(2)}$).

Daily operation of the SSPD-system: in a first step, the SSPD-system has to be cooled down below T_{c}. Therefore, the SSPD-chamber has to be evacuated ($< 5 \times 10^{-5}$ mbar) at room temperature. Afterwards, the cooldown is started by turning on a compressor-cycle connected to the cryostat. The cooldown can be monitored with software provided by

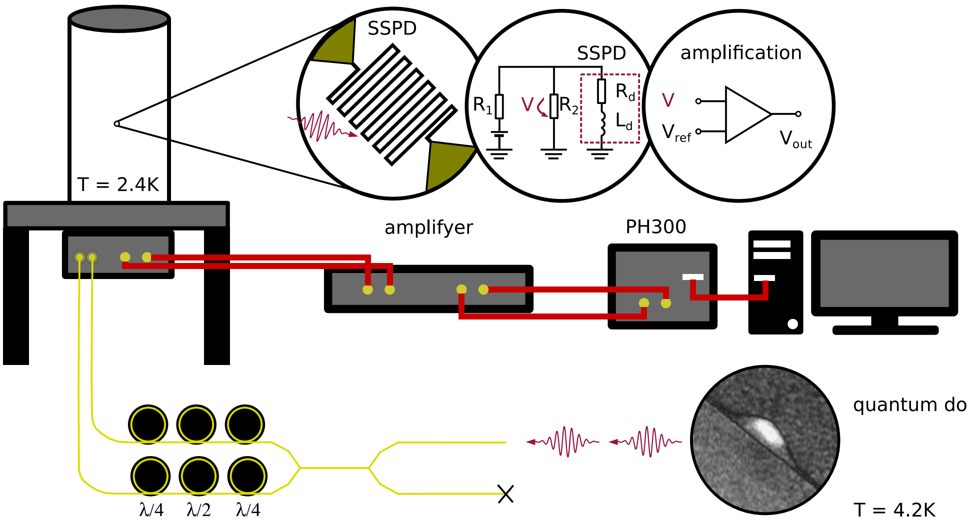

Fig. 8.4: Setup for time-resolved measurements using the superconducting single-photon detectors (SSPDs). The optical emission from a QD is split by a fiber beam-splitter and sent to two SSPDs. The SSPDs are operated at $T = 2.4$ K and biased close to the critical currents. Since the detectors are operated close to the critical current, a single photon impinging on the meander-nanowire breaks its superconductivity. When this happens, there is a finite voltage drop over a resistor, R_2, which is in parallel with the meander-nanowire. To reduce the electronic noise, the voltage is pre-amplified inside of the cryostat hosting the SSPDs. It is amplified another time outside of the cryostat. All signal arrival times are recorded (PicoHarp 300), and a time-dependent correlation of the signals can be computed. Figure partly taken from Refs. [12, 287]

the manufacturer (Single Quantum). A typical dependence of temperature as a function of time is shown in Fig 8.3. After the compressor system is running for ~ 3 h the SSPD-chamber reaches its base temperature of ~ 2.4 K. The detector can be used once this temperature is reached.

The detector performance depends on its bias current. A corresponding measurement is shown in Fig. 8.5 with and without a photon flux on the detectors. The first detector has a critical current of $I_c \simeq 15\ \mu$A the second one has a larger critical current $I_c \simeq 50\ \mu$A. For single-photon detection, each detector should be operated below, but close to its critical current. Too far below the critical current, the detection efficiency is low because a single photon provides barely enough energy to break the superconductivity of the nanowire. Operated too close to its critical current, the dark count rate increases, and the superconductivity sometimes breaks spontaneously for even longer times (latching [290]). Between these two regimes, the detection efficiency has a plateau where the

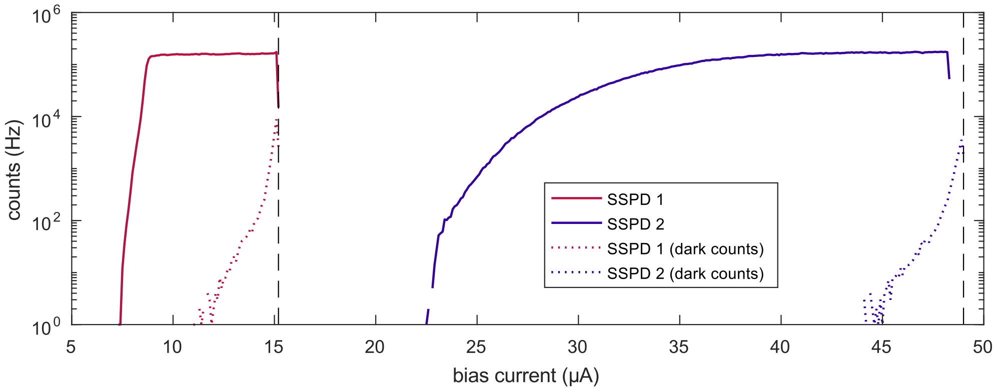

Fig. 8.5: The detector countrate as a function of the applied bias current. The first detector measures the incoming photons with an approximately constant efficiency for a bias current of $8 - 14$ μA (solid red curve). Above 10 μA, the detector starts showing dark counts. Above its critical current of $I_\mathrm{c} \simeq 15$ μA, the superconductivity is, independent of the light exposure, permanently broken – the detector switches off. A good choice for the bias current of the first detector is ~ 10 μA. Here, the dark counts are minimized without significantly reducing the detection efficiency. The second detector (blue curves) has a significantly higher critical current of $I_\mathrm{c} \simeq 49$ μA. A good operating bias is ~ 40 μA.

system can be operated for single-photon detection. The bias current of the detector also has a small influence on the timing jitter: for a higher bias current, the voltage when the superconductivity breaks is higher, which reduces the contribution of electrical noise on the timing jitter. These properties of the detector should be taken into account before measurement and can be slightly adjusted by changing the bias current of the detector.

Calibration of the detection efficiency requires measuring powers very accurately. Such a measurement has not been done here. Instead, Fig. 8.6(a) shows a comparison of the countrate of a fiber-coupled APD (SPCM-NIR, excellitas) with the SSPDs. In both cases, the same photon source has been used. The APD has a specified detection efficiency of 28.7% at $\lambda = 950$ nm which implies a detection efficiency of $\eta > 60\%$ for the SSPDs. Note that the used APD has a detection efficiency that varies with time when a non-angled (PC) fiber is coupled to it. The reason is possibly an interference effect in combination with heating of the APD-device. This issue disappears when a fiber with angled physical contact is coupled to the APD, yet the overall detection efficiency is lower in this case. For these reasons, the comparison between APD and SSPD is only a rough estimation of the SSPD detection efficiency.

Shown in Fig. 8.6(b) is an instrument response function which is used for an estimation of the timing jitter of an SSPD. For this measurement, a pulsed laser is attenuated and

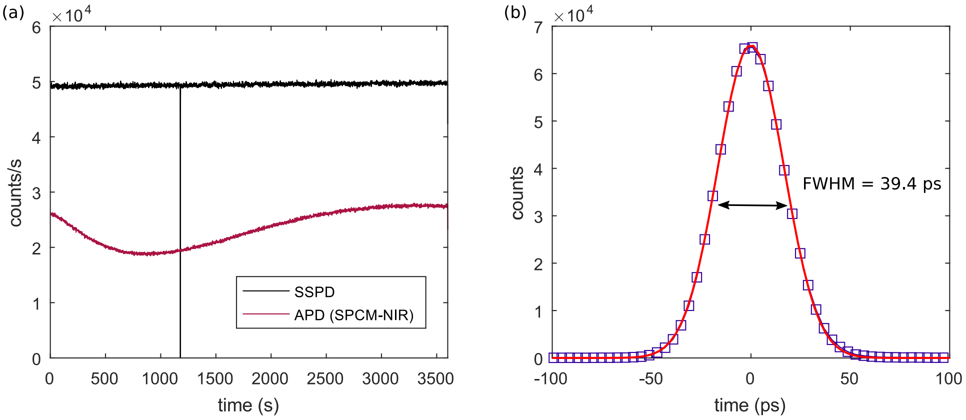

Fig. 8.6: (a) Comparison between the detection efficiency of an APD (SPCM-NIR), red curve, and an SSPD, black curve. After the APD is turned on, its detection efficiency fluctuates over time, probably related to heating of the APD-device. The detection efficiency of the SSPD is significantly higher. Between $t = 1000$ s and $t = 1500$ s, there is an event where the SSPD shuts off for about a second. It is probably caused by electrical noise when the air conditioning switches on. (b) The instrument response function measured for detector 1 has a full width at half maximum of 39.4 ps. The measurement includes the timing jitter of the used time tagger, $\sim$ 28 ps, and the pulse width of the used laser.

sent to an SSPD. The trigger signal of the laser is sent to the first channel of a time tagger (PicoHarp 300), the signal from the SSPD to its second channel. The measured full width at half maximum is 39.4 ps for detector 1 and 35.6 ps for detector 2. Both values are obtained by Gaussian fitting. Note that these numbers include the timing jitter of the used time tagger (PicoHarp 300, $\sim$ 28 ps) and a finite width of the used laser pulse $\sim$ 20 ps. If a Gaussian distribution is assumed for the jitter of the detectors, the time tagger, and the laser pulse, one obtains a timing jitter of $<$ 20 ps for both detectors as specified by the manufacturer.

Bibliography

[1] G. Binnig, H. Rohrer, C. Gerber, and E. Weibel, Phys. Rev. Lett. **49**, 57 (1982).

[2] G. Binnig, C. F. Quate, and C. Gerber, Phys. Rev. Lett. **56**, 930 (1986).

[3] A. Einstein, B. Podolsky, and N. Rosen, Phys. Rev. **47**, 777 (1935).

[4] J. S. Bell, Rev. Mod. Phys. **38**, 447 (1966).

[5] J. I. Cirac and P. Zoller, Phys. Rev. Lett. **74**, 4091 (1995).

[6] D. Loss and D. P. DiVincenzo, Phys. Rev. A **57**, 120 (1998).

[7] J. Clarke and F. K. Wilhelm, Nature **453**, 1031 (2008).

[8] C. H. Bennett and G. Brassard, Theor. Comput. Sci. **560**, 7 (2014).

[9] B. Hensen, H. Bernien, A. E. Dréau, A. Reiserer, N. Kalb, M. S. Blok, J. Ruitenberg, R. F. Vermeulen, R. N. Schouten, C. Abellán, W. Amaya, V. Pruneri, M. W. Mitchell, M. Markham, D. J. Twitchen, D. Elkouss, S. Wehner, T. H. Taminiau, and R. Hanson, Nature **526**, 682 (2015).

[10] P. Lodahl, S. Mahmoodian, and S. Stobbe, Rev. Mod. Phys. **87**, 347 (2015).

[11] P. Senellart, G. Solomon, and A. White, Nat. Nanotechnol. **12**, 1026 (2017).

[12] R. J. Warburton, Nat. Mater. **12**, 483 (2013).

[13] X. Ding, Y. He, Z.-C. Duan, N. Gregersen, M.-C. Chen, S. Unsleber, S. Maier, C. Schneider, M. Kamp, S. Höfling, C.-Y. Lu, and J.-W. Pan, Phys. Rev. Lett. **116**, 020401 (2016).

[14] N. Somaschi, V. Giesz, L. D. Santis, J. C. Loredo, M. P. Almeida, G. Hornecker, S. L. Portalupi, T. Grange, C. Antón, J. Demory, C. Gómez, I. Sagnes, N. D. Lanzillotti-Kimura, A. Lemaítre, A. Auffeves, A. G. White, L. Lanco, and P. Senellart, Nat. Photonics **10**, 340 (2016).

[15] M. Atatüre, J. Dreiser, A. Badolato, A. Högele, K. Karrai, and A. Imamoglu, Science **312**, 551 (2006).

[16] B. D. Gerardot, D. Brunner, P. A. Dalgarno, P. Öhberg, S. Seidl, M. Kroner, K. Karrai, N. G. Stoltz, P. M. Petroff, and R. J. Warburton, Nature **451**, 441 (2008).

[17] J. H. Prechtel, J. H. A. V. Kuhlmann, A. Ludwig, S. R. Valentin, A. D. Wieck, and R. J. Warburton, Nat. Mater. **15**, 981 (2016).

[18] C. Santori, D. Fattal, J. Vučković, G. S. Solomon, and Y. Yamamoto, Nature **419**, 594 (2002).

[19] M. Gschrey, A. Thoma, P. Schnauber, M. Seifried, R. Schmidt, B. Wohlfeil, L. Krüger, J. H. Schulze, T. Heindel, S. Burger, F. Schmidt, A. Strittmatter, S. Rodt, and S. Reitzenstein, Nat. Commun. **6**, 7662 (2015).

[20] G. Kiršanskė, H. Thyrrestrup, R. S. Daveau, C. L. Dreeßen, T. Pregnolato, L. Midolo, P. Tighineanu, A. Javadi, S. Stobbe, R. Schott, A. Ludwig, A. D. Wieck, S. I. Park, J. D. Song, A. V. Kuhlmann, I. Söllner, M. C. Löbl, R. J. Warburton, and P. Lodahl, Phys. Rev. B **96**, 165306 (2017).

[21] Y.-M. He, J. Liu, S. Maier, M. Emmerling, S. Gerhardt, M. Davanco, K. Srinivasan, C. Schneider, and S. Höfling, Optica **4**, 802 (2017).

[22] F. Liu, A. J. Brash, J. O'Hara, L. M. P. P. Martins, C. L. Phillips, R. J. Coles, B. Royall, E. Clarke, C. Bentham, N. Prtljaga, I. E. Itskevich, L. R. Wilson, M. S. Skolnick, and A. M. Fox, Nat. Nanotechnol. **13**, 835 (2018).

[23] J. Dreiser, M. Atatüre, C. Galland, T. Müller, A. Badolato, and A. Imamoglu, Phys. Rev. B **77**, 075317 (2008).

[24] D. Press, T. D. Ladd, B. Zhang, and Y. Yamamoto, Nature **456**, 218 (2008).

[25] A. J. Ramsay, T. M. Godden, S. J. Boyle, E. M. Gauger, A. Nazir, B. W. Lovett, A. M. Fox, and M. S. Skolnick, Phys. Rev. Lett. **105**, 177402 (2010).

[26] C.-Y. Lu, Y. Zhao, A. N. Vamivakas, C. Matthiesen, S. Fält, A. Badolato, and M. Atatüre, Phys. Rev. B **81**, 035332 (2010).

[27] A. Delteil, Z. Sun, W. bo Gao, E. Togan, S. Faelt, and A. Imamoglu, Nat. Phys. **12**, 218 (2016).

[28] R. Stockill, M. J. Stanley, L. Huthmacher, E. Clarke, M. Hugues, A. J. Miller, C. Matthiesen, C. Le Gall, and M. Atatüre, Phys. Rev. Lett. **119**, 010503 (2017).

[29] D. P. DiVincenzo, Fortschritte der Physik: Progress of Physics **48**, 771 (2000).

[30] J. Houel, A. V. Kuhlmann, L. Greuter, F. Xue, M. Poggio, B. D. Gerardot, P. A. Dalgarno, A. Badolato, P. M. Petroff, A. Ludwig, D. Reuter, A. D. Wieck, and R. J. Warburton, Phys. Rev. Lett. **108**, 107401 (2012).

[31] A. Bechtold, D. Rauch, F. Li, T. Simmet, P.-L. Ardelt, A. Regler, K. Müller, N. A. Sinitsyn, and J. J. Finley, Nat. Phys. **11**, 1005 (2015).

[32] R. Stockill, C. Le Gall, C. Matthiesen, L. Huthmacher, E. Clarke, M. Hugues, and M. Atatüre, Nat. Commun. **7**, 12745 (2016).

[33] G. Ethier-Majcher, D. Gangloff, R. Stockill, E. Clarke, M. Hugues, C. Le Gall, and M. Atatüre, Phys. Rev. Lett. **119**, 130503 (2017).

[34] D. Ding, M. H. Appel, A. Javadi, X. Zhou, M. C. Löbl, I. Söllner, R. Schott, C. Papon, T. Pregnolato, L. Midolo, A. D. Wieck, A. Ludwig, R. J. Warburton, T. Schröder, and P. Lodahl, Phys. Rev. Applied **11**, 031002 (2019).

[35] K. Karrai, R. J. Warburton, C. Schulhauser, A. Högele, B. Urbaszek, E. J. McGhee, A. O. Govorov, J. M. Garcia, B. D. Gerardot, and P. M. Petroff, Nature **427**, 135 (2003).

[36] M. Kroner, A. O. Govorov, S. Remi, B. Biedermann, S. Seidl, A. Badolato, P. M. Petroff, W. Zhang, R. Barbour, B. D. Gerardot, R. J. Warburton, and K. Karrai, Nature **451**, 311 (2008).

[37] L. Sapienza, M. Davanço, A. Badolato, and K. Srinivasan, Nat. Commun. **6**, 7833 (2015).

[38] A. V. Kuhlmann, J. Houel, A. Ludwig, L. Greuter, D. Reuter, A. D. Wieck, M. Poggio, and R. J. Warburton, Nat. Phys. **9**, 570 (2013).

[39] A. V. Kuhlmann, J. H. Prechtel, J. Houel, D. Reuter, A. D. Wieck, and R. J. Warburton, Nat. Commun. **6**, 8204 (2014).

[40] A. Ludwig, J. H. Prechtel, A. V. Kuhlmann, J. Houel, S. R. Valentin, R. J. Warburton, and A. D. Wieck, J. Cryst. Growth **477**, 193 (2017).

[41] J. H. Prechtel, A. V. Kuhlmann, J. Houel, L. Greuter, A. Ludwig, D. Reuter, A. D. Wieck, and R. J. Warburton, Phys. Rev. X **3**, 041006 (2014).

[42] B. Merkel, A. Kurzmann, J.-H. Schulze, A. Strittmatter, M. Geller, and A. Lorke, Phys. Rev. B **95**, 115305 (2017).

[43] M. Atatüre, D. Englund, N. Vamivakas, S.-Y. Lee, and J. Wrachtrup, Nat. Rev. Mater. **3**, 38 (2018).

[44] L. Besombes, K. Kheng, L. Marsal, and H. Mariette, Phys. Rev. B **63**, 155307 (2001).

[45] M. C. Löbl, S. Scholz, I. Söllner, J. Ritzmann, T. Denneulin, A. Kovacs, B. E. Kardynał, A. D. Wieck, A. Ludwig, and R. J. Warburton, Commun. Phys. **2**, 93 (2018).

[46] L. Huthmacher, R. Stockill, E. Clarke, M. Hugues, C. Le Gall, and M. Atatüre, Phys. Rev. B **97**, 241413 (2018).

[47] W. Zhang, Z. Shi, D. Huo, X. Guo, F. Zhang, L. Chen, Q. Wang, B. Zhang, and C. Peng, Appl. Phys. Lett. **112**, 153108 (2018).

[48] P. Atkinson, O. G. Schmidt, S. P. Bremner, and D. A. Ritchie, C. R. Phys. **9**, 788 (2008).

[49] T. Pfau, A. Gushterov, J. Reithmaier, I. Cestier, G. Eisenstein, E. Linder, and D. Gershoni, Appl. Phys. Lett. **95**, 243106 (2009).

[50] K. D. Jöns, P. Atkinson, M. Müller, M. Heldmaier, S. M. Ulrich, O. G. Schmidt, and P. Michler, Nano Lett. **13**, 126 (2012).

[51] D. Gangloff, G. Éthier-Majcher, C. Lang, E. Denning, J. Bodey, D. Jackson, E. Clarke, M. Hugues, C. Le Gall, and M. Atatüre, Science **364**, 62 (2019).

[52] M. D. Shulman, S. P. Harvey, J. M. Nichol, S. D. Bartlett, A. C. Doherty, V. Umansky, and A. Yacoby, Nat. Commun. **5**, 5156 (2014).

[53] I. Schwartz, D. Cogan, E. R. Schmidgall, Y. Don, L. Gantz, O. Kenneth, N. H. Lindner, and D. Gershoni, Science **354**, 434 (2016).

[54] D. Kim, A. A. Kiselev, R. S. Ross, M. T. Rakher, C. Jones, and T. D. Ladd, Phys. Rev. Applied **5**, 024014 (2016).

[55] B. Joecker, P. Cerfontaine, F. Haupt, L. R. Schreiber, B. E. Kardynał, and H. Bluhm, Phys. Rev. B **99**, 205415 (2019).

[56] Y. Tsuchimoto, P. Knüppel, A. Delteil, Z. Sun, M. Kroner, and A. Imamoglu, Phys. Rev. B **96**, 165312 (2017).

[57] D. Cadeddu, M. Munsch, N. Rossi, J.-M. Gérard, J. Claudon, R. J. Warburton, and M. Poggio, Phys. Rev. Applied **8**, 031002 (2017).

[58] H.-A. Engel, J. M. Taylor, M. D. Lukin, and A. Imamoglu, arXiv:cond-mat/0612700 (2006).

[59] J. Wolters, G. Buser, A. Horsley, L. Béguin, A. Jöckel, J.-P. Jahn, R. J. Warburton, and P. Treutlein, Phys. Rev. Lett. **119**, 060502 (2017).

[60] D. Najer, I. Söllner, P. Sekatski, V. Dolique, M. C. Löbl, D. Riedel, R. Schott, S. Starosielec, S. R. Valentin, A. D. Wieck, N. Sangouard, A. Ludwig, and R. J. Warburton, Nature **575**, 622 (2019).

[61] A. Faraon, I. Fushman, D. Englund, N. Stoltz, P. Petroff, and J. Vučković, Nat. Phys. **4**, 859 (2008).

[62] A. M. Smith and S. Nie, Accounts of chemical research **43**, 190 (2009).

[63] L. P. Kouwenhoven, D. G. Austing, and S. Tarucha, Rep. Prog. Phys. **64**, 701 (2001).

[64] L. Jacak, European Journal of Physics **21**, 487 (2000).

[65] I. N. Stranski and L. Krastanow, Monatshefte für Chemie/Chemical Monthly **71**, 351 (1937).

[66] Z. M. Wang, B. L. Liang, K. A. Sablon, and G. J. Salamo, Appl. Phys. Lett. **90**, 113120 (2007).

[67] D. Leonard, K. Pond, and P. M. Petroff, Phys. Rev. B **50**, 11687 (1994).

[68] Z. Wasilewski, S. Fafard, and J. McCaffrey, J. Cryst. Growth **201/202**, 1131 (1999).

[69] V. Fock, Zeitschrift für Physik **47**, 446 (1928).

[70] C. G. Darwin, Proc. Camb. Phil. Soc. **27**, 86 (1930).

[71] R. J. Warburton, B. T. Miller, C. S. Dürr, C. Bödefeld, K. Karrai, J. P. Kotthaus, G. Medeiros-Ribeiro, P. M. Petroff, and S. Huant, Phys. Rev. B **58**, 16221 (1998).

[72] K. H. Madsen, P. Kaer, A. Kreiner-Møller, S. Stobbe, A. Nysteen, J. Mørk, and P. Lodahl, Phys. Rev. B **88**, 045316 (2013).

[73] S. Raymond, S. Studenikin, A. Sachrajda, Z. Wasilewski, S. J. Cheng, W. Sheng, P. Hawrylak, A. Babinski, M. Potemski, G. Ortner, and M. Bayer, Phys. Rev. Lett. **92**, 187402 (2004).

[74] A. V. Madhav and T. Chakraborty, Phys. Rev. B **49**, 8163 (1994).

[75] L. Chirolli, E. Prada, F. Guinea, R. Roldán, and P. San-Jose, 2D Materials **6**, 025010 (2019).

[76] B. Van Hattem, P. Corfdir, P. Brereton, P. Pearce, A. M. Graham, M. J. Stanley, M. Hugues, M. Hopkinson, and R. T. Phillips, Phys. Rev. B **87**, 205308 (2013).

[77] M. C. Löbl, L. Zhai, J.-P. Jahn, J. Ritzmann, Y. Huo, A. D. Wieck, O. G. Schmidt, A. Ludwig, A. Rastelli, and R. J. Warburton, Phys. Rev. B **100**, 155402 (2019).

[78] M. Fox, "Optical properties of solids," (Oxford University Press, Oxford, 2010).

[79] R. J. Warburton, C. Schäflein, D. Haft, F. Bickel, A. Lorke, K. Karrai, J. M. Garcia, W. Schoenfeld, and P. M. Petroff, Nature **405**, 926 (2000).

[80] E. A. Zibik, T. Grange, B. A. Carpenter, N. E. Porter, R. Ferreira, G. Bastard, D. Stehr, S. Winnerl, M. Helm, H. Y. Liu, M. S. Skolnick, and L. R. Wilson, Nat. Mater. **8**, 803 (2009).

[81] A. Muller, E. B. Flagg, P. Bianucci, X. Y. Wang, D. G. Deppe, W. Ma, J. Zhang, G. J. Salamo, M. Xiao, and C. K. Shih, Phys. Rev. Lett. **99**, 187402 (2007).

[82] E. B. Flagg, A. Muller, J. W. Robertson, S. Founta, D. G. Deppe, M. Xiao, W. Ma, G. J. Salamo, and C.-K. Shih, Nat. Phys. **5**, 203 (2009).

[83] A. V. Kuhlmann, J. Houel, D. Brunner, A. Ludwig, D. Reuter, A. D. Wieck, and R. J. Warburton, Rev. Sci. Instrum. **84**, 073905 (2013).

[84] A. O. Govorov, K. Karrai, and R. J. Warburton, Phys. Rev. B **67**, 241307 (2003).

[85] N. A. J. M. Kleemans, J. van Bree, A. O. Govorov, J. G. Keizer, G. J. Hamhuis, R. Nötzel, A. Y. Silov, and P. M. Koenraad, Nat. Phys. **6**, 534 (2010).

[86] A. K. Rai, S. Gordon, A. Ludwig, A. D. Wieck, A. Zrenner, and D. Reuter, Phys. Status Solidi B **253**, 437 (2016).

[87] R. B. Patel, A. J. Bennett, I. Farrer, C. A. Nicoll, D. A. Ritchie, and A. J. Shields, Nat. Photonics **4**, 632 (2010).

[88] J.-P. Jahn, M. Munsch, L. Béguin, A. V. Kuhlmann, M. Renggli, Y. Huo, F. Ding, R. Trotta, M. Reindl, O. G. Schmidt, A. Rastelli, P. Treutlein, and R. J. Warburton, Phys. Rev. B **92**, 245439 (2015).

[89] C. P. Anderson, A. Bourassa, K. C. Miao, G. Wolfowicz, P. J. Mintun, A. L. Crook, H. Abe, J. U. Hassan, N. T. Son, T. Ohshima, and D. D. Awschalom, Science (2019), 10.1126/science.aax9406.

[90] A. Kurzmann, A. Ludwig, A. D. Wieck, A. Lorke, and M. Geller, Nano Lett. **16**, 3367 (2016).

[91] M. C. Löbl, I. Söllner, A. Javadi, T. Pregnolato, R. Schott, L. Midolo, A. V. Kuhlmann, S. Stobbe, A. D. Wieck, P. Lodahl, A. Ludwig, and R. J. Warburton, Phys. Rev. B **96**, 165440 (2017).

[92] J. J. Finley, P. W. Fry, A. D. Ashmore, A. Lemaître, A. I. Tartakovskii, R. Oulton, D. J. Mowbray, M. S. Skolnick, M. Hopkinson, P. D. Buckle, and P. A. Maksym, Phys. Rev. B **63**, 161305 (2001).

[93] C. Papon, X. Zhou, H. Thyrrestrup, Z. Liu, S. Stobbe, R. Schott, A. D. Wieck, A. Ludwig, P. Lodahl, and L. Midolo, Optica **6**, 524 (2019).

[94] M. L. Andersen, S. Stobbe, A. S. Sørensen, and P. Lodahl, Nat. Phys. **7**, 215 (2011).

[95] E. F. Schubert, *Physical foundations of solid-state devices* (E. Fred Schubert, 2015).

[96] H. Casey Jr, D. Sell, and K. Wecht, J. Appl. Phys. **46**, 250 (1975).

[97] D. Pinotsi, P. Fallahi, J. Miguel-Sanchez, and A. Imamoğlu, IEEE J. Quantum Electron. **47**, 1371 (2011).

[98] M. Kroutvar, Y. Ducommun, D. Heiss, M. Bichler, D. Schuh, G. Abstreiter, and J. J. Finley, Nature **432**, 81 (2004).

[99] A. Greilich, A. Shabaev, D. Yakovlev, A. L. Efros, I. Yugova, D. Reuter, A. Wieck, and M. Bayer, Science **317**, 1896 (2007).

[100] S. T. Yilmaz, P. Fallahi, and A. Imamoglu, Phys. Rev. Lett. **105**, 033601 (2010).

[101] A. Greilich, S. E. Economou, S. Spatzek, D. R. Yakovlev, D. Reuter, A. D. Wieck, T. L. Reinecke, and M. Bayer, Nat. Phys. **5**, 262 (2009).

[102] A. N. Vamivakas, Y. Zhao, C.-Y. Lu, and M. Atatüre, Nat. Phys. **5**, 198 (2009).

[103] I. Wilson-Rae, P. Zoller, and A. Imamoglu, Phys. Rev. Lett. **92**, 075507 (2004).

[104] I. Söllner, L. Midolo, and P. Lodahl, Phys. Rev. Lett. **116**, 234301 (2016).

[105] A. Javadi, I. Söllner, M. Arcari, S. L. Hansen, L. Midolo, S. Mahmoodian, G. Kiršanskė, T. Pregnolato, E. H. Lee, J. D. Song, S. Stobbe, and P. Lodahl, Nat. Commun. **6**, 8655 (2015).

[106] C. Reese, C. Becher, A. Imamoglu, E. Hu, B. D. Gerardot, and P. M. Petroff, Appl. Phys. Lett. **78**, 2279 (2001).

[107] P. M. Vora, A. S. Bracker, S. G. Carter, T. M. Sweeney, M. Kim, C. S. Kim, L. Yang, P. G. Brereton, S. E. Economou, and D. Gammon, Nat. Commun. **6**, 7665 (2015).

[108] V. Nagavarapu, R. Jhaveri, and J. C. S. Woo, IEEE Transactions on Electron Devices **55**, 1013 (2008).

[109] S. E. Hosseini and M. Kamali Moghaddam, Mater. Sci. Semicond. Process. **30**, 56 (2015).

[110] K. G. Lagoudakis, K. Fischer, T. Sarmiento, A. Majumdar, A. Rundquist, J. Lu, M. Bajcsy, and J. Vučković, New J. Phys. **15**, 113056 (2013).

[111] L. Midolo, T. Pregnolato, G. Kiršanskė, and S. Stobbe, Nanotechnology **26**, 484002 (2015).

[112] J. M. Smith, P. A. Dalgarno, R. J. Warburton, A. O. Govorov, K. Karrai, B. D. Gerardot, and P. M. Petroff, Phys. Rev. Lett. **94**, 197402 (2005).

[113] S. G. Carter, T. M. Sweeney, M. Kim, C. S. Kim, D. Solenov, S. E. Economou, T. L. Reinecke, L. Yang, A. S. Bracker, and D. Gammon, Nat. Photonics **7**, 329 (2013).

[114] K. Müller, A. Bechtold, C. Ruppert, T. Kaldewey, M. Zecherle, J. S. Wildmann, M. Bichler, H. J. Krenner, J. M. Villas-Bôas, G. Abstreiter, M. Betz, and J. J. Finley, Ann. Phys. **525**, 49 (2013).

[115] M. Kroner, K. M. Weiss, B. Biedermann, S. Seidl, A. W. Holleitner, A. Badolato, P. M. Petroff, P. Öhberg, R. J. Warburton, and K. Karrai, Phys. Rev. B **78**, 075429 (2008).

[116] M. Kroner, K. M. Weiss, B. Biedermann, S. Seidl, S. Manus, A. W. Holleitner, A. Badolato, P. M. Petroff, B. D. Gerardot, R. J. Warburton, and K. Karrai, Phys. Rev. Lett. **100**, 156803 (2008).

[117] S. Seidl, M. Kroner, P. A. Dalgarno, A. Högele, J. M. Smith, M. Ediger, B. D. Gerardot, J. M. Garcia, P. M. Petroff, K. Karrai, and R. J. Warburton, Phys. Rev. B **72**, 195339 (2005).

[118] W. Lei, M. Offer, A. Lorke, C. Notthoff, C. Meier, O. Wibbelhoff, and A. D. Wieck, Appl. Phys. Lett. **92**, 193111 (2008).

[119] O. Göktaş, J. Weber, J. Weis, and K. von Klitzing, Physica E Low Dimens. Syst. Nanostruct. **40**, 1579 (2008).

[120] A. Javadi, D. Ding, M. H. Appel, S. Mahmoodian, M. C. Löbl, I. Söllner, R. Schott, C. Papon, T. Pregnolato, S. Stobbe, L. Midolo, T. Schröder, A. D. Wieck, A. Ludwig, R. J. Warburton, and P. Lodahl, Nat. Nanotechnol. **13**, 398 (2018).

[121] L. Midolo and P. Lodahl, "personal communication," (2016–2019).

[122] X. Sun, L. Hu, H. Song, Z. Li, D. Li, H. Jiang, and G. Miao, Solid-State Electronics **53**, 1032 (2009).

[123] E. F. Schubert, *Doping in III-V semiconductors* (E. Fred Schubert, 2015).

[124] H. Thyrrestrup, G. Kiršanskė, H. Le Jeannic, T. Pregnolato, L. Zhai, L. Raahauge, L. Midolo, N. Rotenberg, A. Javadi, R. Schott, A. D. Wieck, A. Ludwig, M. C. Löbl, I. Söllner, R. J. Warburton, and P. Lodahl, Nano Lett. **18**, 1801 (2017).

[125] A. Ludwig, "personal communication," (2016–2019).

[126] M. Müller, S. Bounouar, K. D. Jöns, M. Glässl, and P. Michler, Nat. Photonics **8**, 224 (2014).

[127] W. B. Gao, P. Fallahi, E. Togan, J. Miguel-Sanchez, and A. Imamoglu, Nature **491**, 426 (2012).

[128] D. Englund, D. Fattal, E. Waks, G. Solomon, B. Zhang, T. Nakaoka, Y. Arakawa, Y. Yamamoto, and J. Vučković, Phys. Rev. Lett. **95**, 013904 (2005).

[129] T. Volz, A. Reinhard, M. Winger, A. Badolato, K. J. Hennessy, E. L. Hu, and A. Imamoğlu, Nat. Photonics **6**, 605 (2012).

[130] M. Arcari, I. Söllner, A. Javadi, S. Lindskov Hansen, S. Mahmoodian, J. Liu, H. Thyrrestrup, E. H. Lee, J. D. Song, S. Stobbe, and P. Lodahl, Phys. Rev. Lett. **113**, 093603 (2014).

[131] Y.-J. Wei, Y.-M. He, M.-C. Chen, Y.-N. Hu, Y. He, D. Wu, C. Schneider, M. Kamp, S. Höfling, C.-Y. Lu, and J.-W. Pan, Nano Lett. **14**, 6515 (2014).

[132] T. Kaldewey, S. Lüker, A. V. Kuhlmann, S. R. Valentin, J.-M. Chauveau, A. Ludwig, A. D. Wieck, D. E. Reiter, T. Kuhn, and R. J. Warburton, Phys. Rev. B **95**, 241306 (2017).

[133] A. J. Brash, J. Iles-Smith, C. L. Phillips, D. P. S. McCutcheon, J. O'Hara, E. Clarke, B. Royall, L. R. Wilson, J. Mørk, M. S. Skolnick, A. M. Fox, and A. Nazir, Phys. Rev. Lett. **123**, 167403 (2019).

[134] Z. X. Koong, D. Scerri, M. Rambach, T. S. Santana, S. I. Park, J. D. Song, E. M. Gauger, and B. D. Gerardot, Phys. Rev. Lett. **123**, 167402 (2019).

[135] D. Press, K. D. Greve, P. L. McMahon, T. D. Ladd, B. Friess, C. Schneider, M. Kamp, S. Höfling, A. Forchel, and Y. Yamamoto, Nat. Photonics **4**, 367 (2008).

[136] G. Wüst, M. Munsch, F. Maier, A. V. Kuhlmann, A. Ludwig, A. D. Wieck, D. Loss, M. Poggio, and R. J. Warburton, Nat. Nanotechnol. **11**, 885 (2016).

[137] Q. Q. Wang, A. Muller, P. Bianucci, E. Rossi, Q. K. Xue, T. Takagahara, C. Piermarocchi, A. H. MacDonald, and C. K. Shih, Phys. Rev. B **72**, 035306 (2005).

[138] A. Carmele, F. Milde, M.-R. Dachner, M. B. Harouni, R. Roknizadeh, M. Richter, and A. Knorr, Phys. Rev. B **81**, 195319 (2010).

[139] Y. Toda, O. Moriwaki, M. Nishioka, and Y. Arakawa, Phys. Rev. Lett. **82**, 4114 (1999).

[140] A. Vasanelli, R. Ferreira, and G. Bastard, Phys. Rev. Lett. **89**, 216804 (2002).

[141] J. Finley, A. Lemaître, A. Ashmore, D. Mowbray, M. Skolnick, M. Hopkinson, and T. Krauss, physica status solidi (b) **224**, 373 (2001).

[142] A. Lemaître, A. D. Ashmore, J. J. Finley, D. J. Mowbray, M. S. Skolnick, M. Hopkinson, and T. F. Krauss, Phys. Rev. B **63**, 161309 (2001).

[143] C. Schulhauser, R. J. Warburton, A. Högele, A. Govorov, K. Karrai, J. Garcia, B. Gerardot, and P. Petroff, Physica E **21**, 184 (2004).

[144] K. M. Weiss, J. Miguel-Sanchez, and J. M. Elzerman, Sci. Rep. **3**, 3121 (2013).

[145] M. Winger, T. Volz, G. Tarel, S. Portolan, A. Badolato, K. J. Hennessy, E. L. Hu, A. Beveratos, J. Finley, V. Savona, and A. Imamoglu, Phys. Rev. Lett. **103**, 207403 (2009).

[146] S. Ates, S. Ulrich, A. Ulhaq, S. Reitzenstein, A. Löffler, S. Höfling, A. Forchel, and P. Michler, Nat. Photonics **3**, 724 (2009).

[147] M. Kaniber, A. Laucht, A. Neumann, J. M. Villas-Bôas, M. Bichler, M.-C. Amann, and J. J. Finley, Phys. Rev. B **77**, 161303 (2008).

[148] M. Settnes, P. Kaer, A. Moelbjerg, and J. Mork, Phys. Rev. Lett. **111**, 067403 (2013).

[149] J. M. Villas-Bôas, S. E. Ulloa, and A. O. Govorov, Phys. Rev. Lett. **94**, 057404 (2005).

[150] J. Villas-Bôas, S. E. Ulloa, and A. O. Govorov, Physica E **26**, 337 (2005).

[151] B. Urbaszek, E. J. McGhee, M. Krüger, R. J. Warburton, K. Karrai, T. Amand, B. D. Gerardot, P. M. Petroff, and J. M. Garcia, Phys. Rev. B **69**, 035304 (2004).

[152] C. Nicoll, C. Salter, R. Stevenson, A. Hudson, P. Atkinson, K. Cooper, A. Shields, and D. Ritchie, J. Cryst. Growth **311**, 1811 (2009).

[153] S. M. Ulrich, S. Weiler, M. Oster, M. Jetter, A. Urvoy, R. Löw, and P. Michler, Phys. Rev. B **90**, 125310 (2014).

[154] S. L. Portalupi, M. Widmann, C. Nawrath, M. Jetter, P. Michler, J. Wrachtrup, and I. Gerhardt, Nat. Commun. **7**, 13632 (2016).

[155] M. Arzberger, U. Käsberger, G. Böhm, and G. Abstreiter, Appl. Phys. Lett. **75**, 3968 (1999).

[156] A. F. Tsatsul'nikov, A. R. Kovsh, A. E. Zhukov, Y. M. Shernyakov, Y. G. Musikhin, V. M. Ustinov, N. A. Bert, P. S. Kop'ev, Z. I. Alferov, A. M. Mintairov, J. L. Merz, N. N. Ledentsov, and D. Bimberg, J. Appl. Phys. **88**, 6272 (2000).

[157] X. M. Lu, S. Matsubara, Y. Nakagawa, T. Kitada, and T. Isu, J. Cryst. Growth **425**, 106 (2015).

[158] F. Tutu, P. Lam, J. Wu, N. Miyashita, Y. Okada, K.-H. Lee, N. Ekins-Daukes, J. Wilson, and H. Liu, Appl. Phys. Lett. **102**, 163907 (2013).

[159] P. E. Vullum, M. Nord, M. Vatanparast, S. F. Thomassen, C. Boothroyd, R. Holmestad, B.-O. Fimland, and T. W. Reenaas, Sci. Rep. **7**, 45376 (2017).

[160] J. Blokland, M. Bozkurt, J. Ulloa, D. Reuter, A. Wieck, P. Koenraad, P. Christianen, and J. Maan, Appl. Phys. Lett. **94**, 023107 (2009).

[161] B. Urbaszek, R. J. Warburton, K. Karrai, B. D. Gerardot, P. M. Petroff, and J. M. Garcia, Phys. Rev. Lett. **90**, 247403 (2003).

[162] M. E. Ware, E. A. Stinaff, D. Gammon, M. F. Doty, A. S. Bracker, D. Gershoni, V. L. Korenev, Ş. C. Bădescu, Y. Lyanda-Geller, and T. L. Reinecke, Phys. Rev. Lett. **95**, 177403 (2005).

[163] R. J. Warburton, R. J. Nicholas, L. K. Howard, and M. T. Emeny, Phys. Rev. B **43**, 14124 (1991).

[164] A. Di Carlo, Semicond. Sci. Tech. **18**, R1 (2002).

[165] B. T. Miller, W. Hansen, S. Manus, R. J. Luyken, A. Lorke, J. P. Kotthaus, S. Huant, G. Medeiros-Ribeiro, and P. M. Petroff, Phys. Rev. B **56**, 6764 (1997).

[166] M. Bayer, G. Ortner, O. Stern, A. Kuther, A. A. Gorbunov, A. Forchel, P. Hawrylak, S. Fafard, K. Hinzer, T. L. Reinecke, S. N. Walck, J. P. Reithmaier, F. Klopf, and F. Schäfer, Phys. Rev. B **65**, 195315 (2002).

[167] A. Franceschetti, L. W. Wang, H. Fu, and A. Zunger, Phys. Rev. B **58**, R13367 (1998).

[168] S. Rudin, T. L. Reinecke, and M. Bayer, Phys. Rev. B **74**, 161305 (2006).

[169] S. Pennycook and P. Nellist, in *Impact of electron and scanning probe microscopy on materials research* (Springer, 1999) pp. 161–207.

[170] D. Pfannkuche, R. R.Gerhardts, P. A. Maksym, and V. Gudmundsson, Physica B: Condensed Matter **189**, 6 (1993).

[171] C. Cohen-Tannoudji, B. Diu, and F. Laloe, Quantum Mechanics, 2, 626. ISBN 0-471-16435-6. Wiley-VCH (1986).

[172] S.-J. Cheng, W. Sheng, and P. Hawrylak, Phys. Rev. B **68**, 235330 (2003).

[173] L. Landau, Zeitschrift für Physik **64**, 629 (1930).

[174] A. Babinski, M. Potemski, S. Raymond, J. Lapointe, and Z. R. Wasilewski, Phys. Rev. B **74**, 155301 (2006).

[175] A. Babinski, M. Potemski, and P. C. Christianen, C. R. Physique **14**, 121 (2013).

[176] W. Nakwaski, Physica B **210**, 1 (1995).

[177] A. Zhou and W. Sheng, Eur. Phys. J. B **68**, 233 (2009).

[178] I. Strzalkowski, S. Joshi, and C. R. Crowell, Appl. Phys. Lett. **28** (1976).

[179] M. Grundmann, O. Stier, and D. Bimberg, Phys. Rev. B **52**, 11969 (1995).

[180] A. Wojs and P. Hawrylak, Phys. Rev. B **51**, 10880 (1995).

[181] L. Jacak, P. Hawrylak, and A. Wojs, *Quantum Dots* (Springer, Berlin, 1998).

[182] D. Huber, M. Reindl, Y. Huo, H. Huang, J. S. Wildmann, O. G. Schmidt, A. Rastelli, and R. Trotta, Nat. Commun. **8**, 15506 (2017).

[183] E. Schöll, L. Hanschke, L. Schweickert, K. D. Zeuner, M. Reindl, S. F. Covre da Silva, T. Lettner, R. Trotta, J. J. Finley, K. Müller, A. Rastelli, V. Zwiller, and K. D. Jöns, Nano Lett. **19**, 2404 (2019).

[184] R. M. Stevenson, R. J. Young, P. Atkinson, K. Cooper, D. A. Ritchie, and A. J. Shields, Nature **439**, 179 (2006).

[185] N. Akopian, N. H. Lindner, E. Poem, Y. Berlatzky, J. Avron, D. Gershoni, B. D. Gerardot, and P. M. Petroff, Phys. Rev. Lett. **96**, 130501 (2006).

[186] A. J. Hudson, R. M. Stevenson, A. J. Bennett, R. J. Young, C. A. Nicoll, P. Atkinson, K. Cooper, D. A. Ritchie, and A. J. Shields, Phys. Rev. Lett. **99**, 266802 (2007).

[187] Y. Chen, M. Zopf, R. Keil, F. Ding, and O. G. Schmidt, Nat. Commun. **9**, 2994 (2018).

[188] D. Huber, M. Reindl, S. F. Covre da Silva, C. Schimpf, J. Martín-Sánchez, H. Huang, G. Piredda, J. Edlinger, A. Rastelli, and R. Trotta, Phys. Rev. Lett. **121**, 033902 (2018).

[189] J. Liu, R. Su, Y. Wei, B. Yao, S. F. C. da Silva, Y. Yu, J. Iles-Smith, K. Srinivasan, A. Rastelli, J. Li, and X. Wang, Nat. Nanotechnol. **14**, 586 (2019).

[190] F. Basso Basset, M. B. Rota, C. Schimpf, D. Tedeschi, K. D. Zeuner, S. F. Covre da Silva, M. Reindl, V. Zwiller, K. D. Jöns, A. Rastelli, and R. Trotta, Phys. Rev. Lett. **123**, 160501 (2019).

[191] H. Wang, H. Hu, T.-H. Chung, J. Qin, X. Yang, J.-P. Li, R.-Z. Liu, H.-S. Zhong, Y.-M. He, X. Ding, Y.-H. Deng, Q. Dai, Y.-H. Huo, S. Höfling, C.-Y. Lu, and J.-W. Pan, Phys. Rev. Lett. **122**, 113602 (2019).

[192] N. Sangouard, C. Simon, J. Minář, H. Zbinden, H. de Riedmatten, and N. Gisin, Phys. Rev. A **76**, 050301(R) (2007).

[193] M. T. Rakher, R. J. Warburton, and P. Treutlein, Phys. Rev. A **88**, 053834 (2013).

[194] R. Keil, M. Zopf, Y. Chen, B. Höfer, J. Zhang, F. Ding, and O. G. Schmidt, Nat. Commun. **8**, 15501 (2017).

[195] L. Béguin, J.-P. Jahn, J. Wolters, M. Reindl, Y. Huo, R. Trotta, A. Rastelli, F. Ding, O. G. Schmidt, P. Treutlein, and R. J. Warburton, Phys. Rev. B **97**, 205304 (2018).

[196] B. C. Pursley, S. G. Carter, M. K. Yakes, A. S. Bracker, and D. Gammon, Nat. Commun. **9**, 115 (2018).

[197] J. P. Lee, L. M. Wells, B. Villa, S. Kalliakos, R. M. Stevenson, D. J. P. Ellis, I. Farrer, D. A. Ritchie, A. J. Bennett, and A. J. Shields, Phys. Rev. X **8**, 021078 (2018).

[198] Y. He, Y.-M. He, Y.-J. Wei, X. Jiang, M.-C. Chen, F.-L. Xiong, Y. Zhao, C. Schneider, M. Kamp, S. Höfling, C.-Y. Lu, and J.-W. Pan, Phys. Rev. Lett. **111**, 237403 (2013).

[199] A. Rastelli, S. Stufler, A. Schliwa, R. Songmuang, C. Manzano, G. Costantini, K. Kern, A. Zrenner, D. Bimberg, and O. G. Schmidt, Phys. Rev. Lett. **92**, 166104 (2004).

[200] D. Bruls, J. Vugs, P. Koenraad, H. Salemink, J. Wolter, M. Hopkinson, M. Skolnick, F. Long, and S. Gill, Appl. Phys. Lett. **81**, 1708 (2002).

[201] P. Atkinson, E. Zallo, and O. G. Schmidt, J. Appl. Phys. **112**, 054303 (2012).

[202] M. Fanfoni, F. Arciprete, C. Tirabassi, D. Del Gaudio, A. Filabozzi, A. Balzarotti, F. Patella, and E. Placidi, Phys. Rev. E **86**, 061605 (2012).

[203] C. Heyn, A. Stemmann, A. Schramm, H. Welsch, W. Hansen, and A. Nemcsics, Phys. Rev. B **76**, 075317 (2007).

[204] A. Rastelli, M. Stoffel, A. Malachias, T. Merdzhanova, G. Katsaros, K. Kern, T. H. Metzger, and O. G. Schmidt, Nano Lett. **8**, 1404 (2008).

[205] D. M. Nothern and J. M. Millunchick, J. Vac. Sci. Technol. B **30**, 060603 (2012).

[206] S. Miyamoto, O. Moutanabbir, E. E. Haller, and K. M. Itoh, Phys. Rev. B **79**, 165415 (2009).

[207] S. Bietti, C. Somaschini, L. Esposito, A. Fedorov, and S. Sanguinetti, Appl. Phys. Lett. **116**, 114311 (2014).

[208] A. Rastelli, R. Songmuang, and O. G. Schmidt, Physica E **23**, 384 (2004).

[209] A. Surrente, M. Felici, P. Gallo, A. Rudra, B. Dwir, and E. Kapon, Appl. Phys. Lett. **111**, 221102 (2017).

[210] L. Sapienza, J. Liu, J. D. Song, S. Fält, W. Wegscheider, A. Badolato, and K. Srinivasan, Sci. Rep. **7**, 6205 (2017).

[211] Y. H. Huo, A. Rastelli, and O. G. Schmidt, Appl. Phys. Lett. **102**, 152105 (2013).

[212] J. D. Plumhof, V. Křápek, L. Wang, A. Schliwa, D. Bimberg, A. Rastelli, and O. G. Schmidt, Phys. Rev. B **81**, 121309(R) (2010).

[213] M. Abbarchi, T. Kuroda, T. Mano, and K. Sakoda, J. Phys. Conf. Ser. **245**, 012049 (2010).

[214] L. O. Mereni, O. Marquardt, G. Juska, V. Dimastrodonato, E. P. O'Reilly, and E. Pelucchi, Phys. Rev. B **85**, 155453 (2012).

[215] Y. H. Huo, V. Křápek, A. Rastelli, and O. G. Schmidt, Phys. Rev. B **90**, 041304(R) (2014).

[216] X. Liu, N. Ha, H. Nakajima, T. Mano, T. Kuroda, B. Urbaszek, H. Kumano, I. Suemune, Y. Sakuma, and K. Sakoda, Phys. Rev. B **90**, 081301(R) (2014).

[217] J. Skiba-Szymanska, R. M. Stevenson, C. Varnava, M. Felle, J. Huwer, T. Müller, A. J. Bennett, J. P. Lee, I. Farrer, A. B. Krysa, P. Spencer, L. E. Goff, D. A. Ritchie, J. Heffernan, and A. J. Shields, Phys. Rev. Applied **8**, 014013 (2017).

[218] F. Basso Basset, S. Bietti, M. Reindl, L. Esposito, A. Fedorov, D. Huber, A. Rastelli, E. Bonera, R. Trotta, and S. Sanguinetti, Nano Lett. **18**, 505 (2018).

[219] P. A. Mulheran and J. A. Blackman, Phys. Rev. B **53**, 10261 (1996).

[220] J. A. Blackman and P. A. Mulheran, Phys. Rev. B **54**, 11681 (1996).

[221] M. Fanfoni, E. Placidi, F. Arciprete, E. Orsini, F. Patella, and A. Balzarotti, Phys. Rev. B **75**, 245312 (2007).

[222] F. Ratto, A. Locatelli, S. Fontana, S. Kharrazi, S. Ashtaputre, S. K. Kulkarni, S. Heun, and F. Rosei, Phys. Rev. Lett. **96**, 096103 (2006).

[223] P. Spencer, C. Chen, W. Michailow, H. Beere, and D. Ritchie, arXiv:1906.05842 (2019).

[224] S. Pratontep, M. Brinkmann, F. Nüesch, and L. Zuppiroli, Phys. Rev. B **69**, 165201 (2004).

[225] C. Heyn, T. Bartsch, S. Sanguinetti, D. Jesson, and W. Hansen, Nanoscale Res. Lett. **10**, 67 (2015).

[226] L. Wang, V. Křápek, F. Ding, F. Horton, A. Schliwa, D. Bimberg, A. Rastelli, and O. G. Schmidt, Phys. Rev. B **80**, 085309 (2009).

[227] M. Jo, T. Mano, Y. Sakuma, and K. Sakoda, J. Cryst. Growth **378**, 5 (2013).

[228] H. M. G. A. Tholen, J. S. Wildmann, A. Rastelli, R. Trotta, C. E. Pryor, E. Zallo, O. G. Schmidt, P. M. Koenraad, and A. Y. Silov, Phys. Rev. B **94**, 245301 (2016).

[229] A. Ulhaq, Q. Duan, E. Zallo, F. Ding, O. G. Schmidt, A. I. Tartakovskii, M. S. Skolnick, and E. A. Chekhovich, Phys. Rev. B **93**, 165306 (2016).

[230] N. Ares, V. N. Golovach, G. Katsaros, M. Stoffel, F. Fournel, L. I. Glazman, O. G. Schmidt, and S. De Franceschi, Phys. Rev. Lett. **110**, 046602 (2013).

[231] H. Watzinger, C. Kloeffel, L. Vukušić, M. D. Rossell, V. Sessi, J. Kukučka, R. Kirchschlager, E. Lausecker, A. Truhlar, M. Glaser, A. Rastelli, A. Fuhrer, D. Loss, and G. Katsaros, Nano Lett. **16**, 6879 (2016).

[232] P. A. Dalgarno, J. M. Smith, J. McFarlane, B. D. Gerardot, K. Karrai, A. Badolato, P. M. Petroff, and R. J. Warburton, Phys. Rev. B **77**, 245311 (2008).

[233] C. Teichert, M. Lagally, L. Peticolas, J. C. Bean, and J. Tersoff, Phys. Rev. B **53**, 16334 (1996).

[234] G. Springholz, V. Holy, M. Pinczolits, and G. Bauer, Science **282**, 734 (1998).

[235] M. Pinczolits, G. Springholz, and G. Bauer, Phys. Rev. B **60**, 11524 (1999).

[236] N. Gogneau, F. Fossard, E. Monroy, S. Monnoye, H. Mank, and B. Daudin, Appl. Phys. Lett. **84**, 4224 (2004).

[237] S. Kiravittaya, A. Rastelli, and O. Schmidt, Appl. Phys. Lett. **88**, 043112 (2006).

[238] G. Biasiol, V. Baranwal, S. Heun, M. Prasciolu, M. Tormen, A. Locatelli, T. Mentes, M. Nino, and L. Sorba, J. Cryst. Growth **323**, 176 (2011).

[239] A. Mohan, P. Gallo, M. Felici, B. Dwir, A. Rudra, J. Faist, and E. Kapon, Small **6**, 1268 (2010).

[240] A. Pimpinelli and T. L. Einstein, Phys. Rev. Lett. **99**, 226102 (2007).

[241] M. A. Groce, B. R. Conrad, W. G. Cullen, A. Pimpinelli, E. D. Williams, and T. L. Einstein, Surf. Sci. **606**, 53 (2012).

[242] D. L. González, A. Pimpinelli, and T. L. Einstein, Phys. Rev. E **84**, 011601 (2011).

[243] T. L. Einstein, A. Pimpinelli, and D. L. González, J. Cryst. growth **401**, 67 (2014).

[244] A. Pimpinelli, L. Tumbek, and A. Winkler, J. Phys. Chem. Lett. **5**, 995 (2014).

[245] R. J. Rossi, Wiley Online Library, ISBN 978-1-118-77116-7 (2018).

[246] M. C. Löbl, C. Spinnler, A. Javadi, L. Zhai, G. N. Nguyen, J. R. L. Midolo, P. Lodahl, A. D. Wieck, A. Ludwig, and R. J. Warburton, arXiv:1911.11784 (2019).

[247] T. Åberg and J. Utriainen, Phys. Rev. Lett. **22**, 1346 (1969).

[248] T. Åberg, Phys. Rev. A **4**, 1735 (1971).

[249] F. Bloch and P. A. Ross, Phys. Rev. **47**, 884 (1935).

[250] F. Bloch, Physical Review **48**, 187 (1935).

[251] P. Michler, *Single quantum dots: Fundamentals, applications and new concepts*, Vol. 90 (Springer Science & Business Media, 2003).

[252] W. Bambynek, B. Crasemann, R. W. Fink, H. U. Freund, H. Mark, C. D. Swift, R. E. Price, and P. V. Rao, Rev. Mod. Phys. **44**, 716 (1972).

[253] M.-G. Barthés-Labrousse, Microscopy Microanalysis Microstructures **6**, 253 (1995).

[254] B. Han, C. Robert, E. Courtade, M. Manca, S. Shree, T. Amand, P. Renucci, T. Taniguchi, K. Watanabe, X. Marie, L. E. Golub, M. M. Glazov, and B. Urbaszek, Phys. Rev. X **8**, 031073 (2018).

[255] P. Siyushev, H. Pinto, M. Vörös, A. Gali, F. Jelezko, and J. Wrachtrup, Phys. Rev. Lett. **110**, 167402 (2013).

[256] P. Blood, *Quantum Confined Laser Devices: Optical gain and recombination in semiconductors*, Vol. 23 (OUP Oxford, 2015).

[257] T. A. Carlson, Phys. Rev. **130**, 2361 (1963).

[258] P. J. Dean, J. D. Cuthbert, D. G. Thomas, and R. T. Lynch, Phys. Rev. Lett. **18**, 122 (1967).

[259] M. S. Skolnick, K. J. Nash, D. J. Mowbray, M. K. Saker, T. A. Fisher, D. M. Whittaker, D. W. Peggs, N. Miura, S. Sasaki, R. S. Smith, and S. J. Bass, Solid-State Electronics **37**, 825 (1994).

[260] M. J. Manfra, B. B. Goldberg, L. Pfeiffer, and K. West, Phys. Rev. B **57**, R9467 (1998).

[261] J. Hansom, C. H. H. Schulte, C. Matthiesen, M. J. Stanley, and M. Atatüre, Appl. Phys. Lett. **105**, 172107 (2014).

[262] B. Ohnesorge, M. Albrecht, J. Oshinowo, A. Forchel, and Y. Arakawa, Phys. Rev. B **54**, 11532 (1996).

[263] H. Kurtze, J. Seebeck, P. Gartner, D. R. Yakovlev, D. Reuter, A. D. Wieck, M. Bayer, and F. Jahnke, Phys. Rev. B **80**, 235319 (2009).

[264] X.-Q. Li, H. Nakayama, and Y. Arakawa, Phys. Rev. B **59**, 5069 (1999).

[265] J. C. Slater, Phys. Rev. **34**, 1293 (1929).

[266] H. A. Bethe and R. Jackiw, *Intermediate quantum mechanics* (CRC Press, 2018).

[267] J. Q. Grim, A. S. Bracker, M. Zalalutdinov, S. G. Carter, A. C. Kozen, M. Kim, C. S. Kim, J. T. Mlack, M. Yakes, B. Lee, and D. Gammon, Nat. Mater. **18**, 963 (2019).

[268] E. U. Condon, Phys. Rev. **36**, 1121 (1930).

[269] D. Chithrani, M. Korkusinski, S.-J. Cheng, P. Hawrylak, R. L. Williams, J. Lefebvre, P. J. Poole, and G. C. Aers, Physica E: Low-dimensional Systems and Nanostructures **26**, 322 (2005).

[270] M. Cygorek, M. Korkusinski, and P. Hawrylak, Phys. Rev. B **101**, 075307 (2020).

[271] J. R. Johansson, P. D. Nation, and F. Nori, Computer Physics Communications **184**, 1234 (2013).

[272] J. Hansom, C. H. H. Schulte, C. Le Gall, C. Matthiesen, E. Clarke, M. Hugues, J. M. Taylor, and M. Atatüre, Nat. Phys. **10**, 725 (2014).

[273] R. Loudon, *The quantum theory of light* (OUP Oxford, 2000).

[274] I. Yeo, P.-L. De Assis, A. Gloppe, E. Dupont-Ferrier, P. Verlot, N. S. Malik, E. Dupuy, J. Claudon, J.-M. Gérard, A. Auffèves, G. Nogues, S. Seidelin, J.-P. Poizat, O. Arcizet, and M. Richard, Nat. Nanotechnol. **9**, 106 (2014).

[275] M. Munsch, A. V. Kuhlmann, D. Cadeddu, J.-M. Gérard, J. Claudon, M. Poggio, and R. J. Warburton, Nat. Commun. **8**, 76 (2017).

[276] D. Heiss, S. Schaeck, H. Huebl, M. Bichler, G. Abstreiter, J. J. Finley, D. V. Bulaev, and D. Loss, Phys. Rev. B **76**, 241306 (2007).

[277] L. Bouet, M. Vidal, T. Mano, N. Ha, T. Kuroda, M. V. Durnev, M. M. Glazov, E. L. Ivchenko, X. Marie, T. Amand, K. Sakoda, G. Wang, and B. Urbaszek, Appl. Phys. Lett. **105**, 082111 (2014).

[278] F. Langer, D. Plischke, M. Kamp, and S. Höfling, Appl. Phys. Lett. **105**, 081111 (2014).

[279] P. Mooney, J. Appl. Phys. **67**, R1 (1990).

[280] V. Umansky and M. Heiblum, in *Molecular Beam Epitaxy* (Elsevier, 2013) pp. 121–137.

[281] L. Zhai, M. C. Löbl, G. N. Nguyen, J. Ritzmann, A. Javadi, C. Spinnler, A. D. Wieck, A. Ludwig, and R. J. Warburton, arXiv:2003.00023 (2020).

[282] D. Najer, I. Söllner, M. C. Loebl, D. Riedel, B. Petrak, S. Starosielec, V. Dolique, S. R. Valentin, R. Schott, A. D. Wieck, A. Ludwig, and R. J. Warburton, in *2018 IEEE Photonics Society Summer Topical Meeting Series (SUM)* (IEEE, 2018) pp. 169–170.

[283] D. Riedel, S. Flågan, P. Maletinsky, and R. J. Warburton, Phys. Rev. Applied **13**, 014036 (2020).

[284] T. Hümmer, J. Noe, M. S. Hofmann, T. W. Hänsch, A. Högele, and D. Hunger, Nat. Commun. **7**, 12155 (2016).

[285] J. H. Davies, *The physics of low-dimensional semiconductors: an introduction* (Cambridge university press, 1998).

[286] P. Harrison and A. Valavanis, *Quantum wells, wires and dots: theoretical and computational physics of semiconductor nanostructures* (John Wiley & Sons, 2016).

[287] S. Ferrari, C. Schuck, and W. Pernice, Nanophotonics **7**, 1725 (2018).

[288] A. D. Semenov, G. N. Gol'tsman, and A. A. Korneev, Physica C: Superconductivity **351**, 349 (2001).

[289] G. N. Gol'tsman, O. Okunev, G. Chulkova, A. Lipatov, A. Semenov, K. Smirnov, B. Voronov, A. Dzardanov, C. Williams, and R. Sobolewski, Appl. Phys. Lett. **79**, 705 (2001).

[290] A. J. Annunziata, O. Quaranta, D. F. Santavicca, A. Casaburi, L. Frunzio, M. Ejrnaes, M. J. Rooks, R. Cristiano, S. Pagano, A. Frydman, and D. E. Prober, J. Appl. Phys. **108**, 084507 (2010).

[291] G. Reithmaier, M. Kaniber, F. Flassig, S. Lichtmannecker, K. Müller, A. Andrejew, J. V. R. Gross, and J. J. Finley, Nano Lett. **15**, 5208 (2015).

[292] R. Gourgues, J. W. Los, J. Zichi, J. Chang, N. Kalhor, G. Bulgarini, S. N. Dorenbos, V. Zwiller, and I. E. Zadeh, Optics express **27**, 24601 (2019).

List of Publications

1. Liang Zhai, Matthias C. Löbl, Giang N. Nguyen, Julian Ritzmann, Alisa Javadi, Clemens Spinnler, Andreas D. Wieck, Arne Ludwig, Richard J. Warburton, *Low-Noise GaAs Quantum Dots for Quantum Photonics*, arXiv:2003.00023 (2020).
2. Ravitej Uppu, Hans T. Eriksen, Henri Thyrrestrup, Aslı D. Uğurlu, Ying Wang, Sven Scholz, Andreas D. Wieck, Arne Ludwig, Matthias C. Löbl, Richard J. Warburton, Peter Lodahl, and Leonardo Midolo, *On-chip deterministic operation of quantum dots in dual-mode waveguides for a plug-and-play single-photon source*, arXiv:2001.10716 (2020).
3. Matthias C. Löbl, Clemens Spinnler, Alisa Javadi, Liang Zhai, Giang N. Nguyen, Julian Ritzmann, Leonardo Midolo, Peter Lodahl, Andreas D. Wieck, Arne Ludwig, and Richard J. Warburton, *Radiative Auger Process in the Single Photon Limit on a Quantum Dot*, arXiv:1911.11784 (2019).
4. Liang Zhai, Matthias C. Löbl, Jan-Philipp Jahn, Yongheng Huo, Oliver G. Schmidt, Armando Rastelli, and Richard J. Warburton *Large-Range Frequency Tuning of a Narrow-Linewidth Quantum Emitter*, manuscript in preparation.
5. Daniel Najer, Immo Söllner, Pavel Sekatski, Vincent Dolique, Matthias C. Löbl, Daniel Riedel, Rüdiger Schott, Sebastian Starosielec, Sascha R. Valentin, Andreas D. Wieck, Nicolas Sangouard, Arne Ludwig, Richard J. Warburton, *A gated quantum dot strongly coupled to an optical microcavity*, Nature **575**, 622–627 (2019).
6. Matthias C. Löbl, Liang Zhai, Jan-Philipp Jahn, Julian Ritzmann, Yongheng Huo, Andreas D. Wieck, Oliver G. Schmidt, Arne Ludwig, Armando Rastelli, Richard J. Warburton, *Correlations between optical properties and Voronoi-cell area of quantum dots*, Physical Review B **100**, 155402 (2019).
7. Matthias C. Löbl, Sven Scholz, Immo Söllner, Julian Ritzmann, Thibaud Denneulin, Andras Kovacs, Beata E. Kardynał, Andreas D. Wieck, Arne Ludwig, Richard J. Warburton, *Excitons in InGaAs quantum dots without electron wetting layer states*, Communications Physics **2**, 93 (2019).

8. Dapeng Ding, Martin Hayhurst Appel, Alisa Javadi, Xiaoyan Zhou, Matthias C. Löbl, Immo Söllner, Rüdiger Schott, Camille Papon, Tommaso Pregnolato, Leonardo Midolo, Andreas D. Wieck, Arne Ludwig, Richard J. Warburton, Tim Schröder, and Peter Lodahl, *Coherent optical control of a quantum-dot spin-qubit in a waveguide-based spin-photon interface*, Physical Review Applied **11**, 031002 (2019).

9. Daniel Najer, Immo Söllner, Matthias C. Löbl, Daniel Riedel, Benjamin Petrak, Sebastian Starosielec, Vincent Dolique, Sascha R. Valentin, Ruediger Schott, Andreas D. Wieck, Arne Ludwig, Richard J. Warburton, *A Charge-Tunable Quantum Dot Deep in The Strong Coupling Regime of Cavity QED*, 2018 IEEE Photonics Society Summer Topical Meeting Series (SUM), 169–170 (2018).

10. Alisa Javadi, Dapeng Ding, Martin Hayhurst Appel, Sahand Mahmoodian, Matthias C. Löbl, Immo Söllner, Rüdiger Schott, Camille Papon, Tommaso Pregnolato, Søren Stobbe, Leonardo Midolo, Tim Schröder, Andreas D. Wieck, Arne Ludwig, Richard J. Warburton, and Peter Lodahl, *Spin–photon interface and spin-controlled photon switching in a nanobeam waveguide*, Nature Nanotechnology **13**, 398–403 (2018).

11. Henri Thyrrestrup, Gabija Kirsšanskė, Hanna Le Jeannic, Tommaso Pregnolato, Liang Zhai, Laust Raahauge, Leonardo Midolo, Nir Rotenberg, Alisa Javadi, Rüdiger Schott, Andreas D. Wieck, Arne Ludwig, Matthias C. Löbl, Immo Söllner, Richard J. Warburton, and Peter Lodahl, *Quantum optics with near-lifetime-limited quantum-dot transitions in a nanophotonic waveguide*, Nano Letters **18**, 1801-1806 (2018).

12. Matthias C. Löbl, Immo Söllner, Alisa Javadi, Tommaso Pregnolato, Rüdiger Schott, Leonardo Midolo, Andreas V. Kuhlmann, Søren Stobbe, Andreas D. Wieck, Peter Lodahl, Arne Ludwig, and Richard J. Warburton, *Narrow optical linewidths and spin pumping on charge-tunable close-to-surface self-assembled quantum dots in an ultrathin diode*, Physical Review B **96**, 165440 (2017).

13. Gabija Kiršanskė, Henri Thyrrestrup, Raphaël S. Daveau, Chris L. Dreeßen, Tommaso Pregnolato, Leonardo Midolo, Petru Tighineanu, Alisa Javadi, Søren Stobbe, Rüdiger Schott, Arne Ludwig, Andreas D. Wieck, Suk In Park, Jin D. Song, Andreas V. Kuhlmann, Immo Söllner, Matthias C. Löbl, Richard J. Warburton, and Peter Lodahl, *Indistinguishable and efficient single photons from a quantum dot in a planar nanobeam waveguide*, Physical Review B **96**, 165306 (2017).

Curriculum Vitae: Matthias C. Löbl

Personal Information

Work address: Klingelbergstrasse 82, 4056 Basel, Switzerland
Current e-mail address: matthias.loebl@unibas.ch
Permanent e-mail address: matthias.loebl@rwth-aachen.de
Date of birth: 24 September 1991
Citizenship: Germany

Education

November 2015 - January 2020: PhD in Experimental Physics
University of Basel, Switzerland
Thesis: *Excitons in Quantum Dots and Design of their Environment*
Supervisor: Prof. Richard J. Warburton
Grade: summa cum laude

October 2013 - September 2015: Master in Physics
RWTH Aachen University, Germany
Thesis: *Towards an Optical Interface to Electrically-Controlled Spin-Qubits in GaAs-Based Heterostructures*
Supervisors: Prof. Beata Kardynał, Prof. Hendrik Bluhm

October 2010 - September 2013: Bachelor in Physics
RWTH Aachen University, Germany